Estimation of Breast Density from DICOM Header Data using a Geant4 Monte-Carlo Simulation of the Mammography Imaging Process.

A thesis
submitted in partial fulfilment
of the requirements for the Degree
of
Master of Science in Medical Physics
by

Brett Cunningham

Department of Physics and Astronomy
University of Canterbury
March 6, 2017

Abstract

Breast density is the fractional measurement of glandular tissue versus that of adipose and connective tissue in the breast. This value is often determined from the subjective interpretation of a mammography image by a radiologist. Because this may vary significantly between interpretations, a more formal measure is required to describe a breast density in terms of it's radiographic characteristics, and can be clearly understood and communicated.

Geant4 Monte-Carlo package was used to develop a simulation of the mammography imaging process that included relevant geometries specific to a GE Senograph Essential mammography unit. Filter transmission data was collected for filter materials molybdenum, rhodium and aluminium with anode materials molybdenum, rhodium and tungsten over energy ranges 24-36kV with 2kV increments. Subsequent breast transmission data was collected for selected beam parameters using polymethyl methacrylate(PMMA) and water as breast materials.

From this transmission data a water equivalent thickness was able to be calculated with the aid of Dance, Skinner, Young, Beckett, and Kotre (2000) equivalent breast thickness calculations, as well as an associated breast density, or glandularity. It was found that the mean simulated breast transmission uncertainty was $\pm 4.8\%$, and mean GE Senograph Essential breast transmission uncertainty was $\pm 5.2\%$. This meant the majority of transmission curves fell within each others error bars as the mean transmission difference was 8.6%. Ultimately a water equivalent thickness was calculated to within a mean accuracy of $\pm 7.0\%$.

Acknowledgments

First and foremost I need to need to convey my sincerest gratitude to my supervisors, Dr. Steven Marsh and Mr. Brian Lunt. There guidance, support and encouragement from afar was gratefully accepted, and needed.

The idea of a project with Mr. Lunt was first posed back in mid 2015 when I first expressed an interest in imaging, and the prospect of an imaging thesis project, with Dr. Marsh. His name was put forward in subsequent conversations, and was encouraged to contact him in December 2015. What eventuated was what I consider a leap of faith for Mr. Lunt to take on a Masters student, and I will be forever grateful for that.

I would also like to thank Dr. Orlon Petterson for his support with the University's physplack compute cluster, the use of that facility transformed the project's time constraints and data acquisition.

Lastly, I need to thank my family. Over the years my wife and children have been immensely supportive and encouraging in my venture towards this degree, and I wouldn't have been able to it without them.

Table of Contents

List of Figures

List of Tables

Glossary and Acronyms

ACPSEM Australasian College of Physical Scientists and Engineers in Medicine
ACR American College of Radiology

Be Beryllium: Z = 4
BI-RADS Breast Imaging Reporting and Data System: 5th edition

CC Cranial-caudal
CLHEP Class Library High Energy Physics
CPE Charged Particle Equilibrium
CsI(Tl) Thallium activated Caesium iodide

DICOM Digital Imaging and Communications in Medicine
DR Digital Radiography

ESAK Entrance Skin Air Kerma

FOV Field of View

Geant4 Geometry And Tracking version 4

HVL Half Value Layer - the thickness of an Aluminium filter generating an air kerma transmission (and thus also absorption) factor of 50 percent

IAEA International Atomic Energy Agency
IAK Incident Air Kerma
IVS Inverse Square

Kerma Kinetic Energy Released in the Medium per unit mass, "a" is added for phonetic convenience.
keV kilo-electron volt
kVp kilovolt peak - The peak electric potential applied across the x-ray tube

mAs	milliampere second - The tube current across
MGD	Mean Glandular Dose
mGy	milli-Gray; unita of kerma and dose - mJ/kg
MLO	Medial-lateral-oblique
Mo	Molybdenum: Z = 42
MTF	Modulation Transfer Function
NIST	National Institute of Standards and Technology
PMMA	Polymethyl methacrylate
Rh	Rhodium: Z = 45
RMSE	Root Mean Squared Error
SID	Source to Image Distance
SNR	Signal to Noise Ratio
W	Tungsten: Z = 74

Chapter I

Introduction

The most common invasive malignancy among women in New Zealand is breast cancer, accounting for more than 3000 new registrations and 600 deaths per year since 2012 (Ministry of Health, 2016b; Soeberg, 2014). Although breast cancer can very rarely occur in males, approx. 0.7% of the total new registrations yearly (Ministry of Health, 2016a), women above the age of menopause make up the largest majority; it is seldom seen in women below the age of 30 unless genetically predisposed (Tortora & Derrickson, 2012). In order to combat an increasing trend of new breast cancer registrations each year, women over the age of 45 years are encouraged to undergo mammography screening.

Mammography is radiography of the breast which uses x-ray imaging to diagnose symptomatic patients and for screening of, predominantly, asymptomatic women. It is an essential part of early breast cancer diagnosis, meaning earlier treatment intervention may lead to lower mortality rates. To produce an image of good diagnostic quality which clearly show abnormalities, the mammogram must have unique radiographic characteristics.

Because mammography is a specialised radiographic technique, it uses x-rays to produce what is essentially a density map of the breast tissue. But unlike plain radiography where the difference in densities being imaged are quite large, i.e. between bone and surrounding soft tissue, mammography must use low energy, nearly mono-energetic x-rays for the subtle attenuation differences between various tissues found in the breast, i.e. adipose tissue, normal glandular breast tissue and cancerous tissue, to have a subjective contrast on a mammographic image. Breast tissue is, however, sensitive to ionising radiation particularly at higher relative doses, which may induce breast cancer (Dance et al., 2014). This poses a difficult problem as one must produce the best diagnostic quality image while using a dose that is as

low as reasonably achievable.

There are many variables associated with breast dose, and in the digital mammography realm signal to noise ratio (SNR) is a major factor as the level of beam attenuation by the breast directly affects beam transmission and, subsequently, image quality (Bushberg & Boone, 2011). The descriptors for the cause of the attenuation and x-ray absorption are, generally, breast thickness (cm), and breast composition which is usually defined as glandular vs adipose tissue density percentage (N. F. Boyd et al., 2010; Bushberg & Boone, 2011). However, to understand more accurately the relationship between the breast's attenuation characteristics and image quality, those characteristics need to be represented quantitatively, and such a quantity must reflect the mass of the tissue the beam passes through.

Describing this quantity may be difficult to articulate in the context of attenuation characteristics as both breast composition and thickness varies considerably across the population. Thus in order to represent this quantity to be used and standardised in normal conversational English, and can be easily understood, a water equivalent thickness best serves this purpose.

1.1 Project Framework and Objectives

In order to achieve the required goal, that being to describe the radiographic characteristics of a breast in terms of a water equivalent thickness, a Monte Carlo simulation of the imaging process is going to be developed which will then be validated against real world measurements. There are many different Monte Carlo packages available from which a mammography unit simulation can be developed, but in this case the GEometry ANd Tracking (Geant4) tool-kit will best serve the mammography application for reasons explained in Chapter 2.

The following objectives outline the scope of the project:

1. Become familiar with the Geant4 Monte-Carlo simulation package, and accurately simulate polychromatic x-ray production of a mammography beam.

This particular objective is fundamentally important to subsequent objec-

tives and the project overall. Understanding and implementing Geant4 accurately, i.e. correctly model relevant geometry, apply and simulate appropriate physical processes, and produce an acceptable set of data for analysis, requires a reasonably steep learning curve.

2. Use the Geant4 package to simulate a filtered mammography beam, thus obtaining an equation, or set of equations to accurately predict filter thickness.

This objective assumes prior knowledge of the beams output: kVp, waveform, mAs, target material, target angle, filter material and mGy output; data which can be taken from an accurate mammography tube simulation. With this knowledge one can fit an equation to the filter transmission data for a specific set of beam parameters.

3. Following on from objective 2, use Geant4 package to simulate broad beam transmission of a mammography beam through different stages of the imaging process, ultimately acquiring an equation or set of equations which accurately predicts breast density in terms of a water equivalent thickness.

The prediction is based on readily available Digital Imaging and Communications in Medicine (DICOM) tag data as well as transmission data from the simulation. Correctly simulating the breast and other associated geometries, i.e. compression paddle, breast support, skin thickness and the grid, will be critically important to minimise any correction factors and abnormal errors that may arise. A range of breast thicknesses will be simulated as well as integrating the filter thickness calculation from objective 2.

4. Amalgamating the above objectives to develop a test protocol for field validation using a standard QA phantom to produce calibration factors for an individual machine, in this case a General Electric (GE) Senographe Essential.

Although validation will occur throughout to ensure simulation accuracy, a field test protocol is important which may introduce some correction factors.

1.2 Summary of Method

In order to achieve the above objectives, a method was employed somewhat similar to Dance et al. (2000). However as a polymethyl methacrylate (PMMA) breast was used in Dance et al. (2000), a water breast will be used here as well as altering a number of mammography machine specific geometries.

The summary of the method used is as follows:

1. Install required software to run the Geant4 tool-kit using a Linux operating system.

2. Use pre-installed Geant4 resources to develop a programme for a mammography x-ray tube. Compare x-ray tube spectral data with that of other published spectral data, validating the simulation as an accurate representation of a mammography spectrum.

3. Insert filter(s) into programme and obtain filter transmission data. Compare with other published data and model filter transmission to ascertain filter thickness for a range of known input parameters.

4. Write into programme remaining geometries: compression paddle, patient support, grid and digital radiography (DR) detector. These will be machine specific (GE Senographe Essential), and will need to be as accurate as possible.

5. Obtain transmission data for a range of breast thicknesses. Calculate a ratio between the incident air kerma on the upper side of the breast under the compression paddle, and the dose measured under the breast below the breast support and grid. Model the ratio fitting an equation for a set of specific input parameters based on readily available DICOM tag data. This will also incorporate the filter thickness calculation.

Although validation procedures haven't been explicitly detailed, throughout the course of the project reasonably extensive testing and secondary experimentation occurred. Chapter 3 and Chapter 4 will explain the scope of these experiments and their results.

Chapter II

Background

2.1 Breast Anatomy

The breast is an organ located on the anterior chest wall and extends cranially from the second or third rib to the sixth or seventh rib caudally. Laterally it stretches from the lateral edge of the sternum to the mid-axillary line, or armpit (De Benedetto et al., 2016; Ellis & Mahadevan, 2013). The breast or mammary gland consists of two major groups of tissue, the glandular tissue which is the milk producing component, and the connective tissue which makes up the remainder of the breast mass and aids in the support of the breast. Adipose tissue, fascia and muscle are all part of the breast's connective tissue.

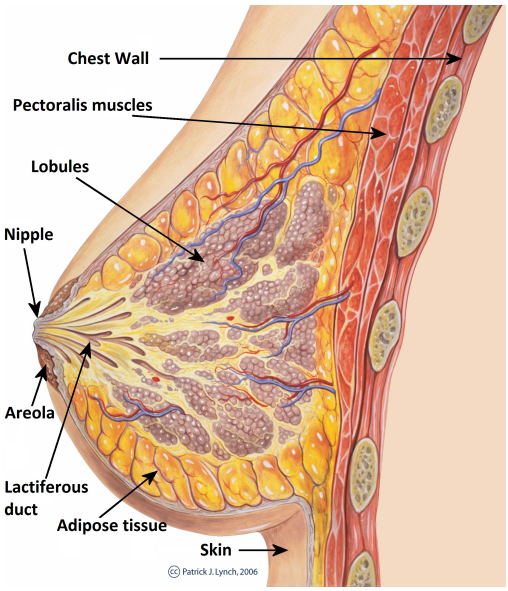

Figure 2.1: A medial lateral breast depiction showing major anatomical breast features.

The glandular tissue of the breast is a modified apocrine sweat gland containing 15-20 lobes, of which each has 10-100 lobules where multiple acini in each lobule produce and store milk during lactation (Hogg, Kelly, & Mercer, 2015). The quantity of lobes, lobules and acini have a number of influencing factors including age, hormone production and lacation; it's the quantity of this glandular tissue relative to the connective tissue (predominantly adipose tissue) that give the breast a density classification.

2.2 Breast Density Classification

There are a number of breast density classifications, to name three: Boyd (N. Boyd et al., 1982), which divides the mammographic density into six percentage based categories; Tabar (Gram, Funkhouser, & Tabár, 1997), which uses five unique density pattern descriptions; and the Breast Imaging Reporting and Data System (BI-RADS) classification system which visually categorises the quantity of glandular tissue seen within a mammography image (Sickles et al., 2013). The four categories of the BI-RADS breast desity classification are:

Table 2.1: BI-RADS breast density classification, taken from Sickles et al. (2013) .

Classification	**Description**
ACR1	The breasts are almost entirely fatty.
ACR2	There are scattered areas of fibroglandular density.
ACR3	The breasts are heterogeneously dense, which may obscure small masses.
ACR4	The breasts are extremely dense, which reduces the sensitivity of mammography.

Although this is not a percentage based system, which can serve as an indicator of cancer risk, the BI-RADS system is widely used and accepted to give a subjective definition of the quantity and distribution of glandular tissue. The system also incorporates the relative sensitivity of mammography for a given image, ACR1 indicates a mostly fatty breast thus mammography is very sensitive. However, locating lesions and masses with an ACR4

breast becomes much more difficult as overlying glandular tissue can obscure abnormalities; here mammography sensitivity can be very low.

The relative quantity of glandular tissue will decrease with the start of menopause due to the body rapidly decreasing the production of oestrogen and progesterone, leading to an increase of breast adipose tissue. This gives the mammography exam a much higher sensitivity, enabling the detection of neoplasms to be much more obvious (Ellis & Mahadevan, 2013). This is the central reasoning behind breast screening of post-menopausal women.

2.3 Mammography

To be able to view the anatomy of the breast and detect associated pathology, the radiography procedure must be specifically sensitive to the unique attributes of breast anatomy, all while delivering a dose that is as low as reasonable achievable. This is of particular importance as mammography is used for screening of asymptomatic patients, thus the lower the delivered dose to the breast, a particularly radio-sensitive anatomical area, the lower any future stochastic cancer risks.

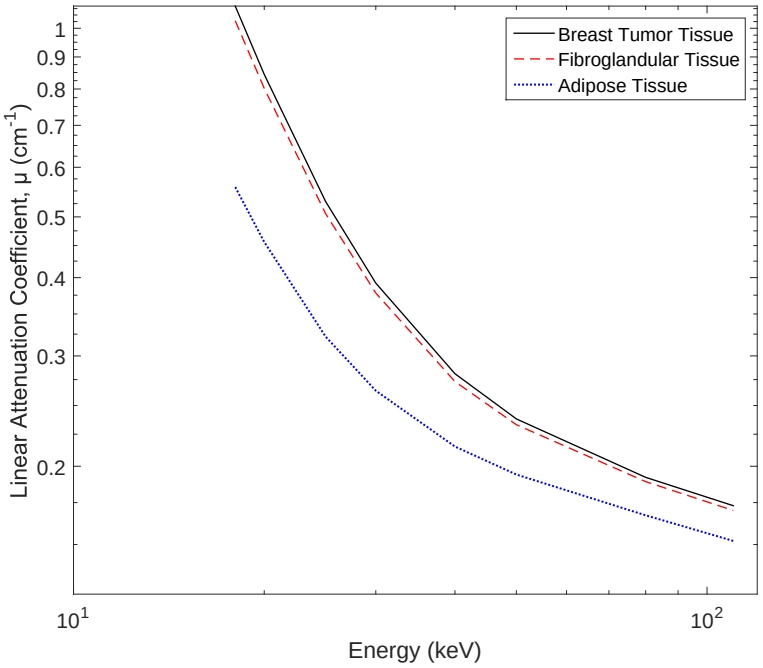

Figure 2.2: The linear attenuation of adipose, fibroglandular and breast tumor tissue. Graph reproduced using data from (P. C. Johns & Yaffe, 1987).

Radiologically, the contrast differences between normal glandular tissue and cancerous tissue or calcifications, are tiny due to the attenuation coefficients being very similar; Figure 2.2 and 2.3 highlight attenuation differential and relative subject contrast. It can be seen that the optimal attenuation differential clearly occurs at very low energies where attenuation of adipose tissue is minimal while maximising the difference in cancerous and glandular tissue, thus accentuating subject contrast. At higher energies subject contrast is seen to decreases sharply over a reasonably short energy range.

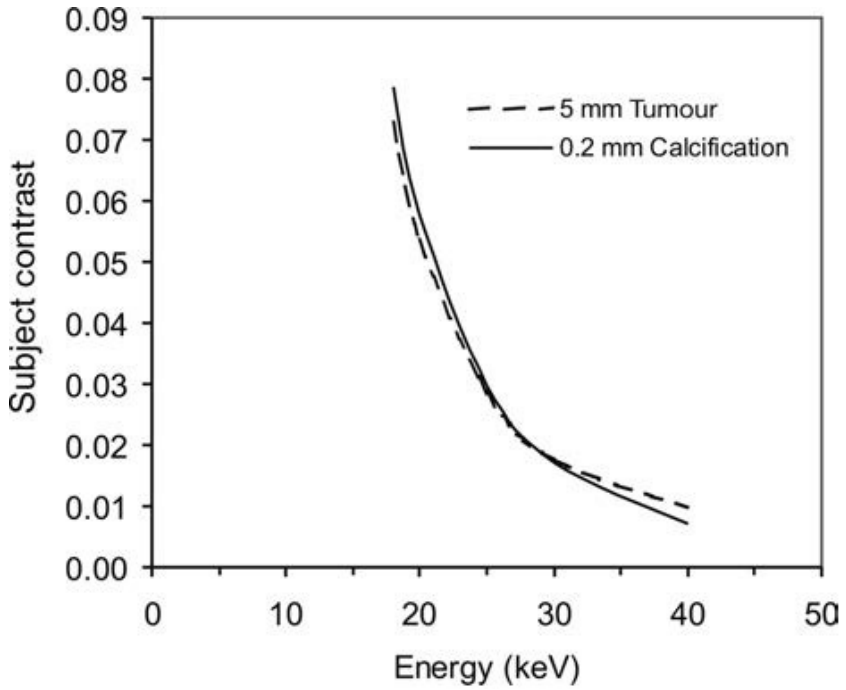

Figure 2.3: Subject contrast of a 5mm tumor and 0.2mm calcification as a function of energy, relative to breast glandular tissue (Bushberg & Boone, 2011; Dance et al., 2014).

Additionally the size of the pathology being imaged can range from less than 1mm when looking at calcifications, but can be as small as 20μm, to larger low contrast and poorly defined masses. Mammography, therefore requires a very high spatial resolution detector which is generally achieved using high doses (Hogg et al., 2015). To overcome the challenges of producing a mammography image of high subject contrast and high spatial resolution while delivering as low a dose as possible, mammography units house a range of specialized equipment.

2.3.1 Mammography Equipment

Unlike plain radiography, the mammography x-ray tube is located above the image detector such that the line from the focal spot to the edge of the detector closest the patient forms a vertical line. This important collimation design feature allows the beam to skim the chest wall, if the focal spot was located as in a plain radiography design the beam would miss some breast tissue, and as a result some tissue wouldn't be imaged.

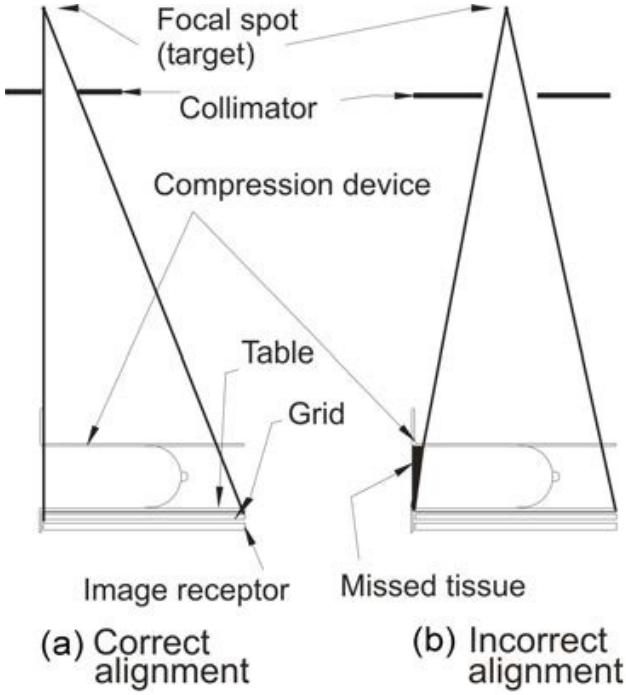

Figure 2.4: Correct and incorrect alignment of mammography beam geometry (Bushberg & Boone, 2011; Dance et al., 2014).

The x-ray tube specific to a mammography machine is fitted with features not too dissimilar to plain radiography, but functions with different operating parameters and materials. Firstly the cathode filament of an x-ray tube, be it plain radiography or mammography, are most commonly a wound tungsten coil. However, some mammography units offer dual focal spot sizes, 0.3mm and 0.1mm, for the purpose of magnification and general mammography which arises from two separate length filaments; a shorter and longer filament respectively (Bushberg & Boone, 2011). The tube will operate, generally, below 40kV with a filament current limited to 100mA and 25mA for the 0.3

and 0.1mm focal spot respectively. The filament current is limited to directly limit the tube current due to Molybdenum (Mo) and Rhodium (Rh), as an anode material, having lower melting points when compared to Tungsten (W). In the case of a W anode, filament currents can be as high as 200mA and 50mA for the respective focal spots (Bushberg & Boone, 2011; Dance et al., 2014).

The anode of the mammography x-ray tube can range in material, the most common being Molybdenum but Rhodium and Tungsten are also used depending on the imaging acquisition method, e.g. film or digital, and the breast characteristics such as compressed thickness and density. The varying materials used in mammography are driven by the inherent low accelerating potentials used in the x-ray tube, and the material's atomic properties. The central motivation for the use of Mo and Rh as anode materials are their characteristic x-ray production coming from their K-shell electron binding energies. Characteristic emission greatly increase the quantity of x-rays in an energy range optimal to the mammography imaging technique. In the case of W, which has a much higher Z, this will produce non-characteristic x-rays more efficiently than Mo and Rh (this will be discussed in the next section). When used with a digital detector, characteristic x-ray production becomes less important as image processing can be used to enhance contrast post acquisition (Bushberg & Boone, 2011).

X-ray production is notoriously inefficient in terms of energy conversion, a large proportion of electron kinetic energy is transferred to heat leading to the significant increase in anode temperature. To combat this most modern anodes have a rotating design to spread the heat loading, this can enable the tube to withstand higher tube currents and exposure time, Figure 2.5 depicts two different rotating anode designs currently used. Figure 2.5 also describes the anode angle, which can differ depending on the anode design. The GE Essential uses a 0 degree anode angle design.

Tube angle, or tube tilt, plays a fairly significant role in the maximum field of view (FOV) of a mammography unit. At typical source-to-image distances (SID) the minimum effective tube angle to achieve a large FOV, 24 x 30cm at an SID of 60cm, is at least 22 degrees. This minimum tube angle arises from the complete attenuation of x-rays on the lower edge of the

anode. However, in the case of a GE Essential the FOV is 24 x 30.7cm at an SID of 66cm, thus the minimum required combined tube angle is 20 degrees; the tube angle of a GE Essential is in fact 22.5 degrees.

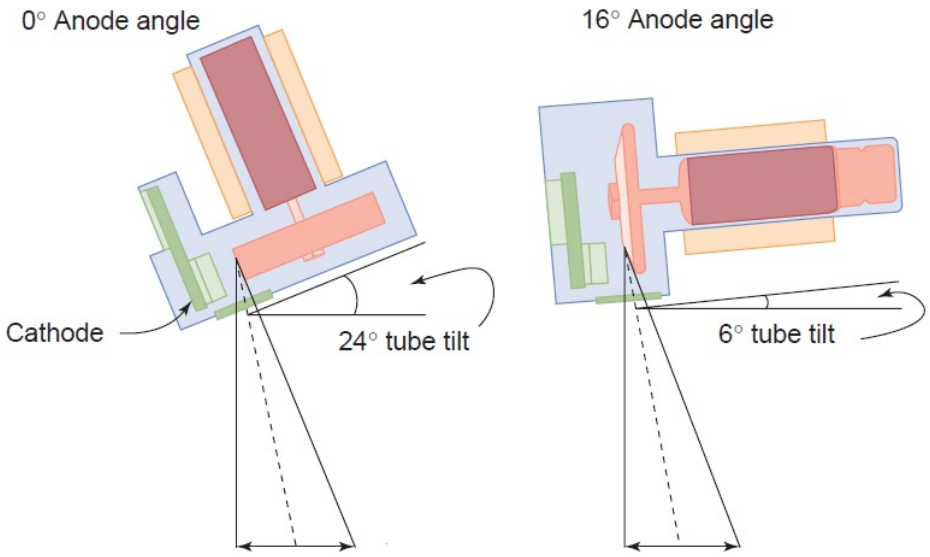

Figure 2.5: Tube angles, or tube tilt, designs of typical mammography tubes with differing anode angles (Bushberg & Boone, 2011).

It is also important to note that the tube angle directly affects the amount of x-ray absorption in the anode material. Increasing the tube angle decreases the x-ray absorption length in the target, this results in an unchanged kVp but a decrease in hardness or half value layer (HVL) and increased yield; the opposite is true with a decreasing tube angle.

Filters used in mammography differ significantly from that used in plain radiography. Instead of glass the exit window is made from Beryllium (Be), which has a low atomic number ($Z = 4$) enabling it to filter x-rays below about 5keV; the thickness of these windows can be up to 1mm, a GE Essential employs a 0.69mm Be window. Additionally, due to the characteristics of a mammography spectrum produced from Mo, Rh or W which are a sum of bremsstrahlung and characteristic x-rays (explained further in section 2.3.2), some x-rays are detrimental to image quality and patient dose, and therefore need to be eliminated.

In eliminating unwanted x-rays, both low and high energy, it improves

the spectrum's energy distribution. This is achieved with thin filter materials such as Mo, Rh, Al, and Silver (Ag) which are able to absorb specific bands of energies to enhance the spectrum's characteristics. Filter material and thickness vary depending on the anode material and the imaging purpose, Mo and Rh anodes may use either Mo or Rh filters up to about 0.035mm thick, where as W anode can use Mo, Rh, Al and Ag filter materials ranging up to 0.05mm for Mo, Rh and Ag, and up to 0.7mm for Al. Examples of unfiltered and filtered spectra (produced from this project) can be found in Appendix **??**.

In filtering the mammography beam, one of its key characteristics that changes is the HVL. The HVL of a mammography beam is again dependent on anode material, filter material, kV and filter thickness, but is generally below 0.7mmAl. Examples of HVL's for this project can be found in Appendix C. From those tables it can be seen that a Mo anode at 26kV with a Mo filter 0.03mm thick produces a HVL of 0.328mmAl, where as a W anode at 34kV with an Al filter 0.55mm thick has produced a HVL of 0.531mmAl. It must be noted that the compression paddle of the machine also provides some beam attenuation and therefore contributes to the HVL.

HVL plays a major role in dose deposited to the breast and image quality. If the beam has too much filtering it becomes to penetrative and reduces image quality, whereas if there is not enough filtering the beam has too many low energy photons which have low penetration and can increase the breast dose resulting in poor image quality. A specific optimal "recipe" of parameters is therefore required for each individual breast, dependant on breast density and compressed thickness. Specific protocols are often tested on mammography units to ensure they perform to within required guidelines. Some of those include testing HVL and the average breast dose, or mean glandular dose, and examining their correlation if they fall outside of regulated parameters.

Down stream of the compression paddle lies the breast itself which, during examination, is compressed in the cranial-caudal (CC) or medial-lateral-oblique (MLO) orientation between the compression paddle constructed from perspex, and a carbon fibre breast support. As the beam travels through these structures it will create a significant quantity of scattered x-rays, some

of which may make it to the detector. These are generally lower energy x-rays that don't necessarily contribute to image quality, but add random noise to the image degrading subject contrast. To combat this an anti-scatter grid is positioned between the breast support and the detector which eliminates any randomly varying radiation distributions.

Anti-scatter grids are are typically made from lead but can be made from other materials such as copper, depending on their design: 1D linear, 2D linear or 2D cellular, all of which can be focussed or unfocussed.

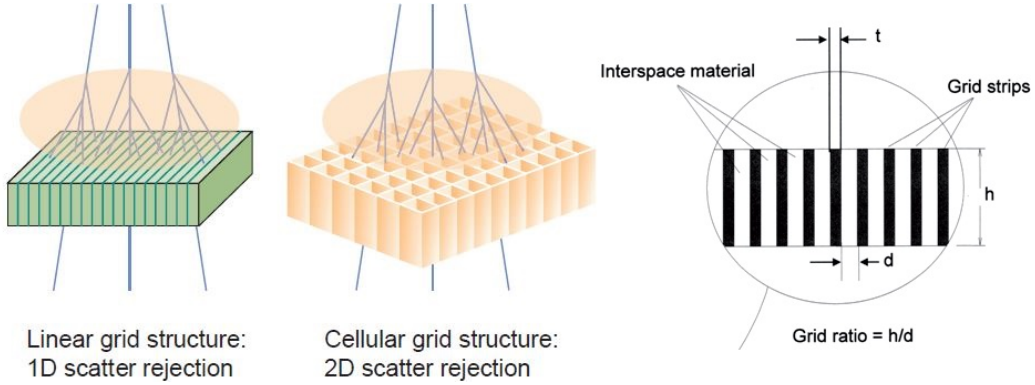

Figure 2.6: Depiction of grid construction and function. Focused grid structure is not shown, however the septa (grid strips) are angled for the specific mammography machine characteristics such as FOV and SID (Bushberg & Boone, 2011; Dance et al., 2014).

Focussed cellular type grids are widely used in mammography, the grid ratio (as described in Figure 2.6) of 5:1 is generally employed, an example might be a 1.4mm height, 0.28mm between septa with a 0.015mm septa thickness. The grid frequency of mammography grids range between $30-45cm^{-1}$, this can be calculated using the relation $1/(t+d)$ so in the above example this would lead to a grid frequency of $34cm^{-1}$. These physical characteristics of the grid effect the efficiency of scatter elimination, which can be up to 85%, and the beam transmission ranging from $65-75\%$ (Bushberg & Boone, 2011; Dance et al., 2014).

It must be noted that most modern mammography machines render their image through DR, however as the process of image acquisition through DR isn't overly pertinent to the project, it won't be covered here.

2.3.2 X-ray Production

In 1895 German physicist Wilhelm Roentgen discovered that when a beam of electrons contacts a target material x-rays are produced. This x-ray production was primarily a function of two physical interactions electrons have with matter, where the electrons lose some of their energy through bremsstrahlung or braking radiation, and characteristic radiation. Bremsstrahlung radiation is produced when the electron tracks close to the nucleus of the atom, the electron then partially orbits the nucleus from the strong Coulombic forces between the negative electron and positive nucleus. The result is the emission of an x-ray with energy equal to the difference in initial and final energy of the electron; i.e. taking E equal to the electron incident energy, then $h\nu = E - E'$ where E' is the final electron energy and $h\nu$ equal to the x-ray's energy; h is Planck's constant, and ν is the frequency. When the electron is completely stopped $E' = 0$, then $h\nu = E$ and the produced x-ray is equal to the energy of the incident electron, this is an important concept from a radiography or mammography perspective as it says the peak x-ray energy can only be as high as the peak electron energy, which is governed by the accelerating potential across the x-ray tube (H. E. Johns & Cunningham, 1983).

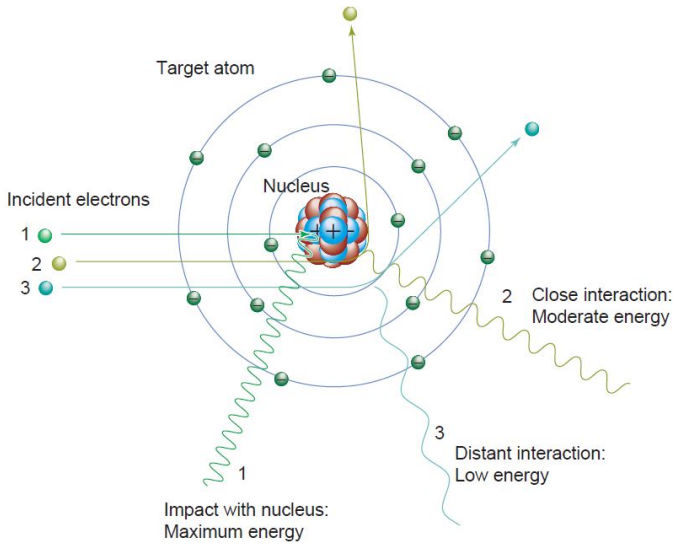

Figure 2.7: Bremsstrahlung radiation production (Bushberg & Boone, 2011).

Bremsstrahlung radiation makes up a significant proportion of an x-ray spectrum, and the probability of a bremsstrahlung interaction is heavily in-

fluenced by the Z of the target material and the mass of the incident particle. The total bremsstrahlung radiation produced per atom is proportional to Z^2/m^2, the efficiency therefore increases for higher Z materials, but decreases for high mass incident particles (H. E. Johns & Cunningham, 1983). Although the overall efficiency of x-ray production is very low, an electron will produce almost a million times more bremsstrahlung than that of a proton of alpha particle. As bremsstrahlung is considered a collisional energy loss and heat production considered radiative energy loss, the ratio of the two for an electron beam can be described as:

$$\frac{\text{Radiative energy loss}}{\text{Collisional energy loss}} = \frac{E_k Z}{8.2 \times 10^5} \tag{2.1}$$

where E_k is the kinetic energy of the incident photon in keV (Bushberg & Boone, 2011). However, more generally the efficiency of x-ray production, that being the ratio of x-ray energy output to incident electron input energy can be approximated as:

$$\text{Efficiency} = 9 \times 10^{-10}\ ZV \tag{2.2}$$

where V is the tube voltage in volts (Khan & Gibbons, 2014). In terms of mammography energies this figure is very low. Take, for example, a 30kV x-ray tube with a Mo target, the efficiency can be calculated as:

$$\text{Efficiency} = 9 \times 10^{-}10\ (42)(3 \times 10^5) = 0.1\%$$

Only at much higher energies does x-ray efficiency increase markedly which can be achieved with a linear accelerator to the order of $30 - 95\%$ depending on the energy of the electron beam.

This concept of x-ray production is an important consideration in terms of the project's initial framework as the efficiency can have and impact on subsequent data quality; this will be discussed in Chapter 5.

The second interaction making up an x-ray spectrum is the radiation produced by the photoelectric effect and inelastic scattering. These x-ray energies are specific to the target material and are a characteristic of the element's shell binding energies; hence the term characteristic radiation. The mechanism in which this occurs from an incident electron with a kinetic energy starts with an interaction between said electron and an orbital electron.

If the incident electron energy, dependant on the x-ray tubes accelerating potential, is greater than that of the orbital electron, then there is a probability the interaction may eject the bound electron ionizing the atom. With an orbital vacancy the atom will tend towards a stable state, immediately transitioning an outer orbital electron with a lower bound energy state to fill the vacancy. From a quantum mechanics perspective, the transitioning electron loses energy in the form of a photon equal to the difference between the orbital energy states; Figure 2.8 depicts this process.

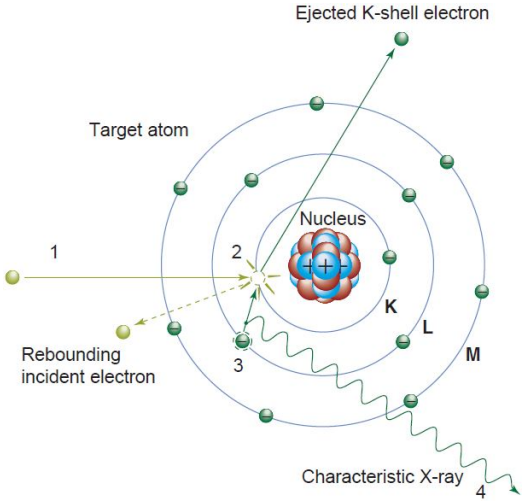

Figure 2.8: Characteristic radiation production (Bushberg & Boone, 2011).

As an example take the K, L and M-shell binding energies of Mo and calculate their resulting x-rays: K-shell = 20.0keV, L-shell = 2.8, 2.6, and 2.5keV, M-shell = $0.5 - 0.4$keV.

$$E_{KLI} = E_{LI} - E_K = -2.8 - (-20.0) = 17.2keV$$
$$E_{KLII} = E_{LII} - E_K = -2.6 - (-20.0) = 17.4keV$$
$$E_{KLIII} = E_{LIII} - E_K = -2.5 - (-20.0) = 17.5keV$$
$$E_{MLI} = E_{MI} - E_K = -0.5 - (-20.0) = 19.5keV$$
$$E_{KLII} = E_{MII} - E_K = -0.4 - (-20.0) = 19.6keV$$

These values are not precise, but are representative of the characteristic x-rays produced from an Mo target. It can be seen, therefore, that unlike bremsstrahlung x-ray energies characteristic radiation has discrete energy values. Generally, those values can be described as:

$$h\nu = E_L - E_K \tag{2.3}$$

where E_L and E_K describe the shells from which the transition occured, $L \rightarrow K$ in this case. In this equation and previous calculations the binding energies take a negative value to remain consistent with a quantum mechanics perspective.

The proportion of characteristic x-rays in a spectrum is minimal but increase as tube voltage increases; approx. 5% for a W anode at 80kV, but increases to approx. 10% at 100kV. This is an important facet of the mammography spectrum as the characteristic x-rays, which present as peaks on a spectrum, form the cornerstone from which to base an ideal mammography spectrum. The ideal mammography spectrum is one which minimises dose for the best diagnostic image quality, and this occurs around 20keV (Hogg et al., 2015). With appropriate filtering materials low and higher energy bremsstrahlung radiation can be mostly minimised as it generally doesn't contribute to image quality, but contributes to unnecessary dose while preserving the characteristic peaks. This leads to a much narrower energy band and closer to a more mono-energetic spectrum.

Figure 2.9 below gives a visual representation of how both bremsstrahlung and characteristic radiation appears in an x-ray spectrum.

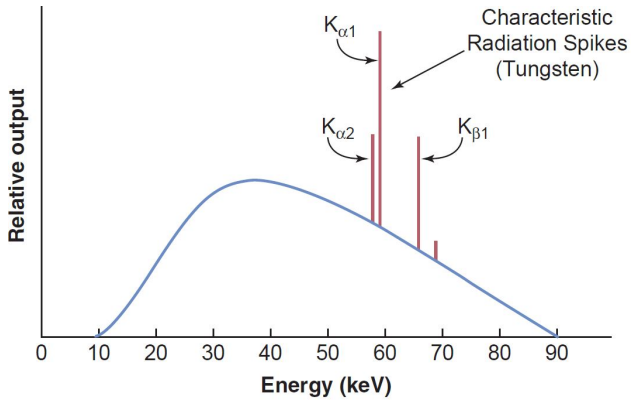

Figure 2.9: Combined spectrum of both bremsstrahlung and characteristic radiation from a W target. (Bushberg & Boone, 2011).

The quantity of filtering and kV of the x-ray beam can be very different from breast to breast as a thicker, more dense breast may need a higher kV with a thicker filter to obtain the beam penetration needed to produce an acceptable image. Where as a thinner, less dense breast may require less kV and filter thickness to achieve good subject contrast.

2.3.3 Attenuation

The attenuation of x-rays in matter is a product of several interactions, each contributes to the total linear attenuation and mass attenuation of a material, the level of contribution changes depending on x-ray energy. The three major interactions at mammography energy levels are coherent scattering, incoherent scattering and photoelectric absorption.

Coherent or Rayleigh scattering can be thought of as a classical interaction between the electromagnetic wave of the x-ray and the entire atom's electrons. The oscillating electric field excites the electrons which vibrate in phase with the electric field, the electrons cumulatively emit radiation equal in wavelength to the incident electromagnetic wave. This is a non ionizing process, hence no energy is transferred to electron kinetic energy (H. E. Johns & Cunningham, 1983).

From a quantum mechanics perspective incoherent or Compton scattering can be described as a collision between a photon with energy $h\nu$, and an electron generally in an outer atomic shell; this electron is often referred to as a "Free" electron. This collision is a two fold process whereby some energy is transferred to the electron as kinetic energy E, and the remaining energy is scattered as a photon with energy $h\nu'$. Thus from energy conservation $h\nu = h\nu' + E$, however because momentum must be conserved the angles at which each is scattered is dependant on the angle of collision (H. E. Johns & Cunningham, 1983). By applying these rules, the energy of the scattered photon $h\nu'$ and energy of the scattered electron, E, can be calculated if the angle of the scattered photon, θ, and the energy of the incident photon, $h\nu$, is known.

$$E = h\nu \frac{\alpha(1 - cos\theta)}{1 + \alpha(1 - cos\theta)} \tag{2.4}$$

$$h\nu' = h\nu \frac{1}{1 + \alpha(1 - cos\theta)} \tag{2.5}$$

where $\alpha = h\nu/511\text{keV}$, and 511keV is the rest mass energy of the electron (H. E. Johns & Cunningham, 1983; Khan & Gibbons, 2014). This concept of an angular distribution of scatter is important as Compton scattering in

tissue dominates interaction probabilities at mammography energies which affects image quality, and other processes such as backscatter. As an example it can be shown that the scattered photon and scattered electron obtain their minimum and maximum energies, respectively, when $\theta = 180°$:

$$E_{max} = h\nu \frac{2\alpha}{1 + 2\alpha} \tag{2.6}$$

$$h\nu'_{min} = h\nu \frac{1}{1 + 2\alpha} \tag{2.7}$$

where the relationship between the scattered electron angle and photon angle is:

$$\cot \phi = (1 - \alpha) \tan \left(\frac{\theta}{2}\right) \tag{2.8}$$

(Dance et al., 2014; H. E. Johns & Cunningham, 1983; Khan & Gibbons, 2014).

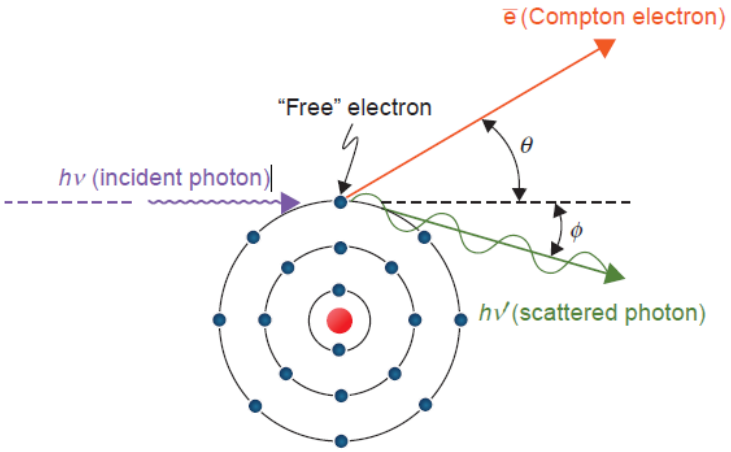

Figure 2.10: Illustration of a Compton interaction. (Khan & Gibbons, 2014).

From these results it is straight forward to deduce that the energy of resulting backscatter, where $\theta > 90°$, of a mammography x-ray beam or general radiology beam, is significantly lower than the incident beam. Conversely as θ tends to 0°, the resulting forward-scatter, $\theta < 90°$, energies tend closer to the incident x-ray energy, i.e. if $\theta = 0°$ then $h\nu' = h\nu$ and $E = 0$. Although these three, the Compton relations, form a description of the interaction kinematics, they offer no information on the Compton cross-section, or probability of interaction. The probability of a Compton interaction for a photon of energy $h\nu$ into a solid angle $d\Omega$ at an angle of θ can be described by the Klein–Nishina formula; this is the differential scattering cross-section:

$$\frac{\mathrm{d}\sigma_{KN}}{\mathrm{d}\Omega} = \frac{r_0^2}{2}(1+\cos^2\theta)f_{KN} \tag{2.9}$$

where f_{KN} is:

$$f_{KN} = \left\{\frac{1}{1+\alpha(1-cos\theta)}\right\}^2\left\{1+\frac{\alpha^2(1-cos\theta)^2}{[1+\alpha(1-cos\theta)][1+\cos^2\theta]}\right\} \tag{2.10}$$

Here $f_{KN} < 1$, if $f_{KN} \to 1$ then $\mathrm{d}\sigma_{KN}/\mathrm{d}\Omega \to$ the Thompson scattering cross-section, i.e. $h\nu' \to h\nu$ or $\alpha \to 0$ (Dance et al., 2014; H. E. Johns & Cunningham, 1983; Turner, 2008). Here the total Compton cross-section is obtained by integrating $\mathrm{d}\sigma_{KN}/\mathrm{d}\Omega$ over boundary conditions $(0, \pi)$.

$$\sigma_{KN} = 2\pi r_0^2\left\{\left\{\frac{1+\alpha}{\alpha^2}\right\}\left\{\frac{2(1+\alpha)}{1+2\alpha}-\frac{ln(1+2\alpha)}{\alpha}\right\}+\frac{ln(1+2\alpha)}{2\alpha}-\frac{1-3\alpha)}{(1+2\alpha)^2}\right\} \tag{2.11}$$

The previous limiting conditions for $\mathrm{d}\sigma_{KN}/\mathrm{d}\Omega$ hold for σ_{KN}.

The purpose for describing the Compton cross-section in more detail than would ordinarily be accepted is that for the purposes of this project the Monte-Carlo programme, Geant4, places a large requirement on the accuracy of these cross sections, of which it offers a range of cross-section datasets for one to use. So to understand the mechanism a little more deeply, as Compton scattering is the major interaction of dose deposition in tissue, it may give the reader more of an appreciation of the origin of dose measurements. However, photoelectric absorption also plays a role in dose deposition, and in particular filter beam transmission.

Photoelectric absorption is essentially the same process described in section 2.3.2 where after an inner orbital electron is ejected, its vacancy is filled by an outer orbital electron thus emitting an x-ray equal in energy to the difference in the orbital electron bound energies. However, when considering x-ray absorption through the photoelectric effect, instead of an incident electron as discussed in section 2.3.2, an incident x-ray is totally absorbed by the atom and the excess energy is transferred to a bound orbital electron. If the energy of the incident photon is equal to, or higher than a bound electron

then there is a probability that an electron may be ejected, thus leading to the process of x-ray production described earlier from the photoelectric effect (H. E. Johns & Cunningham, 1983; Khan & Gibbons, 2014).

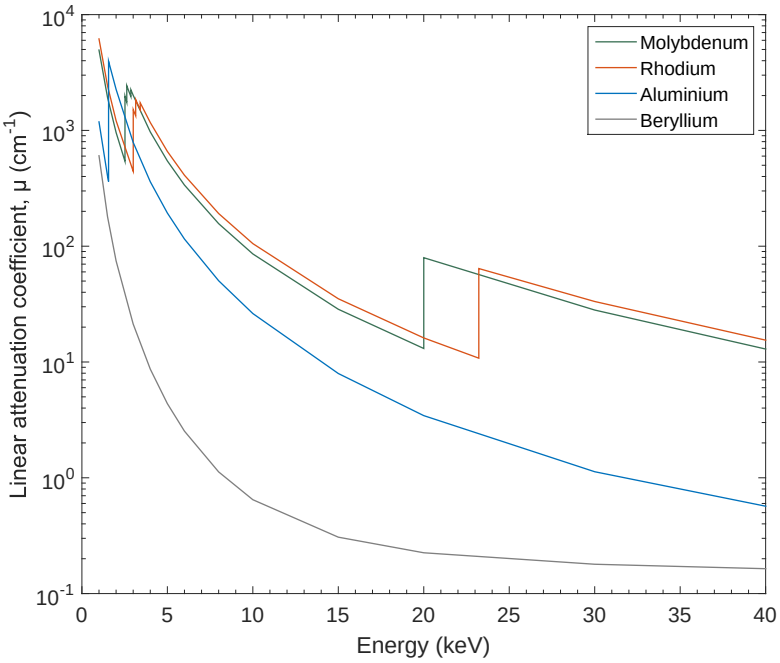

Figure 2.11: Linear attenuation coefficients for relevant mammography filter material. Data from Hubbell and Seltzer (1995).

As with other x-ray interactions that contribute to a total attenuation of photons, photoelectric absorption also carries its own unique cross-section. However, it is not quite as straight forward to describe mathematically due to significant discontinuities occurring at discrete energy values specific to the material. Figure 2.11 shows a number of common filter materials used in mammography units, but of note are the Mo and Rh attenuation plots where a sharp vertical rise is observed. These discontinuities are a function of photoelectric absorption which occur, in this plot, at the K-edge energy of the material. This points to an energy dependence on the probability of photoelectric absorption.

Starting at the higher energies of the figure it can be observed that a sharp decline in attenuation at about 20keV for Mo, and 23keV for Rh (exact figures are 20.002keV for Mo, and 23.229keV for Rh (Bearden, 1967)).

Below these discontinuities the incident photons carry insufficient energy to eject a K-shell electron, thus the probability of such an interaction decreases significantly and the attenuation coefficient decreases accordingly; photoelectric interactions are thereafter limited to the L and M shells. Of note is the steady decline in the attenuation coefficient, which is a function of the contribution of the photoelectric effect, as energy increases until another atomic shell energy limit is reached. At this energy limit the K-shell electrons become much more important and effectual in terms of attenuation than that of the L or M shells.

If the plot was extended to higher energies, one could observe an approximate relationship of attenuation versus energy. This would show that the apparent photoelectric cross section is approximately proportional to $1/(h\nu)^n$ where for higher Z materials $n \approx 3$ (Dance et al., 2014; H. E. Johns & Cunningham, 1983). To contrast, Compton scattering involves 'free' electrons thus its cross-section is independant of Z and relies solely on the materials electron density:

$$\rho_e = (\text{electrons}/g)\rho_{material} = \text{electrons}/cm^3 = \frac{N_A Z}{A} \tag{2.12}$$

where N_A is Avogadro's number $= 6.022 \times 10^{23}\text{mol}^{-1}$, and A is the atomic weight (H. E. Johns & Cunningham, 1983).

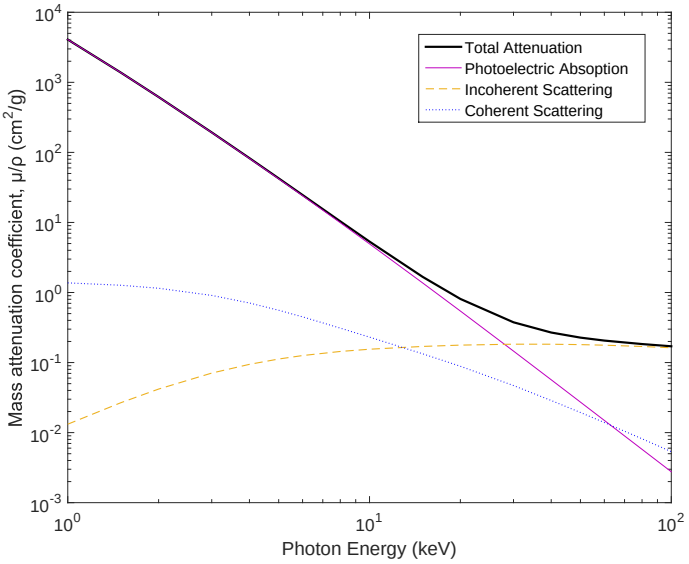

Figure 2.12: Mass attenuation coefficients of water for each of the interactions discussed. Data from Berger et al. (2011).

The total attenuation is a function of all the interactions mentioned, which differ in cross-section depending on E and Z. Figure 2.12 is an example of how they change in water for relevant diagnostic energies.

Each interaction has its own attenuation coefficient, μ, and mass attenuation coefficient, μ/ρ, as a function of energy. The total mass attenuation coefficient can therefore be described as a sum of the individual coefficients:

$$\left(\frac{\mu}{\rho}\right)_{Total} = \left(\frac{\tau}{\rho}\right)_{photoelectric} + \left(\frac{\sigma_{coherent}}{\rho}\right)_{coherent} + \left(\frac{\sigma_C}{\rho}\right)_{Compton} \tag{2.13}$$

where τ, $\sigma_{coherent}$ and σ_C represent the relevant linear attenuation coefficients (H. E. Johns & Cunningham, 1983; Khan & Gibbons, 2014). It must be noted that one other interaction, pair production, should be apart of this sum, (π_{pair}/ρ), however at diagnostic energies it is not relevant and will not be covered here.

Figure 2.13 highlights how x-ray attenuation differs between a high Z material and that of low effective Z material, and the different interactions responsible for their curves.

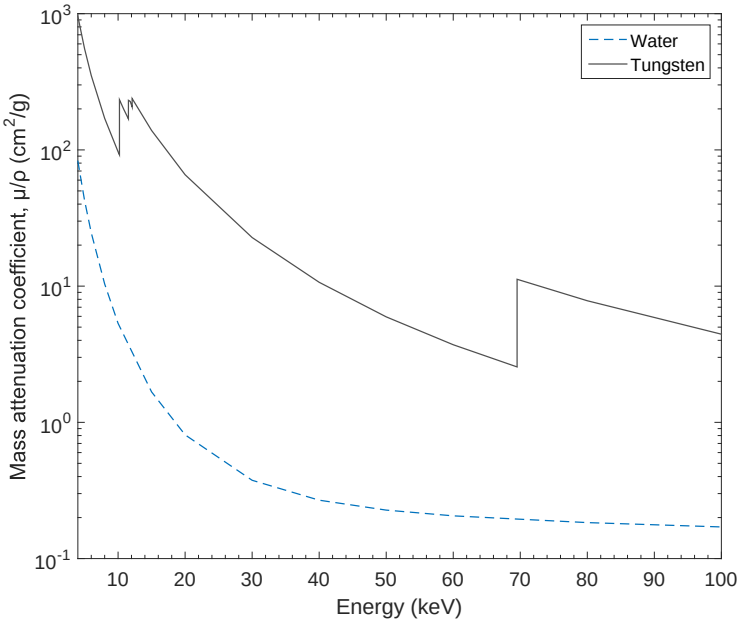

Figure 2.13: Comparison of mass attenuation coefficients for a high Z material, W, and low Z material, water. Data from Hubbell and Seltzer (1995).

The relative percentage of interactions that originate from a given process can be calculated from the following; in this case the relative percentage of photoelectric interactions:

$$100\tau/(\tau + \sigma_{coherent} + \sigma_c) = 100\frac{\tau}{\mu} \tag{2.14}$$

Applying equation 2.13, Table 2.2 can be compiled for the approximate energies of this project:

Table 2.2: Relative importance of photoelectric (τ), coherent ($\sigma_{coherent}$) and Compton (σ_C) attenuation in water by process (H. E. Johns & Cunningham, 1983; Khan & Gibbons, 2014).

	% **Interaction by process**			% **Energy Transferred**	
$h\nu$(keV)	Coherent	Compton	Photo Elec	Compton	Photo Elec
10	4.5	3.1	92.4	0.1	99.9
15	8.5	10.8	80.7	0.4	99.6
20	11.6	23.3	65.1	1.3	98.7
30	13.0	50.7	36.3	6.8	93.2
40	11.0	69.9	19.4	19.3	80.7

2.3.4 Radiation Dosimetry in Mammography

In the previous section it was described how the transfer of energy occurs through an interaction with an x-ray photon to a material, whereby an interaction generally results in an excitation or ionization of an atom. But what wasn't described clearly was the energy transfer of the ejected electron(s) in the medium.

This initial energy transfer from the incident photon to an atomic electron is the process known as *kinetic energy released in the medium* or Kerma. This describes the amount of energy transferred to charged particles per unit mass; this is the result of the photoelectric or Compton interactions previously discussed. Although the ejected electron after one of these interactions is then free to deposit its energy elsewhere, the definition of kerma is the energy

transfer from uncharged particles to the medium, thus only the initial photon-medium interaction is relevant. Taking kerma being equal to the energy transferred per unit mass $\mathrm{K} = dE_{tr}/dm$:

$$\mathrm{K} = \Phi\left(\frac{\mu}{\rho}\right)_Z dE_{tr} = \Psi\left(\frac{\mu_{tr}}{\rho}\right)_Z \tag{2.15}$$

where Φ is the photon fluence, and dE_{tr} is the total kinetic energy liberated to charged particles from the incident photon in a mass equal to dm. However the product $\Phi(\mu/\rho)$ reduces to the photon energy fluence Ψ, but invokes the mass energy transfer coefficient (μ_{tr}/ρ).

These equations describe the general case where a beam of photons is mono-energetic, but in practice a kerma calculation would be taken from a spectrum, thus a kerma spectrum calculation would require the summation of all kerma contributions from all energies in the spectrum. As described previously (μ/ρ) is energy dependant, accordingly (μ_{tr}/ρ) follows a similar energy dependence:

$$\mathrm{K}_{total} = \sum_{h\nu} n_{h\nu}\Phi_{h\nu}\left(\frac{\mu_{tr}}{\rho}\right)_{h\nu,Z} \tag{2.16}$$

where $n_{h\nu}$, $\Phi_{h\nu}$ and $(\mu_{tr}/\rho)_{h\nu,Z}$ is the number of photons, photon energy fluence, and mass energy absorption coefficient at specific photon energy $h\nu$, respectively. It must be noted that the mass attenuation coefficient and mass energy absorption coefficient are also dependant on Z.

Energy loss through ionisation is only one energy transfer mode from collisional interactions, but energy transfer can take place from radiative process such as bremsstrahlung from secondary particles. The total kerma can, therefore, be thought of as the sum of both collisional and radiative kerma processes:

$$\mathrm{K}_{total} = \mathrm{K}_{col} + \mathrm{K}_{rad} \tag{2.17}$$

Absorbed dose is a close relative to collisional kerma, this makes it an especially useful quantity as it is straight forward to calculate. The main difference between absorbed dose and kerma is that they don't occur at the same location. Where kerma considers photon energy transferred to kinetic

energy of charged particles (ionisation processes), absorbed dose takes into account the quantity of energy retained in the medium, including radiative processes. That is to say that kerma is the location of the primary energy transfer from the incident photon beam, where absorbed dose is concerned with the entire volume in which the kinetic energy is spent.

The only way in which both kerma and absorbed dose can be related is when an equilibrium exists between the two quantities. Kerma takes into account the transfer of energy that sets a charged particle in motion. Once that charged particle is in motion, it will begin to lose energy through a number of interactions, eventually coming to rest. Consider an electron that is set in motion and consequently enters a volume but loses all it's energy and comes to rest within this volume - in this case the absorbed dose in the volume is affected, but there is no affect on kerma. One can therefore deduce that for kerma and absorbed dose to be directly related, the quantity of electrons entering said volume must equal that leaving; this is called electronic equilibrium, charged particle equilibrium (CPE) or complete electron equilibrium, Figure 2.14 depicts this process.

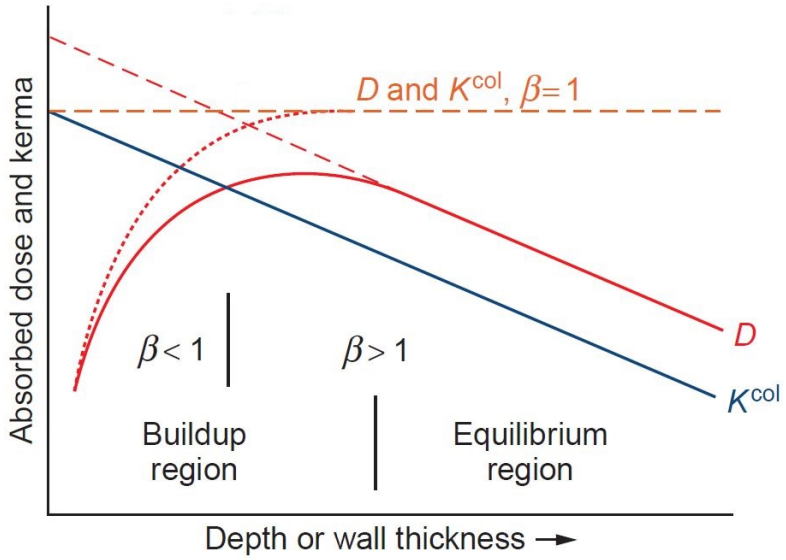

Figure 2.14: The relationship between collisional kerma (K^{col}) and absorbed dose (D) with and without CPE (Khan & Gibbons, 2014).

In the case of air, where kerma measurements have been calculated throughout this project and has a low effective Z, CPE can be realistically achieved. If $\beta = \mathrm{D}/K_{col}$ (ratio of dose to collisional kerma), then:

$$\mathrm{D} = \Psi \frac{\mu_{en}}{\rho} \beta \tag{2.18}$$

where μ_{en}/ρ is the mass energy absorption coefficient. However:

$$\frac{\mu_{en}}{\rho} = \frac{\mu_{tr}}{\rho}(1 - g) \tag{2.19}$$

where g is the portion of energy lost to radiative processes (H. E. Johns & Cunningham, 1983; Khan & Gibbons, 2014). But air has a low effective Z and radiative processes are dependant on Z^2, thus for $\beta = 1$, g = 0:

$$\mathrm{D} = \Psi \frac{\mu_{en}}{\rho} \beta = K_{col} \tag{2.20}$$

As $g = 0$, $K_{rad} = 0$, therefore $K_{total} = K_{col}$. If any one of the provisos change such that the conditions for CPE is not achievable or $0 < g < 1$, dose and kerma interchangeability fails.

This leads on to a previously mentioned unique dosimetry quantity specific to mammography, the mean glandular dose (MGD). As mentioned the glandular component of the breast is the most radio-sensitive and the site of carcinogenesis, however dose deposition to the glandular tissue is a function of depth. Glandular tissue further from the beam entrance in the breast will receive mixed values of dose, thus making a precise dose measurement difficult and so the MGD was developed. The MGD can be quantified as a product of the incident air kerma (IAK), or entrance skin air kerma (ESAK), and conversion factors. The conversion factors can vary depending on geographic location, equation 2.21 is the protocol adopted for European dosimetry models developed by Dance (1990); Dance et al. (2000); Dance, Young, and Van Engen (2010).

$$\mathrm{MGD} = Kgcs \tag{2.21}$$

Here K is the IAK which is measured at the point of entrance into the breast minus backscatter, where g, c and s are tabulated conversion factors published in the aforementioned papers. g is incident air kerma to mean glandular dose conversion factor (g-factor) for a standard 50% adipose to

50% glandular breast; c is a conversion factor that corrects for a glandularity other than 50%; and s is a spectral correction for any spectrum different from that of an Mo anode and Mo filter; where a Mo anode and filter are used $s = 1$.

The protocol adopted by the Australasian College of Physical Scientists and Engineers in Medicine (ACPSEM) is that developed by Sobol and Wu (1997); Wu, Gingold, Barnes, and Tucker (1994). Here they describe the MGD ($\overline{D}_g$) as a product of a *normalised* average glandular dose which is defined as the average glandular dose per unit incident air kerma ($\overline{D}_{gN}$), and the ESAK ($X_{_{ESAK}}$). The unit of $\overline{D}_{gN}$ is mGy dose/mGy incident air kerma and therefore is a unit-less conversion factor, $X_{_{ESAK}}$ has the units of mGy:

$$\overline{D}_g = \overline{D}_{gN} \times X_{_{ESAK}} \tag{2.22}$$

It is important to note that the factor $\overline{D}_{gN}$ is calculated using a Monte Carlo simulation developed by Wu, Barnes, and Tucker (1991); Wu et al. (1994). The conversion factor is dependant on the parameters used in the image acquisition which are: HVL, anode material, breast composition and breast thickness. Sobol and Wu (1997) details the parameterisation of $\overline{D}_{gN}$ as a function of the above parameters which are independantly dependant on specific parameters. This could be viewed as an amalgamation of factors similar to Dance (1990), but in the context of Sobol and Wu (1997) the effort was to provide parametrised models. Equation 2.23 below describes these functions and gives an insight on the premise behind a normalised average glandular dose:

$$D_{gN} = \mathrm{C}\{\mathrm{V}\{\mathrm{D}\{\mathrm{H}(\mathrm{HVL}), d\}, \mathrm{kVp}\}, c\} \tag{2.23}$$

the $\mathrm{C}(..., c)$ indicates D_{gN} is a function of breast composition which depends on all the parameters within the brackets, those being: kVp, HVL and d. Similarly D_{gN} is also a function of tube potential $\mathrm{V}(..., \mathrm{kVp})$ which is dependant on HVL and d; it's a function of breast thickness $\mathrm{D}(..., d)$ that depends on HVL; and D_{gN} is a function of HVL $H(HVL)$ that depends solely on HVL values.

Any MGD calculations made throughout this project, the tables from Wu et al. (1994) or the parametrised version from Sobol and Wu (1997) were used as it falls in line with ACPSEM's protocols.

2.4 Literature Review

Data availablility on an equivalent material thickness, be it water or otherwise, as a function of breast thickness and breast density is few and far between. However there have been some researchers who have tabulated results directly, but in most cases as an indirect consequence of their results and how they have been presented.

Dance (1990) main theme was to calculate MGD conversion factors for a range of breast thicknesses, the results were presented for a range of breast thickness for a standard breast. The standard breast was defined as a 16cm diameter semi-circular cross section of density 50% glandular 50% adipose tissue with a 0.5mm outer layer of adipose tissue, the standard breast is also 4.5cm thick. Dance (1990) proposed to calculate the MGD conversion factors for a thickness of Perspex as opposed to the standard breast, this was due to the practicality of constructing a suitable phantom to replicate the standard breast accurately; this was the motivation to find a Perspex, or PMMA, equivalent thickness. To obtain accurate results a p factor was proposed to convert incident air kerma for Perspex to the standard breast.

The method in which this was calculated was to simply take the energy absorbed in the image receptor per unit incident air kerma, without backscatter, for the standard breast versus that for the Perspex breast. The tabulated results were an average taken between the ratio described above for no-grid and grid set-ups, however it was noted that there was little variation in each case, in fact the maximum noted variation in equivalent thickness as a function of differing spectra and grid was $\pm 1.5\%$. The results for this paper ultimately showed the standard breast had a linear dependence on the equivalent Perspex thickness which can be calculated as (Heggie et al., 2012):

$$\begin{matrix} Standard\ Breast \\ Thickness \end{matrix}(mm) = 1.047 \times \begin{matrix} Perspex \\ Thickness \end{matrix}(mm) + 1.78 \qquad (2.24)$$

Further to Dance (1990), Dance et al. (2000) extended the results found previously to calculate conversion factors over a range of breast glandularity from 100% adipose to 100% glandular for a greater range of mammography spectra, also increasing the compressed breast thickness to between 2-11cm;

previously 2-8cm. Consequently it was found that as the previous study was based on a 50% glandular breast over a range of breast thickness, 2-8cm, an equivalent PMMA thickness would lead to perturbations in dose for thinner and thicker breasts. This is due to breast glandularity having a dependence on breast thickness, Dance et al. (2000) therefore documented a trend in their study population as:

$$Glandularity(\%) = at^3 + bt^2 + ct + d \tag{2.25}$$

where a, b, c and d are coefficients of the fitted polynomial which is dependant on age range, 40-49 years or 50-64 years. This polynomial fit proved to be generally correct, albeit with some outliers, for larger surveys conducted by Geeraert, Klausza, Mullera, et al. (2012) which included populations from Asia Pacific, Europe and North America using GE Senographe DS and GE Essential mammography units.

From the studies mentioned in Dance et al. (2000) which confirmed a glandular density dependence on breast thickness, an equivalent PMMA thickness was tabulated for a typical glandularity, which varied as a function of thickness. As a further extension to Dance et al. (2000), a study by the same author, Dance, Young, and Van Engen (2009), added additional factors for spectra being introduced with DR mammography, those with W anodes, and validated the PMMA equivalent thickness for typical breasts.

The methodology and PMMA equivalent thickness results obtained from these papers will be considered in this project, and may be utilised to aid in converting their PMMA equivalent thickness to a water equivalent thickness during validation of transmission data.

2.5 Geant4 Monte-Carlo Simulation

The first Monte Carlo theorems were produced by Stanislaw Ulam while working on neutron diffusion as part of the nuclear weapons project at Los Alamos National Laboratory. But as the entirety of their work was classified, the first published work was made available in 1949 in Metropolis and Ulam (1949). It describes the Monte Carlo method as solving deterministic problems through the use of random population sampling or random

event sampling. An historic example of this is the Buffon's needle experiment, where pi (π) can be estimated by dropping a needle of length, L, over equidistant parallel lines with separation, t, a large number of times; $L \leq t$. Without derivation, the probability that the needle crosses any one parallel line is:

$$P = \frac{2L}{t\pi} \tag{2.26}$$

but now taking n as the number of times the needle has been dropped and h as the times the needle crosses a parallel line, P can be approximated as h/n; thus rearranging equation 2.24:

$$\pi \approx \frac{2Ln}{th} \tag{2.27}$$

This experiment was performed in 1901 by Italian mathematician Mario Lazzarini [1], he obtained an approximation equal to 355/113 which is accurate to 10^{-6} (Badger, 1994). This was a good example of how the random sampling of events can lead to a deterministic value, however in the case of a large complex system such as radiation and particle transport, Markov Chain Monte Carlo methods are more appropriate. A Markov chain is where the random sampling comes from a probability distribution and the outcome of an event is based on the state of the previous event. The development of specific computer packages to model such systems, one being Geant4, has led to solving large scale radiation and particle transport problems being much more manageable.

Geant4 was developed by CERN on the back of what was already available in Geant3 as part of a major international collaboration to construct a package based on C++ object oriented technology. This was ultimately completed and available for use by 1999 where it is consistently updated and improved by the collaborative effort of over 100 scientists worldwide (Agostinelli et al., 2003).

As Geant4 is based on an object oriented programming language, it offers a vast array of flexibility in user design that accommodates varying experimental requirements. A key feature is that the the physics implementation

[1] Lazzarini's experiment has been somewhat criticised as to the accuracy which it was carried out, and scepticism still remains as to the precision of his result.

is clearly defined and is available for user confirmation. Being modular in design, it allows the user to customise their components to whatever requirement is needed. These facets of Geant4 enable the tool-kit to possess a hierarchical structure where the key domains and sub-domains are shown in Figure 2.15.

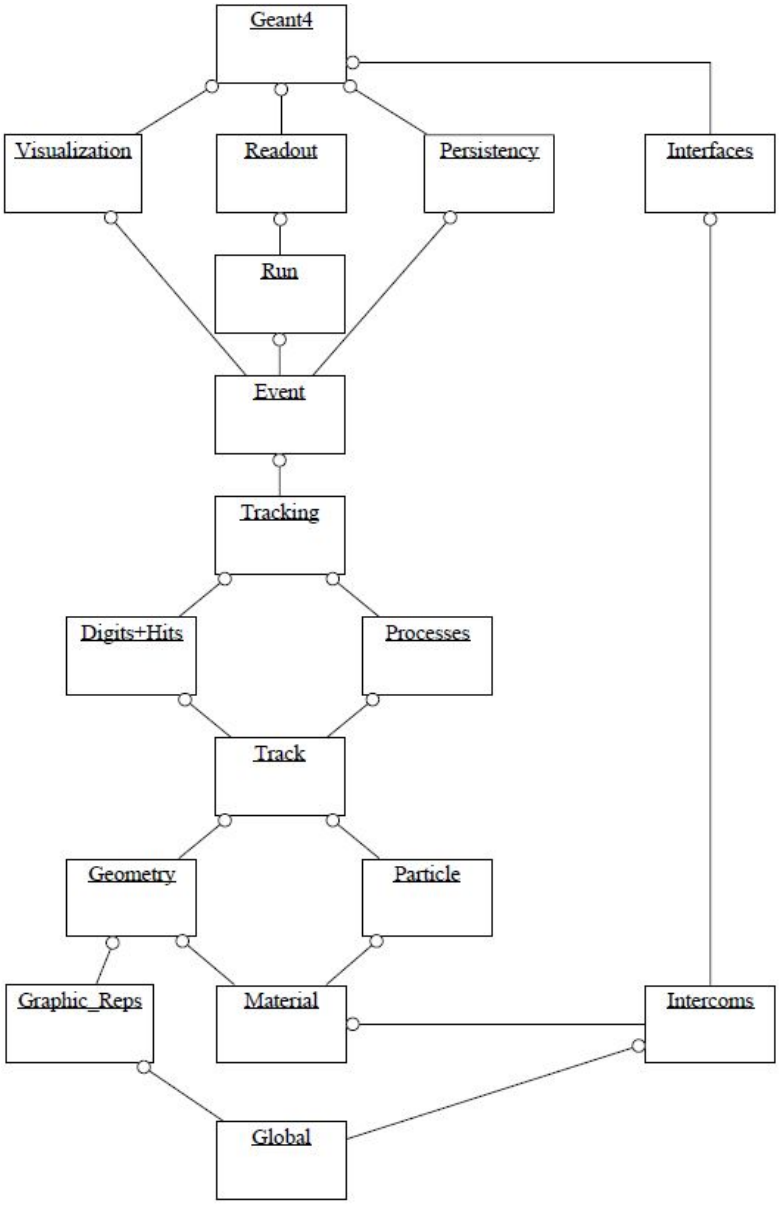

Figure 2.15: The Top Level Category Diagram of the Geant4 tool-kit. The open circle on the joining lines represents a "using" relationship; the category at the circle end uses the adjoined category (Agostinelli et al., 2003).

The domains expressed in Figure 2.15 are the requirements to successfully simulate the passage of particles through matter, and from these domains came the development of the class categories in the shape of class files with associated working groups. As such the minimum mandatory user classes required to compile and run a simulation with Geant4 are:

- *G4VUserDetectorConstruction*
  This user class is used to model the geometry of the simulation which might include defining materials, detectors and visualisations.

- *G4VUserPhysicsList*
  A physics list encompasses the definition of the physical processes, particles and potential physical limiting parameters such as energy limits.

- *G4VUserPrimaryGeneratorAction*
  This class is required to produce the primary particles, be it from a particle generator or phase-space file, and to define their properties.

With these three user classes there is no pre-defined specific function, but are instead abstract definitions where a user is required to define their own classes. As well as these required user classes, optional user classes allow the user to manipulate the behaviour of the simulation tailoring the output to their requirements:

- *G4UserRunAction*
  Class used to define actions taken at the start and end of every run.

- *G4UserEventAction*
  Class used to define actions taken at the start and end of every event.

- *G4UserStackingAction*
  To define the users access to the track stacks.

- *G4UserTrackingAction*
  To customise the actions taken at start and end of every track.

- *G4UserSteppingAction*
  To define actions to be taken at every step.

The relationship between the required and optional user classes highlight the hierarchical and commutable design of Geant4 where one can infer a unidirectional dependency link between classes as depicted in Figure 2.15.

Visualisation is also a user defined optional preference. Geant4 is able to link it's output to secondary external software used to not only visualise ones simulation, but also tailor the output to the users requirements. This includes visualisations from OpenGL, DAWNFILE, RayTracer, OpenInventor and Qt to name a few. Data output can also be tailored through secondary software such as R^2 and Root.

The flexibility of Geant4 allows the user to take full control over their simulation, the parameters used, and the output. As well as being open-source, the knowledge that it was developed through a major international conglomerate of scientific contributors and is continually improved upon makes it the most suitable Monte Carlo package for this project.

Chapter III

Materials and Methods

The materials of this project were predominantly computer software based: Geant4, MATLAB, SpekCalc and IPEM78 (Cranley, Fogarty, & Desponds, 1997) spectrum generator, as well as other Linux and Windows based supplementary software. The methods employed were developed using this software that are specific to a mammography simulation, data collection and analysis.

3.1 Geant4

Geant4, as described in section 2.5, is a C++ based Monte Carlo particle physics package which can be installed on a Linux or Windows operating system. To install Geant4 on either a Windows or Linux platform with their associated secondary software such as Class Library High Energy Physics (CLHEP), VMware (Windows only), and CMake presents a reasonably significant challenge. Despite attached install and set-up instructions achieving operational software where basic introductory examples worked to a satisfactory standard proved particularity non-trivial.

For a short initial phase of this project Geant4 and its associated libraries was installed on a Windows platform. However significant issues arose with the linking of CLHEP and CMake to Geant4, which ran through VMware, that proved too time consuming to attempt a concerted effort to solve and as such a Windows Geant4 platform was abandoned. This was the first attempt to install Geant4 on any operating system, and at the time a very rudimentary knowledge of the associated software, libraries and C++ generally was known hence a Linux platform was preferred.

There are many open-source Linux operating systems available and for the purposes of this project any one of them would have been suitable, Ubuntu was ultimately chosen for no other reason other than it was informally rec-

ommended as a stable, visually appropriate system. Linux, however, is quite different to that of Windows and requires its own learning curve to use on a semi-useful basis, but this was achieved during the process of installing Geant4. The installation instructions proved just as challenging to have work correctly as the Windows instructions, but an extremely helpful tutorial video on the installation of Geant4 on Ubuntu was found which enabled significant progress in a short period to have CLHEP and CMake installed correctly. Geant4, on the other hand, was only partially installed as versions of CLHEP, CMake and Geant4 clashed as the version of Geant4 required a particular version of both CMake and CLHEP to run properly. To solve this the version of Geant4, CLHEP, and CMake were degraded to versions which were compatible. Subsequently, the first successful install of Geant4 on a Linux system was achieved to where basic introductory examples were compiled and working as required. This marked the first significant task completion of the project as it enabled the progression of the project towards the goal.

3.1.1 Geometry Construction

Geant4 encourage users to adopt one of their examples on which to develop a unique simulation as they all have the mandatory user classes, and some optional user classes which forms a compilable code that runs as expected. It is a matter of personal preference and experimental requirements on which example to develop, for this project the basic example B1 was selected. Example B1 included two very basic shapes for the purpose of accounting for energy deposition from an electron beam, dose is then recorded in a selected volume. The primary generator was an electron beam that was randomly generated over a particular area in the XY plane, and the detector was simply one of the material volumes; essentially example B1 was selected because of it's simplicity and ease of manipulation.

It must be noted before continuing that the project involves data collection from a number of locations in the Z direction of the beam, and at each point requires quite a significant amount of rearrangement of code in order to collect the required data. Therefore, instead of having one singular chunk

of code from which to manipulate as required, a varied set of code was developed in order to collect data at each point; this included code for specific test experiments.

X-ray tube and initial geometry: The x-ray tube was the first set of volumes to be constructed in the *Detector Construction* class, the anode dimensions had to be estimated as no specific tube data was available at the time. The anode was 10cm in diameter and 1.5cm in thickness, this was located in the geometry such that the focal spot was the position $(0, 0, 0)$ with an angle of 24 degrees. When sufficient data was made available to correctly simulate the anode's dimensions, the diameter and thickness remained unchanged, but the anode angle was moved to 22.5 degrees.

The electron beam was manipulated directly from the previous electron beam defined in the *PrimaryGenerator* class from example B1. Example B1's beam was, however, large in surface area so it had to be miniaturised such that the resulting beam formed a focal spot of 0.3mm upon contact on the anode. The beam origin was located such that the beam contacted the anode perpendicular to the middle of the anode's circumference surface, Figure 3.1 shows this. This was 2.5cm from the anode surface and at an angle of 22.5 degrees from the horizontal plane, or 112.5 degrees from the positive Z axis.

To properly replicate the conditions in an x-ray tube, the electron beam and anode were encased in a lead box, which also housed a vacuum environment. The wall on the positive Z axis was made from Beryllium located at Z=2cm with dimensions $4cm \times 4cm \times 0.69mm$; the thickness is specific to a GE Essential mammography unit.

Filter and compression paddle: Below the Beryllium window are the main beam attenuating volumes before the breast volume. The first is the filter which was located at $Z = 2.7cm$ with dimensions $6cm \times 6cm \times filter\_thickness$ where $filter\_thickness$ is user defined, and the second is the breast compression paddle. The compression paddle was made from Geant4 defined material *Perspex* which has the same elemental composition as PMMA. It's dimensions matched that of the maximum FOV, $24cm \times 30.7cm \times 1.5mm$, and was

located in the Z direction relative to breast thickness, i.e. a thicker breast would mean the compression paddle would be closer to the focal spot. However for certain experiment set-ups and testing the compression paddle was located as close to the focal spot as was required by the testing procedure.

Additionally, the Beryllium window, filter and compression paddle was located in the Y plane as to ensure the entire x-ray beam traversed through them. Both the Beryllium window and filter's dimensions far exceed the area of the beam at their respective Z locations, therefore an exact Y location wasn't required. The Y locations of both the Beryllium window and filter was $Y = 0cm$, however an exact Y location was a little more important with the compression paddle as it had to potentially encompass the maximum FOV, the Y location was therefore $Y = 12cm$. Figure 3.1 depicts the discussed initial geometry configuration and some aspects not yet mentioned. The compression paddle has been left out of the image as it becomes a vital geometric volume when designing breast transmission geometry.

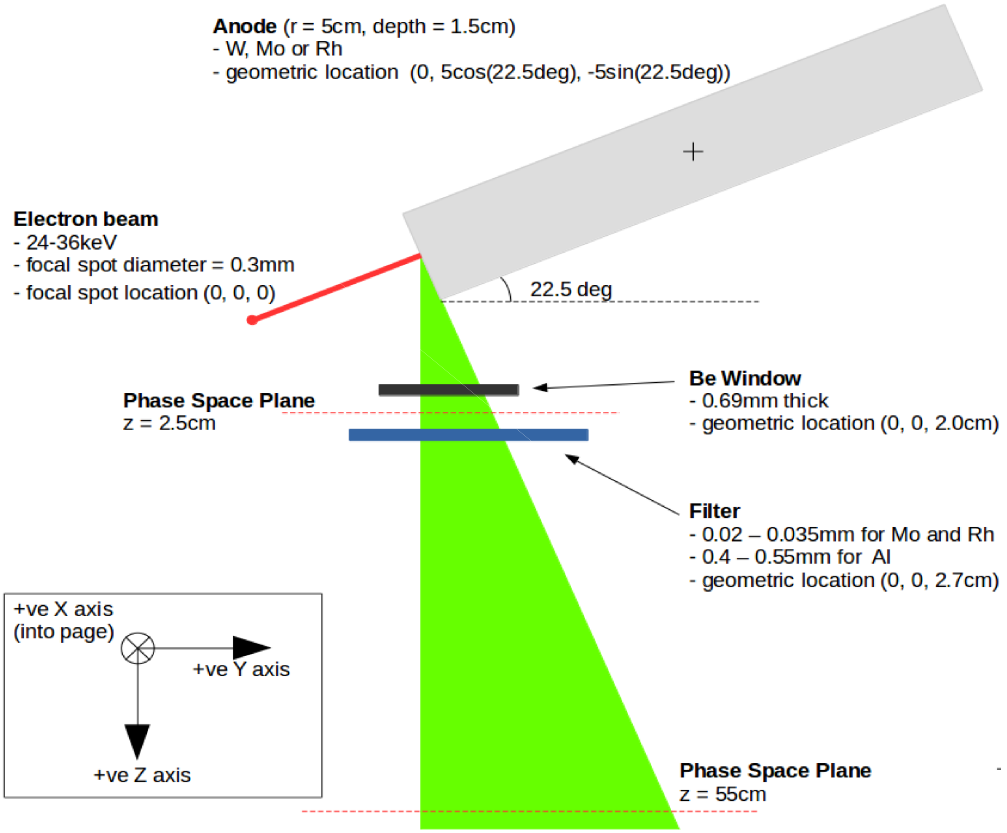

Figure 3.1: X-ray tube and associated geometry.

Parts of code for simulating the electron beam and the anode volume can be found in Appendix F.

The code developed up to this point is the basis for two particular aspects of the project, the first being to validate the physical processes the simulation is producing in the form of spectral analysis, and the second is to collect a set of unfiltered phase-space files at a point after the beryllium window. These two will be discussed in Section 3.2 and 3.3.1 respectively.

Breast and associated volumes: The remaining physical volumes that were configured in the *Detector Construction* were the breast, the skin layer, breast support, grid and the Thallium activated Caesium iodide (CsI(Tl)) scintillator. The breast was constructed to somewhat replicate a standard breast as described earlier in section 2.4, that being a breast with a radius of 8cm. However, a standard breast is defined as having a composition of 50% glandular 50% adipose tissue, and a 0.5cm layer of adipose tissue surrounding the breast apart from on the chest wall surface. As this projects purpose is to ascertain a water equivalent thickness, the breast composition was the Geant4 elemental description of water; a thin layer, 1.5mm, of skin was also added in place of the 0.5cm thick adipose tissue.

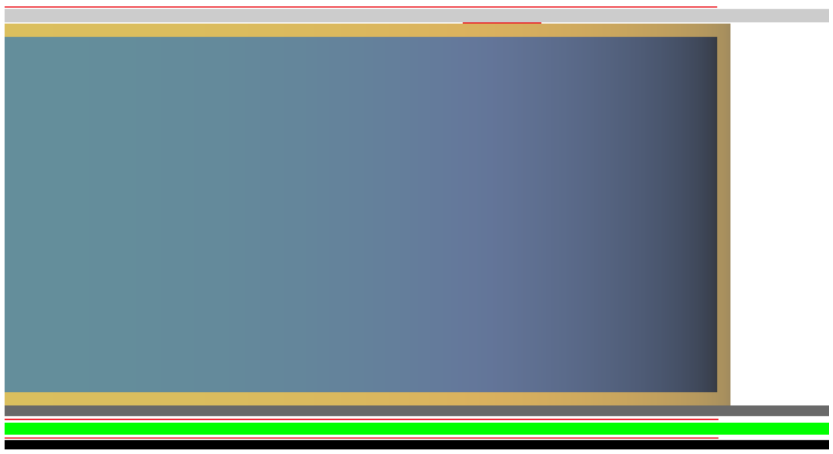

Figure 3.2: Side projection looking along the x-axis of the breast and associated volumes. From top to bottom the volumes are: breast compression paddle, cranial skin layer, breast, caudal skin layer, breast support, grid (bright green), and CsI(Tl) scintillator. The thin red lines represent data collection planes which will be discussed in subsequent sections.

The breast's lower surface location remained in contact with the breast support at $Z = 65.05cm$ independant of breast thickness, while the XY locations were 0cm. The thickness of the breast was user defined, therefore the Z location of the upper surface and volumes associated with the upper surface (compression paddle, upper skin layer) varied with breast thickness.

The breast support was modelled to replicate Dance et al. (2000) as conclusive accurate data on breast support plates was difficult to obtain. The breast support's dimensions were, therefore, that of the maximum FOV and compression paddle in the XY plane but with a slightly altered thickness, $24cm \times 30.7cm \times 1.2mm$. It was constructed from carbon fibre, however Geant4 doesn't have a predefined carbon fibre material that can be used, so one had to be defined manually. Although carbon fibre is not 100% carbon, an overwhelming majority of it is and therefore the carbon fibre used in the breast support was constructed purely of carbon with a density of 1.45g/cm^3. The location of the top surface of the breast support is $Z = 65.05$ to match that of the lower surface of the breast, also the XY coordinates were $X = 0$ and $Y = 12cm$.

Below the breast support was the grid which consisted of lead septa arranged in a 2D focused linear pattern similar to that shown in 2.6. The angle of the septa in both the X and Y plane varied according to their relative location in said planes, the maximum angle occurred on the extremities of the FOV and an angle of 0 degrees occurs at both X and $Y = 0$. The following grid characteristics were taken from information published with a GE Essential mammography unit (General Electric, 2013) and applied to the simulated grid. The grid ratio was 5:1 and the grid frequency was $36lines/cm$, using the septa thickness of 0.025mm and the formula described in section 2.3.1, the septa spacing was 0.278mm which led to a septa height of 1.264mm. Some grids may have an inter-space material, but none was specified nor found for the grid used by the GE Essential so none was applied to the geometry.

The last volume as part of the breast transmission geometry was the CsI(Tl) scintillator, this volume was made from CsI and Tl with the proportions 99.6% CsI and 0.4% Tl; these proportions have been previously defined by examples provided by Geant4 and were adopted here. The location of the CsI(Tl) scintillator was $Z = 66cm$, the SID, at its upper most surface

and had the same XY location as the compression paddle and breast support. The XY dimensions were also the same as the compression paddle and breast support, but the thickness was $0.5mm$; the thickness was taken from Zhao, Ristic, and Rowlands (2004) which is of the higher end of that study, this was because mammography requires a good modulation transfer function (MTF). The CsI(Tl) scintillator will not be used directly to collect dosimetric quantities, the simulation of this volume is purely for continuity.

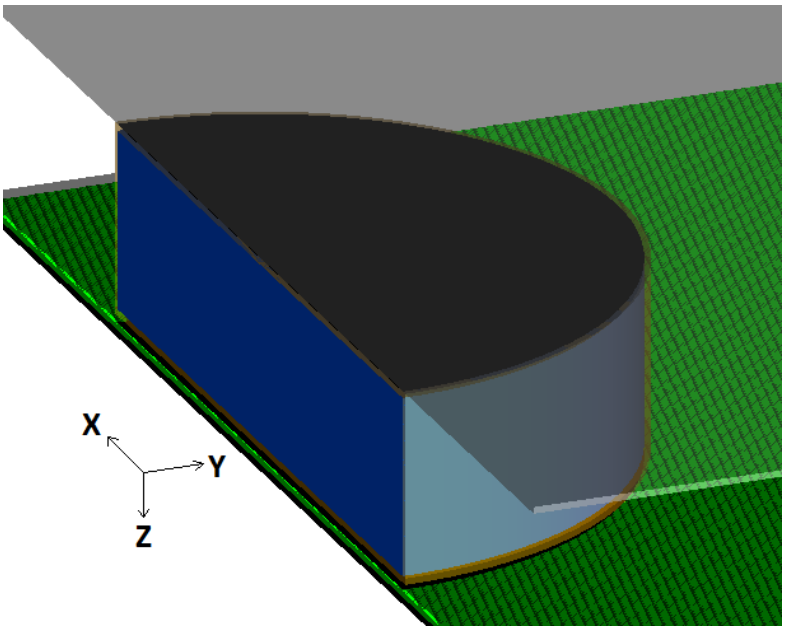

Figure 3.3: 3D projection of breast and associated volumes.

3.2 Initial Spectrum Validation

Validating the physical processes is a key step in ensuring the collected data is being produced by the correct simulated physical processes. The accuracy of the data stems not only from correct geometry construction, but also from the physics list being used by the user, and the set of data from the class library, CLHEP. Additionally, the method in which the data is collected can play a role in its validity, which will be discussed in a later section.

The validation spectra collected were from a W anode at 150kVp and 40kVp, these were chosen to highlight processes being simulated at both higher energies and lower mammography energies. The initial detector vol-

ume configuration was used without a compression paddle and filter in the beam. A detector volume, which consisted of a $1cm \times 1cm \times 0.001mm$ box that was placed at $Z = 10cm$, X and $Y = 0cm$ and was used to detect a photon passing through that volume and write it's energy to a text file. Five instances of the simulation ran simultaneously each simulating 2×10^9 histories, or electrons hitting the anode, giving a total of 10^{10} histories for both W150kVp and W40kVp. Although there was a large amount of initial histories, the efficiency of x-ray production is poor at these energies, and the sample spectra taken from the detector volume is only a small proportion of that which would be produced from sampling an entire point source spectra; the efficiency of these spectra and expected estimates will be discussed in Section 5.

In order to streamline the validation process, and subsequent data collections, a set of commands both built-in and user defined were used and exectued through a macro file which was called upon instigating a *run* (*/run /beamOn [# of histories]*).This proved the most efficient method to produce suitable results, and for the purposes of this section of the project, and for use in later sections, the anode material had a user defined command */mammo/anodeFilter/setAnodeMat* which comes from it's own user class, for altering geometric materials and volume parameters *DetectorMessenger*. An example of what a set of commands would look like in the validation macro file:

/mammo/anodeFilter/setAnodeMat G4_W
/gun/energy 150 keV
/run/beamOn 2000000000

/gun/energy 40 keV
/run/beamOn 2000000000

where */gun/energy* and */run/beamOn* are built in commands and *G4_W* is the material definition used by the user code. Note that the user command is only used at the start, it would only need to be reinstated if another command alters the geometry which may reset the current anode material.

Once the data was collected the data file was then imported into Mat-

lab where a histogram of the energies for the spectrum was plotted, and an appropriate line graph rendered from that. However the simulated spectrum needed to be validated against other accurate published material, and SpekCalc served those requirements. SpekCalc is a software program designed to calculate x-ray spectra from a tungsten anode which were validated against spectra produce by the BEAMnrc monte carlo program, and IPEM78 as an alternative. It boasts a wide array of tube potentials, anode angles and filter materials which are particularly valuable to medical physics. More can be read about SpekCalc in the follow publications: G. Poludniowski, Landry, DeBlois, Evans, and Verhaegen (2009); G. G. Poludniowski (2007); G. G. Poludniowski and Evans (2007).

The data from SpelCalc and the simulation were then compared in the form of a spectrum comparison, inspecting the general shape of the bremsstrahlung and the location of characteristic peaks. The data was then plotted against each other to produce a linear regression model of the data and obtain an R^2 and RMSE.

However, SpekCalc proves to be particularly unsuitable for energies below 15keV (this will be presented and discussed in section 4 and 5) so another form of validation that is accurate at low energies is required. IPEM78 was therefore used as a substitute to SpekCalc.

As an aside, IPEM78 was used to compare spectra produce by an Mo and Rh anode, both filtered and unfiltered, to ensure the spectral results were in line with what would be expected.

3.3 Data Collection

The methods used to collect data have already been partially discussed, but will be discussed more formally here. The methods used for data collection were in the form of phase space files, and detector volumes located at specific XYZ coordinates. The purpose of the phase space files was to provide a platform from which the beam characteristics are captured at particular locations throughout typical mammography transmission. The purpose for the location of the detector volumes was to simply collect both dosimetry

and spectral data depending on the detectors location.

3.3.1 Phase Space files

The International Atomic Energy Agency (IAEA) developed a stand-alone method of reading and writing particle information that can be used in Geant4 and other validated Monte Carlo codes. The writing facet of the code enables the user to record particle information at a user defined location in the form of an *IAEAphsp* file as part of a Geant4 simulation run. The phase-space reader enables the user to then read the information contained in the *IAEAphsp* file and produce primary particles within a Geant4 user simulation. The additional code to implement IAEA's phase-space occurs in the *RunAction*, *SteppingAction*, *EventAction* and *PrimaryGenerator* class files. The extent of the added code is minimal for the user to implement, but for a deeper understanding of IAEA's phase-space method the following articles are of use: Cortés-Giraldo, Quesada, Gallardo, and Capote (2009, 2012)

The first set of phase-space files were collected at $Z = 2.5cm$ which was located after the Beryllium window and before the filter, Figure 3.1 shows its location. The purpose for this location was to produce a suitable quantity of histories from a given spectrum to pass through the filter, which would lead to less variance in the filter transmission results (this will be discussed in Chapter 5). The phase-space file was produced from a simulation run consisting of 2×10^9 electron histories for each anode/energy combination. The anode material was Mo, Rh and W, and a range of tube energies were simulated for each anode material, 24kV to 36kV in 1kV increments; this meant 39 phase-space files were collected. These phase space files were collimated without the use of physical geometry. During collection a condition was instigated in the $G4IAEAphspWriter$ class file (used to write the phase-space file) that eliminated photons that fell outside the maximum FOV, at an SID of 66cm, if they were to carry on to the detector. In doing this the phase space files were specific to a mammography x-ray tube, and reduced the likelihood of scatter from adjacent collimators being recorded.

To use the phase-space files efficiently a user defined command was con-

structed that was added to a macro file which would define the phase-space file to be used. Because this affected the *PrimaryGenerator* class file, the additional command was produced in a *PrimaryGeneratorMessenger* class file which detailed it's function. The additional command looked like - $/mammo/SourceFile/setFile\ Mo28keV$, when the command was used with subsequent phase space files, the phase-space file name would take on a slightly altered structure with additional parameters such as filter material and thickness, and breast thickness.

The second set of phase space files were collected at $Z = 55cm$, which is just above the breast compression paddle when the breast is at it's thickest, 8cm. These phase-space files were produced by simulating 10^7 histories from the previous phase-space files collected above the filter. The purpose for these files was to obtain a spectrum closer to the breast in order to amplify the quantity of histories used to collect breast transmission data. It also meant there was an element of beam transmission (through the filter) that wasn't being simulated which led to faster simulation times.

The third and last set of phase-space files were recorded between the breast support and the grid. Unlike the two previous sets which encompassed the entire FOV, these were limited to a surface area slightly larger than the breast, a 9.4cm radius. A larger surface area was selected in order to collect any and all photons that may travel through the breast at all thicknesses. At a breast thickness of 8cm the maximum radius at which a photon would travel through any part of the breast volume was 9.28cm. These were collected in conjunction with obtaining breast transmission data which was collected using 2×10^9 histories from the second set of phase space files, hence some of the phase-space files were very large. The purpose for collecting these phase-space files was to not only collect spectral data, but also a means for future work that may include looking at grid transmission.

A depiction of the first two phase-space locations can be found in Figure 3.1, and the third in Figure 3.2 between the breast support and grid.

3.4 Detector Volumes

The detector volumes used in this project consisted of a thin volume located at specific locations to collect spectrum and dosimetry data. These were used to collect kerma measurements, as opposed to dose. Strictly speaking the detector volumes should be a volume where dose is measured, but a kerma measurement was selected instead.

This was due to a number of reasons, the first was that in order to gain an accurate dose measurement the detector volume would need to be approximately 2mm thick, which is in the order of an electrons range in air. With four possible detector volumes, three of which were integrated among the associated breast transmission volumes, the geometry would have to allow for a minimum of 6mm of geometry movement to accommodate them; this was too much of a perturbation for simulate accurate beam transmission.

The second reason was due to differences in ionization densities of foreign materials that the air filled detector volumes are next to. This would lead to a breakdown in CPE and an inaccurate dose measurement. However, using kerma as a dose substitute can be justified in section 2.3.4 where the medium must have a low effective Z, meaning $K_{rad} = 0$ thus $\beta = 1$. However, before a kerma volume was ultimately used, a dose measurement was tested extensively with varying distances from adjacent volumes, different volume thicknesses and using additional code specifically designed to calculate dose. Each test proved to be too variable due to the influence from adjacent volumes, only at extreme distances (1cm+) were dose measurements in line with what was expected. These measurements were taken between the top of the breast and the compression paddle to calculate an MGD and were compared against measured data. In contrast, using a thin volume to measure kerma showed no fluctuation with distance from adjacent volumes and fell to within acceptable limits of measured data.

3.5 Average Energy, HVL and Tube Yield

As part of a cumulative additional validation process of the simulation, the average energy, HVL and tube yield was calculated and compared to other

published material to ensure the forthcoming results have every opportunity to be as accurate as possible.

For the calculation of the HVL and tube yield the first set of phase-space files were used to produce a beam through relevant filter materials and thicknesses, the HVL and tube yield calculations also had the compression paddle placed in the beam. The anode/filter combinations and energies used were Mo/Mo, Mo/Rh, Rh/Rh and W/Al, and 24-36kV in 2kV increments; the reason for these selections will be discussed in section 3.7.

To calculate the HVL and yield the filter was placed at $Z = 2.7cm$ and the compression paddle at $Z = 8cm$, the detector volume was positioned below the filter and compression paddle at $Z = 59.2cm$ which is in accordance with "Senographe Essential Service Information and Procedures Class A SIP-A" (2014). To replicate a normal HVL measurement performed on a mammography unit an additional Al filter was placed slightly above the detector volume at $Z = 57cm$ and for each anode/energy/filter combination the Al thickness was varied between $0 - 0.8mm$ in $0.2mm$ increments. A kerma measurement was taken from 10^8 simulated histories for each Al thickness.

The data was then imported into Matlab where a HVL was calculated using a formula referred to in "Senographe Essential Service Information and Procedures Class A SIP-A" (2014), but adapted more generally as:

$$\text{HVL} = \frac{t_b\ ln(2K_a/K_0) - t_a\ ln(2K_b/K_0)}{ln(K_a/K_b)} \tag{3.1}$$

where K_a and K_b are kerma values at Al thickness t_a and t_b respectively, but $t_a < t_b$ for kerma values that fall either side of the HVL.

The yield was calculated using the kerma measurement with no Al filter in the beam. The mAs was then calculated based on the 'general' mAs to produce the first set of phase-space files, which is non anode/energy specific, and adjusted that figure by the ratio of the number of simulated histories used by the phase-space file, 10^8, to the number of photons in phase-space file. Thus the general and phase-space specific mAs was calculated as:

$$\text{General mAs} = (2 \times 10^9) \cdot (1.602177 \times 10^{-19} \cdot (1000) = 3.2 \times 10^{-7}\text{mAs} \tag{3.2}$$

where 2×10^9 is the quantity of electrons used to generate the first set of phase-space files, 1.602177×10^{-19} is the amount of charge per electron in coulomb (C) or amp second (As), and 1000 adjusts As to mAs.

$$\text{Specific mAs} = \textit{Initial mAs} \cdot \left(\frac{10^8}{\textit{\# of photons in phase-space file}} \right) \tag{3.3}$$

An example of this being if say a phase-space file has 55000 photons and 10^8 histories are produced from it, this would lead to a simulated specific mAs of 5.83×10^{-4} mAs. The yield is therefore a quotient of the kerma measurement in μGy over the specific mAs.

The average spectrum energy for each energy/anode/filter combination was taken from the second set of phase space files. A Geant4 code was developed to read the phase-space file and record the energy of each photon in a text file. These files were then imported to Matlab and the mean energy calculated by summing the energies and dividing through by the number of entries in the file. Code for this can be found in Appendix F.

3.6 Filter Transmission

To collect filter transmission data a detector volume was positioned at $Z = 3cm$, and the filter volume was positioned at $Z = 2.7cm$ which allowed for the maximum filter thickness, $Al0.55mm$, to be clear of both the detector volume and location of the initial phase-space file. The filter dimensions were those described in section 3.1.1, the detector had dimensions $0.74cm \times 0.58cm \times 0.001mm$ and was located at $Y = 0.58cm$.

Kerma measurements were taken initially without a filter in the beam to measure the unfiltered kerma for all the phase-space files. The phase-space files were then passed through the filter materials: $0.02mm - 0.035mm$ for both Mo and Rh filter materials, and $0.4mm - 0.55mm$ for the Al filter, where kerma measurements were taken. In order to automate the filter material and thickness another two user defined commands were created in the $DetectorMessenger$ class. They were $/mammo/Filter/setFilterMat$and $/mammo/Filter/setFilterThickness$, where the input variables were $G4\_Mo$, $G4\_Rh$ or $G4\_Al$, and the aforementioned filter thicknesses respectively. As there were 39 phase-space files and 12 filter combinations, 468 data files were

produced. This data was then processed in Matlab where the transmission, a ratio of transmitted kerma vs incident kerma, was plotted and fitted to a cubic polynomial: $ax^3 + bx^2 + cx + d$, a, b, c and d are coefficients of the fit. An inverse square (IVS) factor was also added to the data as the detectors were at different Z coordinates.

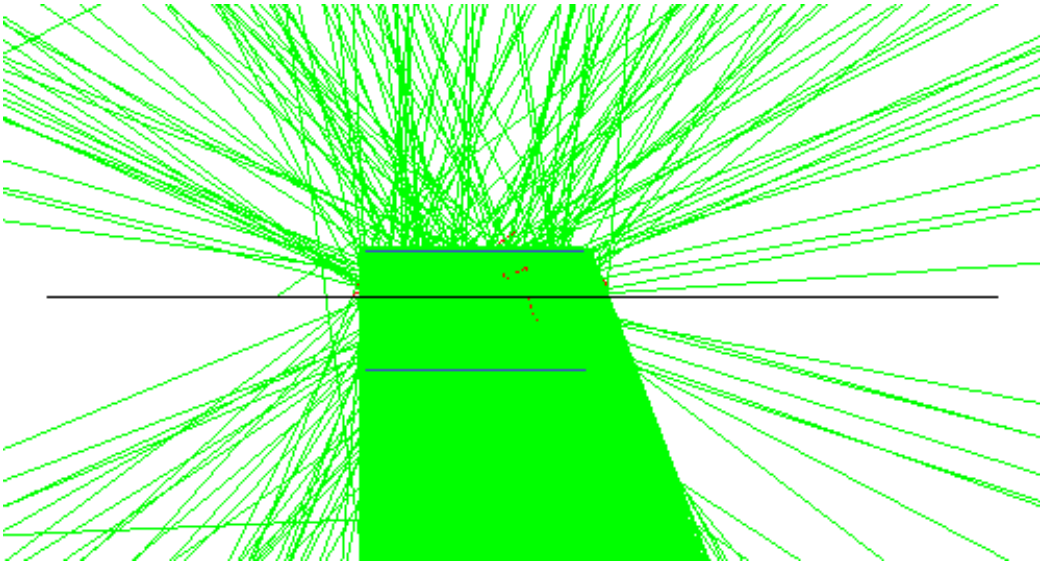

Figure 3.4: Geant4 visualisation of filter transmission, the black line represents the filter and the blue lines are the detector volumes. The green lines are photon tracks, and the red dots and lines are electron paths. Of note is the quantity of both forward and backscatter.

3.7 Breast Transmission

Breast transmission data was measured similarly to filter transmission where an incident air kerma was measured between the compression paddle and the top of the breast, and a second kerma measurement taken between the grid and CsI(Tl) scintillator. The volumes were arranged as described in section 3.1.1 and the detector volumes located as seen in Figure 3.2. The Z location of the detector volume between the compression paddle and breast, and above the compression paddle varied dependant on the breast thickness. Where as the detectors between the breast support and grid, and between the grid and scintillator were $Z = 65.75cm$ and $65.95cm$ respectively.

The second set of phase-space files, which were produced by using the first phase-space files through various filters and recorded at $Z = 55cm$, were used at this stage. As the phase-space files were specific to anode material, filter material and filter thickness, only two user specific commands were created to manage the transmission simulation runs. The first was a command to load the phase-space file, which had already been somewhat developed in the filter transmission simulations, and the second was to vary the breast thickness; $/mammo/SourceFile/setFile$ and $/mammo/Breast/setBreastThickness$ respectively. 2×10^9 histories were simulated from the phase-space files, so the macro file therefore looked similar to:

$/mammo/SourceFile/setFile\ Mo\_Anode/Mo0.02mmFilter/Mo24\_Mo0.02mm$
$/mammo/Breast/setBreastThickness\ 40\ mm$
$/run/beamOn\ 2000000000$

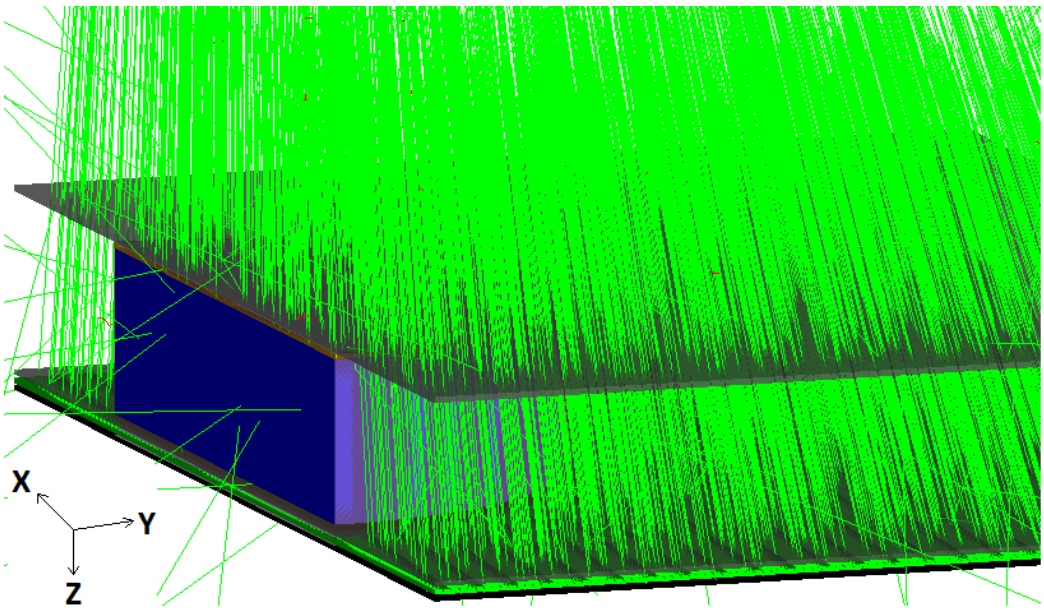

Figure 3.5: 3D Geant4 visualisation of breast transmission simulation with a breast thickness of 4cm; the green lines represent photon tracks

From the 468 phase-space files produced from the filter transmission and the 7 different breast thicknesses, 3276 data sets and additional phase-space files would be produced from this phase of the simulation. This was subsequently reduced to energies between 24 and 36kV but in 2kV increments,

anode/filter combinations Mo/Mo, Mo/Rh, Rh/Rh and W/Al, and breast thicknesses $2-8$cm in 2cm increments leading to 448 data sets and additional phase-space files (this will be discussed in Chapter 5).

The data was then imported into Matlab and processed to produce transmission curves similar to that produced with the filter transmission. The breast transmission was fitted to a double exponential, $a*exp(bx)+c*exp(dx)$, a, b, c and d are coefficients of the fit; an IVS correction was also applied. In order to produce a transmission curve from which to obtain a fitted function for a specific set of parameters, the transmission (ratio of transmitted kerma to entrance kerma) was plotted as a function of breast thickness.

Additionally a set of breast transmission data was collected with the aforementioned parameters, but using PMMA as the breast material. This was done in aid of establishing a model for a water equivalent thickness where the ratio of the transmission between water and PMMA could be calculated. As a breast thickness can be linked to a glandularity, and a PMMA thickness to an equivalent breast thickness (Dance et al., 2000), a model of a water equivalent thickness could be calculated.

3.8 Simulation Validation and Water Equivalent Thickness

To validate the data taken from the breast transmission simulation, measurements were taken on a GE Essential unit. The parameters replicated on the unit from the simulation were:

- Accelerating potential of $26-34$kV in 4kV increment.
- Anode materials Mo and Rh.
- Filter materials Mo and Rh for an Mo anode, and Rh for an Rh anode
- Filter thickness of 0.025mm for an Mo filter and 0.03mm for an Rh filter.
- PMMA thickness of $2-8$cm in 2cm increments.
- Detector positioned 6cm from chest wall on the center line of the detector.

A Piranha mammography specific dosimeter was used for both entrance kerma and transmission kerma measurements, and has a dose inaccuracy of

±5% (Electronics, 2013). The Ocean 2014 diagnostic software package was used in conjunction with the dosimeter, which provides all the quality assurance features needed to obtain dose measurements and other mammography testing measurements.

Figure 3.6: Image of the validation set-up on a GE Senograph Essential. Shown is the dosimeter, red rectangular device, between the compression paddle and two slabs of PMMA blocks each 19mm thick. The Cu plate is also shown which was used to protect the detector. Additional pictures of the procedure can be seen in Appendix G.

Kerma measurements were to be taken as described in the simulation, an entrance kerma was measured above the PMMA breast but below the compression paddle, and the other between the grid and CsI(Tl) scintillator. However due to the design of the unit a measurement between the grid and scintillator could not be achieved, in lieu of this measurement the detector was placed directly below the PMMA, i.e. between the breast support and the PMMA breast. This meant there was a slight perturbation in the geometry,

and there was now no added attenuation from the breast support. In addition to a change in the location of the detector, a 2mm Copper (Cu) plate was placed over the detector to prevent damage from excessive exposures.

As data for this location wasn't collected in the simulation, a last set of breast transmission data was collected for both PMMA and water with the breast support removed.

In order to calculate a water equivalent thickness from this data, as mentioned a double exponential was fitted to the water transmission data, but also a set of PMMA transmission data. A transmission was therefore calculated for a given PMMA thickness from it's fitted function, which is dependant on the set of beam parameters. The PMMA transmission was therefore set to the water's transmission and it's fitted function was solved to render an equivalent thickness.

Additionally, data from Dance et al. (2000) was obtained and from their PMMA thickness an equivalent breast thickness was calculated, and an associated breast glandularity. Thus the calculated water equivalent thickness was associated with a breast glandularity or density.

3.9 Statistics, Uncertainty and Error

The majority of data collected is from a spectrum and therefore constitutes Poisson statistics. The standard deviation of a Poisson distribution, σ, can be represented as $\sigma = \sqrt{N}$ and the variance, σ^2, can be expressed as $\sigma^2 = N$.

To represent the variation of a quantity a RMSE will be calculated, which is the square root of the mean squared error (MSE) where the MSE is the square of the distance between, for example, a fitted line and a data point. The RMSE therefore gives the distance, on average, between the fitted line to the data and this is what will be used as a measure of the goodness of fit where fitted functions are used. By extension this can also be used to calculate the observed variation in a dose measurement. To express the RMSE more formally:

$$RMSE = \sqrt{\frac{1}{n}\sum_{i=1}^{n}((y_i - \hat{y}_i)^2)} \tag{3.4}$$

where y_i is the measured data value and $\hat{y}_i$ is the predicted value.

As the filter and breast transmission will include two separate measurements with their associated errors, attenuated and unattenuated, where a ratio of the two will be calculated, errors will be handled with the following:

$$\sigma R = |R| \cdot \sqrt{\left(\frac{\sigma X}{X}\right)^2 + \left(\frac{\sigma Y}{Y}\right)^2} \tag{3.5}$$

where σR are the relative error, σX and σY is the uncertainties in the two respective measurements X and Y, and $|R|$ is the final result $R = X/Y$.

Additionally, a coefficient of determination (R^2) value will be associated with each fit that is calculated. To calculate an R^2 the method of least-squares is used to generate parameters for the fitted function that minimises the sum of the squared residuals, which accounts for the variability in the data by the statistical model. Generally the closer R^2 is to 1, the better the fitted function explains the data:

$$R^2 = \frac{SS_R}{SS_T} = \frac{\sum_i (\hat{y}_i - \bar{y})^2}{\sum_i (y_i - \hat{y}_i)^2} \tag{3.6}$$

where y_i and $\hat{y}_i$ are the data and modelled values respectively, SS_R and SS_T are the residual sum of squares and total sum of squares respectively.

However, although R^2 is a good indicator of the goodness of fit it doesn't indicate biasing, in this case a visual inspection of the residuals plot is required. This observation is critically important to the accuracy of kerma measurements throughout this project as they are based on a the mass-absorption attenuation coefficient which is determined by fitting National Institute of Standards and Technology (NIST) data to a function that can be used in Geant4.

Other sources of uncertainty and error are present as part of the simulation and it's relationship to the validation measurements. Such uncertainties include the accuracy of geometric locations and orientations, a disparity in the density and thickness of geometric volumes (compression paddle, filter and breast volume), the accuracy of test equipment, and the impact of scatter. An attempt will be made to minimise said error production, but where it is not possible to eliminate uncertaintly, appropriate steps will be made to account for any error in the results.

Chapter IV

Results

4.1 Initial Spectrum Validation

A comparison with SpekCalc spectra, 40kV and 150kV, revealed a very poor fit with the lower energy of 40kV but an excellent fit with 150kV; the reason for this will be discussed in Chapter 5. The simulated spectra and SpekCalc spectra were compared through observing the location of characteristic peaks and their intensity, and the intensity of bremsstrahlung throughout the spectra. More formally the respective data was fitted to a linear correlation model, $x = y$, and a linear regression model; an R^2 and root mean squared error (RMSE) was obtained as a measure of correlation for both.

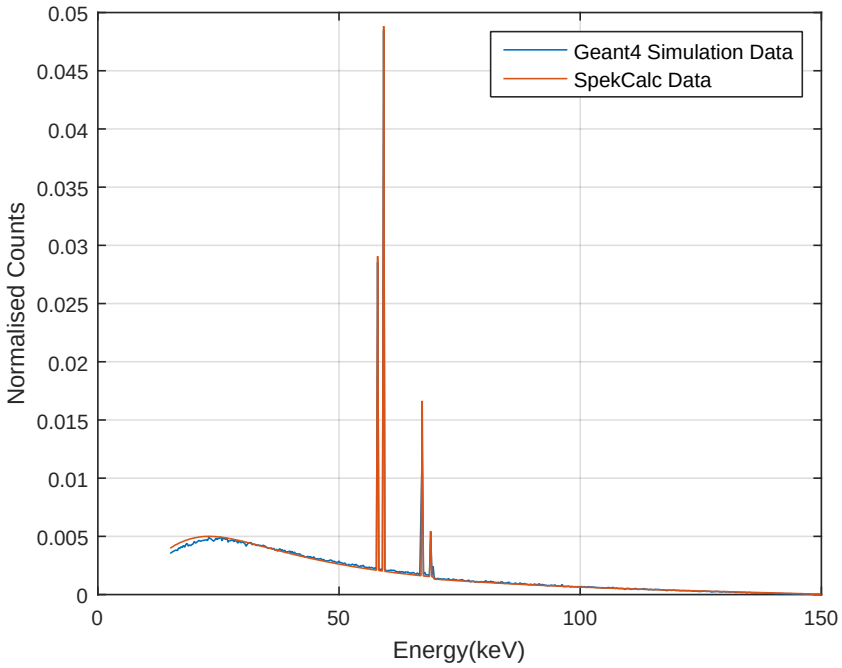

Figure 4.1: W 150kV Geant4 and SpekCalc spectra.

The 150kV Geant4 and SpekCalc spectra results can be shown in Figure 4.1, and the linear models in Figure 4.2 where R^2 and the $RMSE$ for both are annotated. The data was binned into 0.25keV bin widths to give adequate spectral resolution to observe the peaks accurately; the data was normalised as $1/N$ where N is the integral of the curve, or total counts. A table of K-edge characteristic x-ray line energies has been provided to allow the reader to compare the spectrum with known data from (Bearden, 1967; Dewey, Mapes, & Reynolds, 1969; Salem, Panossian, & Krause, 1974). The intensities are intended as a very rough guide to the measured spectrum's accuracy; numerically presented as relative to the highest peak intensity.

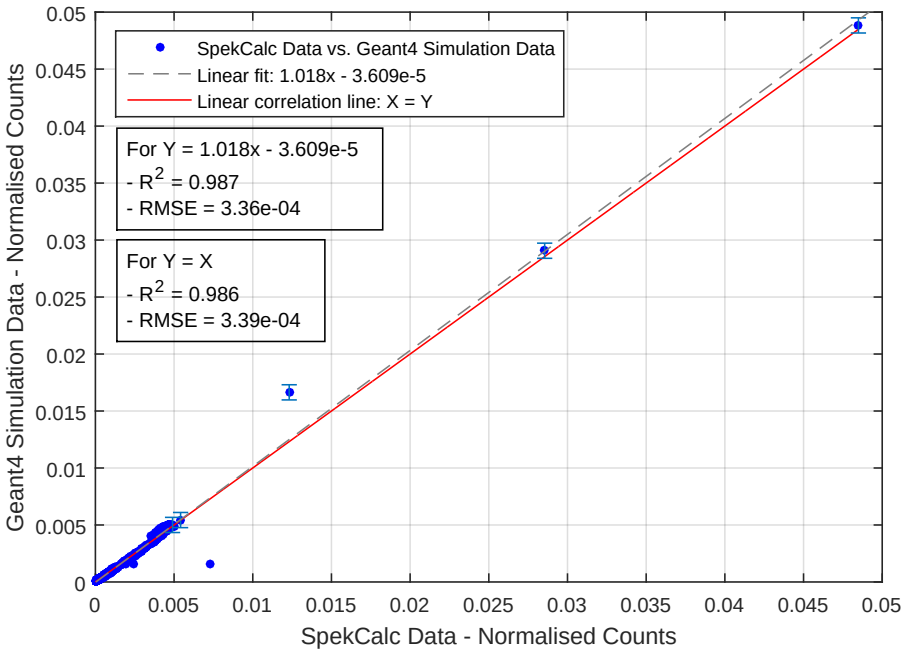

Figure 4.2: W 150kV Geant4 and SpekCalc linear comparison.

Table 4.1: K-series characteristic X-ray line energies for W (keV).

Reference Peak Location(keV)	*69.10*	*67.24*	*66.95*	*59.32*	*57.98*
Reference Intensity(%)	~ 11	~ 20	~ 10	100	~ 59
Geant4 Peak Location(keV)	*69*	*67.25*	*67*	*59.25*	*58*
Geant4 Intensity(%)	11.1	24.3	13.1	100	58.9
SpekCalc Intensity(%)	11.1	34.1	*N/A*	100	59.5

It can be observed that both characteristic peak locations and intensities match well with SpekCalc data and reference data from Table 4.1, however intensities at peaks 67.25keV and 67keV don't match particularly well with a differences of 12.5% and 21.5% respectively. An explanation for this will be given in Chapter 5. The 67.25keV and 67keV peak intensities are also difficult to confirm from SpekCalc data as they are not well represented individually and in fact share the same peak. This, in part, is due to the level of accuracy in the simulation peak locations, which is a function of the histogram's bin widths the spectrum was rendered from - ±0.125keV; this will be discussed further in Chapter 5. Notwithstanding the notable outliers the maximum difference in spectral peak intensity is ±1.1%.

The spectra comparison between SpekCalc and Geant4 for a W anode at 40kV can be seen in Figure 4.3, and it's linear correlation and regression fit in Figure 4.4. This data was again binned into 0.25keV bins and normalised the same way as the W 150kV spectra. A table of L-edge characteristic x-ray line energies has been added to compare the Geant4 result vs reference data from Bearden (1967); Dewey et al. (1969); Salem et al. (1974).

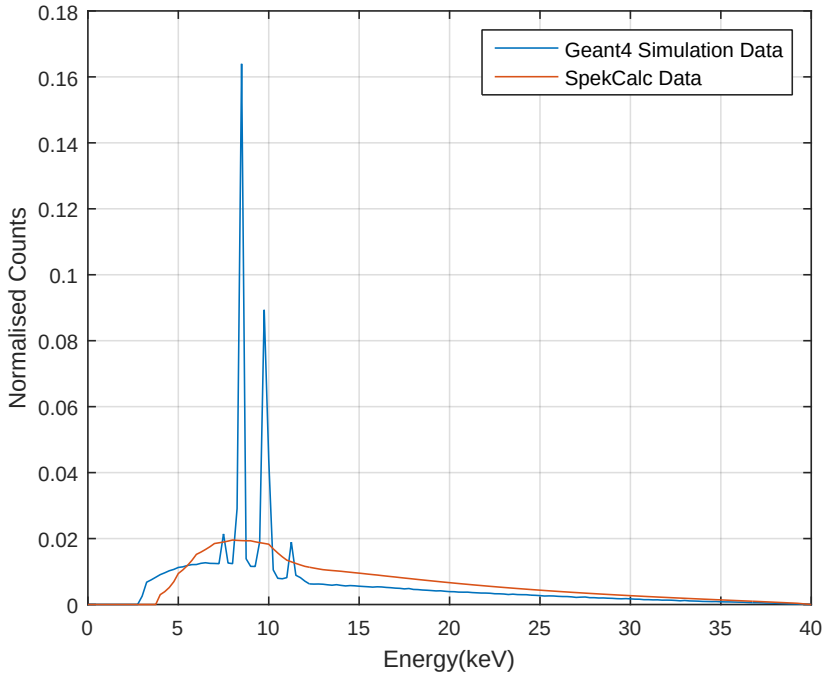

Figure 4.3: W40kV SpekCalc spectra

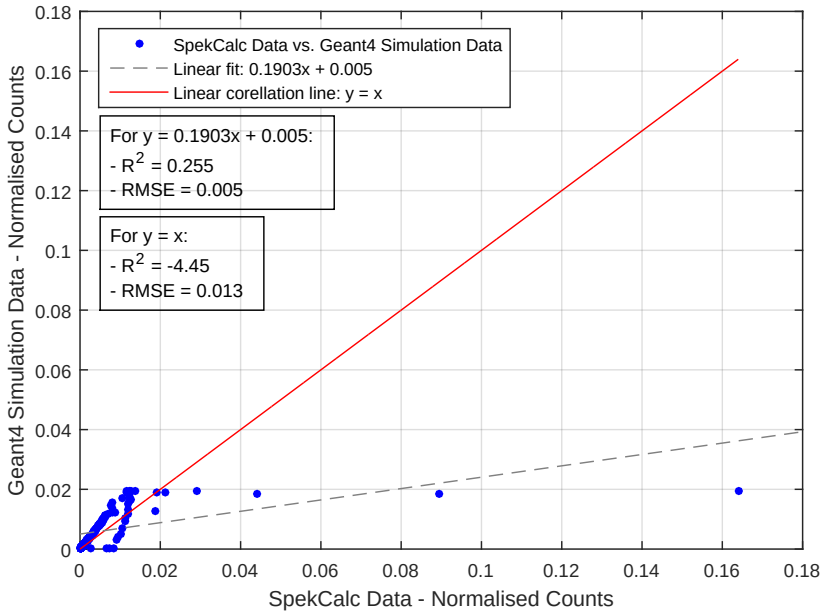

Figure 4.4: W40kV SpekCalc linear fit.

Table 4.2: L-series characteristic X-ray line energies for W (keV).

	L1-series			**L2-series**	
Refeence Peak Location(keV)	*11.68*	*9.82*	*9.53*	*11.28*	*9.67*
Reference Intensity(%)	22	100	71	19	100
Geant4 Intensity(%)	22	100	77	17	100

	L3-series			
Reference Peak Location(keV)	*9.96*	*8.40*	*8.36*	*7.39*
Reference Intensity(%)	23	100	11	4
Geant4 Intensity(%)	20	100	11	6

However, table 4.2 differs slightly from the table presented with a W anode at 150kV. As the SpekCalc data renders no characteristic peaks the Geant4 simulated spectrum can't be correlated against it; Table 4.2 is compared purely to the aforementioned reference data. To do this the Geant4 spectrum was binned into much smaller bins, 0.01keV, to gain an acceptable energy resolution. It was found the peaks occurred precisely where the reference data states, and considering the reference intensities are supposed to

act purely as a rough guide, the intensities are within an acceptable margin.

As mentioned SpekCalc data offers no visible peaks on which to correlate and compare Geant4's data, the results of any associated analyses is inconsequential. So as an applicable substitute data from IPEM78 was used to produce a spectrum to analyse against Geant4 data, the spectra can be found in Figure 4.5, and linear correlation and regression fit in Figure 4.6.

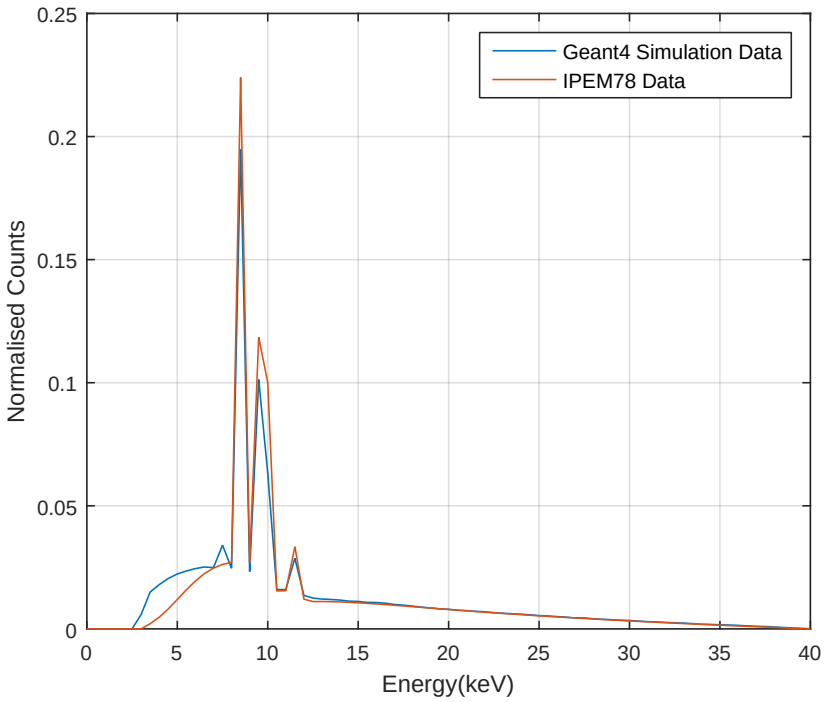

Figure 4.5: W40kV IPEM78 spectra

The data available from IPEM78 has a set energy resolution of 0.5keV, thus the Geant4 data had to match that resolution in order to obtain a spectrum from which any analysis could be done. As such the peaks represented in Table 4.2 are not visible, only the major peak locations can be ascertained from the spectra and Figure 4.5, therefore, acts as a visual guide to Geant4's validity. Figure 4.6 shows R^2 and RMSE of the respective linear fits for IPEM78 versus Geant4 data. Discussion on the accuracy of this comparison, as well as the comparison presented with the W anode at 150keV, will be presented in Chapter 5.

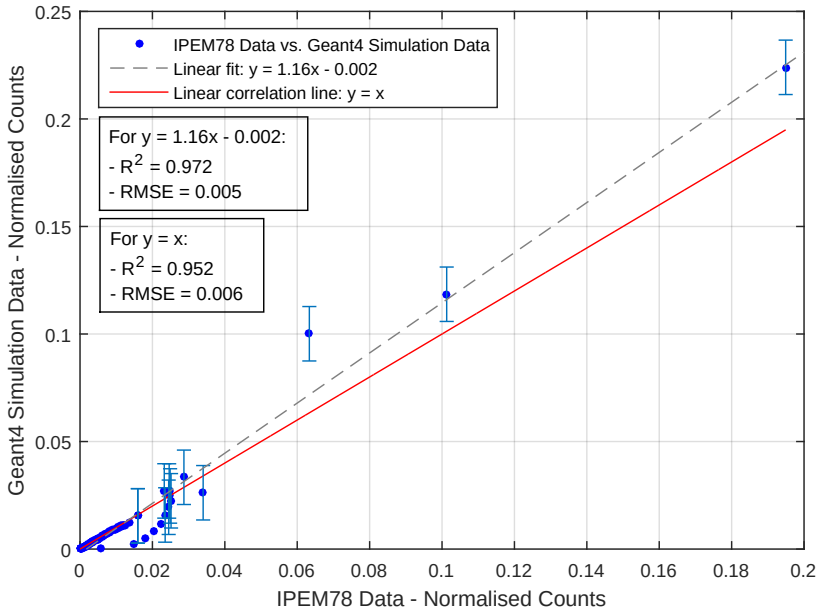

Figure 4.6: W40kV IPEM78 linear fit.

4.2 Filter Transmission

The filter transmission plots are shown in Figures 4.7 and 4.8. Typically a transmission plot is made such that it extends back to a transmission of 1 where there is no filter in the beam, however in this instance the transmission was fitted only over the relevant ranges. When attempting to produce a suitable fit to an appropriate function with the addition of no filter in the data, fitting the function was troublesome and the results proved to be too inaccurate. The best results for those fits can be viewed in Appendix B.

The fitted cubic polynomials each had an $R^2 = 1$ with no calculable RMSE, i.e. RMSE ≈ 0. The error bars were calculated from the RMSE produced in the simulation, the overall mean uncertainty was $\pm 2.3\%$ with a minimum uncertainty of $\pm 0.4\%$ and a maximum uncertainty of $\pm 8.6\%$. The minimum and maximum was found to occur in the Mo/Mo anode/filter plot at 34kVp and 0.02mm filter, and the Rh/Rh anode/filter plot at 26kVp and 0.035mm filter, respectively.

As well as the plots shown in Figures 4.7 and 4.8, the coefficients for the cubic polynomials have been recorded and can be viewed in Table 4.3.

The anode/filter combinations recorded here are pertinent to the subsequent breast transmission results, thus unrelated anode/filter combinations have been omitted. The calculated uncertainties will also impact the validity of the breast transmission results.

Table 4.3: Filter transmission fitted function coefficients for a cubic polynomial: ax^3+bx^2+cx+d. These coefficients are valid over the range $0.02-0.035$ for Mo and Rh filters, and $0.4-0.55mm$ for Al filters.

		Coefficients			
Anode/Filter	**Energy(keV)**	**a**	**b**	**c**	**d**
Mo/Mo	*24*	-2201	242.6	-9.911	0.1676
	26	-2209	250.1	-10.54	0.1864
	28	-2400	269.7	-11.38	0.2056
	30	-2439	277.7	-11.94	0.2226
	32	-2490	285.3	-12.44	0.2389
	34	-2447	287.3	-12.88	0.2565
	36	-3443	372.7	-15.42	0.2893
Mo/Rh	*24*	-1561	171.9	-6.941	0.1129
	26	-1612	181.4	-7.540	0.1289
	28	-1850	206.1	-8.538	0.1474
	30	-1794	205.1	-8.798	0.1596
	32	-2225	244.5	-10.14	0.1811
	34	-2338	258.9	-10.89	0.1990
	36	-2267	256.4	-11.08	0.2100
Rh/Rh	*24*	-1045	114.9	-4.611	0.0737
	26	-1069	119.5	-4.900	0.0813
	28	-1101	123.4	-5.126	0.0879
	30	-840.8	103.0	-4.727	0.0906
	32	-802.5	101.1	-4.790	0.0960
	34	190.3	15.54	-2.458	0.0792
	36	-67.20	39.64	-3.302	0.0934

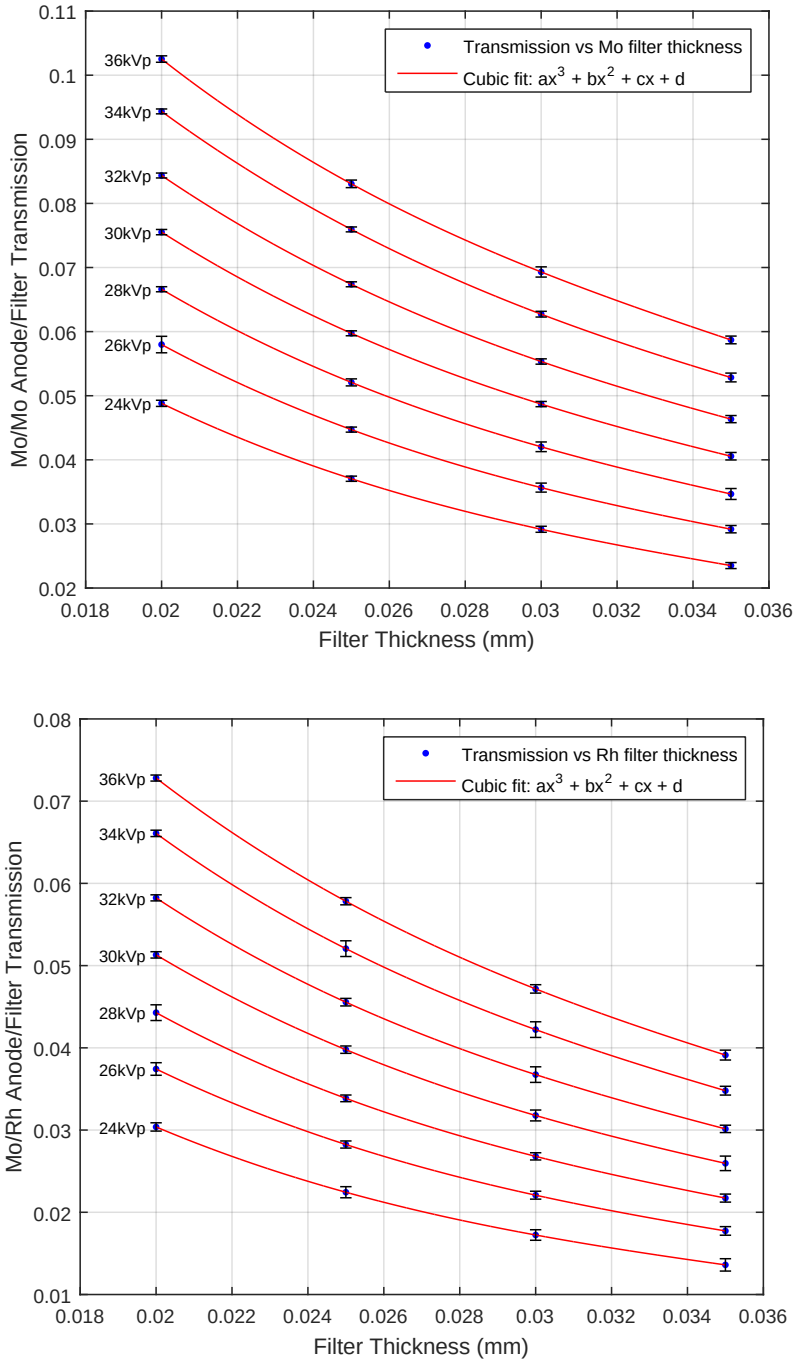

Figure 4.7: Filter transmission curves for (top) Mo/Mo anode/filter combinations, and (bottom) Mo/Rh anode/filter combinations.

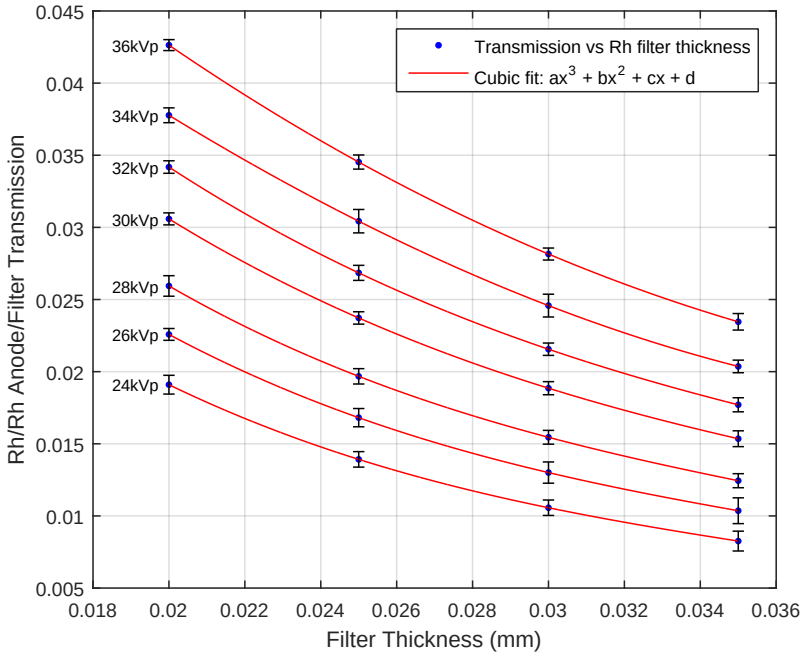

Figure 4.8: Filter transmission curves for (top) Rh/Rh anode/filter combinations.

4.3 HVL, Mean Energy, and Tube Yield

The results for the measured HVL, mean energy and tube yield are presented in the following tables. These values function as important validation of filtered spectra, in particular the yield values as an evaluation can be inferred as to the accuracy of dose measurements from the simulation in reference to validation measurements from the mammography unit.

The HVL and mean energy values were compared to Boone et al. (1997), the yield measurements were compared to data collected from a GE Essential when taking breast transmission measurements. The anode/filter combinations presented here are the combinations able to be validated on a GE Essential, for a more extensive list of simulation HVLs, mean energies and yields, see Appendix C

HVL values in Table 4.4 were calculated with individual errors, but had an overall mean error of ±3.5% with a minimum of ±1.6% and maximum of ±9.8%. Comparing data to Boone et al. (1997), a mean divergence of ±2.3%

with a minimum and maximum of ±0.1% and ±5.6% respectively.

Table 4.4: HVL simulation measurements compared against Boone et al. (1997).

Mo Anode		**24**	**26**	**28**	**30**	**32**	**34**	**36**
Filter	**Thickness**	**HVL(mmAl)**						
Mo	0.03	0.302	0.328	0.346	0.365	0.380	0.394	0.409
Boone et al. (1997)		*0.305*	*0.325*	*0.351*	*0.365*	*0.386*	*0.401*	*0.413*
Rh	0.025	0.353	0.386	0.405	0.423	0.439	0.449	0.466
Boone et al. (1997)		*0.352*	*0.380*	*0.408*	*0.422*	*0.441*	*0.454*	*0.464*
Rh Anode								
Rh	0.025	0.332	0.370	0.401	0.430	0.453	0.477	0.497
Boone et al. (1997)		*0.337*	*0.371*	*0.412*	*0.443*	*0.471*	*0.489*	*0.517*

Table 4.5: Mean energies for simulation measurements compared against Boone et al. (1997).

Mo Anode		**24**	**26**	**28**	**30**	**32**	**34**	**36**
Filter	**Thickness**	**Mean energy(keV)**						
Mo	0.03	15.59	16.04	16.41	16.79	17.13	17.48	17.83
Boone et al. (1997)		*16.27*	*16.65*	*17.06*	*17.39*	*17.80*	*18.19*	*18.61*
Rh	0.025	16.53	17.00	17.36	17.69	17.96	18.26	18.56
Boone et al. (1997)		*17.14*	*17.57*	*17.93*	*18.17*	*18.48*	*18.74*	*19.09*
Rh Anode								
Rh	0.025	16.38	17.12	17.74	18.21	18.67	19.09	19.45
Boone et al. (1997)		*17.18*	*17.91*	*18.50*	*18.99*	*19.41*	*19.76*	*20.12*

As with HVL values the average energies were calculated with individual errors, however a mean error of ±2.4% and minimum and maximum of ±0.6% and ±8.7% was calculated respectively. When comparing the values to Boone et al. (1997) a mean difference of ±4.0% with a minimum and maximum of ±1.7% and ±6.7% was calculated respectively.

Table 4.6: Yields for Mo and Rh anodes. 0.03mm Mo and 0.025 Rh filters for the Mo anode, and 0.025 Rh filter for the Rh anode 24 - 36kVp.

Mo Anode		**24**	**26**	**28**	**30**	**32**	**34**	**36**
Filter	**Thickness**				**Yield(μGy/mAs)**			
Mo	0.03	74.2	97.7	119.7	145.1	172.0	198.0	228.7
GE Essential		*58.1*	*80.2*	*105.5*	*133.2*	*164.1*		
Rh	0.025	61.4	83.1	103.8	126.8	150.7	174.6	203.1
GE Essential		*50.3*	*71.1*	*94.5*	*119.6*	*147.5*	*176.5*	*208.5*
Rh Anode								
Rh	0.025	58.7	75.3	94.3	115.9	134.7	156.8	180.4
GE Essential			*63.4*	*84.2*	*108.2*	*133.9*	*162.5*	*192.4*

The yield values in Table 4.6 serve as an important indicator and addition to the HVLs and mean energies in Table 4.4 and 4.5. These values have a mean calculated error of ±5.2% with a minimum and maximum of ±4.1% and ±6.8% respectively. The mean difference between measured and simulated values was 11.7%, with a minimum and maximum of 1.1% and 22.7% respectively; the uncertainty in these measurements was ±5.1%. However, when assessing in terms of a GE Essential three testing parameters sets are important as stated in "Senographe Essential Service Information and Procedures Class A SIP-A" (2014), they are an Mo anode at 26keV with an Mo filter 0.03mm thick, an Mo anode at 28keV with an Rh filter 0.025mm thick, and finally an Rh anode at 30keV with an Rh filter 0.025mm thick.

The limits for the mentioned three parameter sets are a HVL of $0.29 - 0.38$mmAl, $0.31 - 0.47$mmAl and $0.33 - 0.52$mmAl respectively, and yield values of $35 - 130\mu$Gy/mAs for each. The three parameter sets can be observed to fall within these limits stipulated by GE. The ACPSEM suggests guidelines of a minimum of $(kV/100) + 0.03$mmAl and a maximum of $(kV/100) + C$mmAl where C= 0.12 for Mo/Mo anode/filter, C= 0.19 for Mo/Rh anode/filter, and C= 0.22 for Rh/Rh anode/filter (Heggie et al., 2012). Again, the parameters sets fall within these suggested limits.

4.4 Breast Transmission and Water Equivalent Thickness

Results for breast transmission can be found in Table 4.7, 4.8 and 4.9. Instead of presenting all of the transmission figures, due to the shear number of values only the fitted function's coefficients that are relevant to the subsequent simulation validation are listed; a more extensive list can be found in Appendix D. Each function had an $R^2 = 1$ with no calculable RMSE.

Table 4.7: Mo/Mo anode/filter transmission fitted function coefficients for a water breast: $a * exp(bx) + c * exp(dx)$

Mo Anode	**Energy**	**Coefficients**			
Mo Filter	**(keV)**	**a**	**b**	**c**	**d**
0.03mm	*24*	0.2349	-0.1250	0.0451	-0.0783
	26	0.2710	-0.1135	0.0231	-0.0640
	28	0.2926	-0.1153	0.0335	-0.0609
	30	0.3020	-0.1076	0.0205	-0.0503
	32	0.3219	-0.1098	0.0281	-0.0478
	34	0.3215	-0.1066	0.0270	-0.0437
	36	0.3364	-0.1077	0.0331	-0.0428

Table 4.8: Mo/Rh anode/filter transmission fitted function coefficients for a water breast: $a * exp(bx) + c * exp(dx)$

Mo Anode	**Energy**	**Coefficients**			
Rh Filter	**(keV)**	**a**	**b**	**c**	**d**
0.025mm	*24*	0.2266	-0.1244	0.0775	-0.0710
	26	0.2236	-0.1199	0.1112	-0.0677
	28	0.4289	-0.1558	0.1440	-0.0660
	30	0.2445	-0.1092	0.1192	-0.0609
	32	0.2800	-0.0971	0.0904	-0.0553
	34	0.3181	-0.0904	0.0667	-0.0487
	36	0.3320	-0.0876	0.0581	-0.0447

Table 4.9: Rh/Rh anode/filter transmission fitted function coefficients for a water breast: $a * exp(bx) + c * exp(dx)$

Rh Anode Rh Filter	**Energy (keV)**	**Coefficients a**	**b**	**c**	**d**
0.025mm	*24*	0.2266	-0.1244	0.0775	-0.0710
	26	0.2236	-0.1199	0.1112	-0.0677
	28	0.2453	-0.1063	0.0973	-0.0619
	30	0.2855	-0.1177	0.1292	-0.0617
	32	0.2800	-0.0971	0.0904	-0.0553
	34	0.3181	-0.0904	0.0667	-0.0487
	36	0.3320	-0.0876	0.0581	-0.0447

The calculated uncertainty stems from a range of factors, the first being the anode/filter transmission uncertainty calculated previously, the second was a small factor, 1%, added due to the conversion between kerma and dose in the simulation not being perfect, this will be discussed in Chapter 5. An example of a breast transmission graph can be seen in Figure 2.6, additional example graphs can be seen in Appendix D.

In order to calculate a water equivalent thickness, a set of breast transmissions from PMMA breast thicknesses had to be collected. The purpose of this was to link a PMMA transmission to a water transmission where the PMMA transmission could be linked to an equivalent breast thickness and hence a glandularity from Dance et al. (2000). The relevant coefficients for the PMMA breast transmission can be found in Appendix D.

Figure 4.9 shows an example of the difference in water and PMMA transmission curves. In this particular case for 26kV Rh/Rh 0.025mm anode/filter combination, the transmission curve coefficients for PMMA are: $a = 0.6114$, $b = -0.0853$, $c = 0.1062$, and $d = -0.0421$; and for water: $a = 0.4019$, $b = -0.0900$, $c = 0.0420$, and $d = -0.0437$. Taking a breast thickness of 45mm, for example, and using the double exponential fit, a PMMA transmission is calculated to be 0.0291 ± 0.0012. Now solving the double exponential fit for water with the same transmission of 0.0291 ± 0.0012, an equivalent

thickness is calculated to be $33.63mm \pm 1.44mm$.

Using Dance et al. (2000) data, an equivalent breast thickness can be calculated as $55.56mm \pm 2.78mm$ with a glandularity depending on age of $45.41\% \pm 2.01\%$ if aged $40 - 49$ years, and $29.53\% \pm 1.48\%$ of aged $50 - 64$ years. The uncertainty in these measurements corresponds to a maximum reported error not exceeding 5% in Dance et al. (2000).

Plots for the data extracted from Dance et al. (2000) can be found in Appendix E.

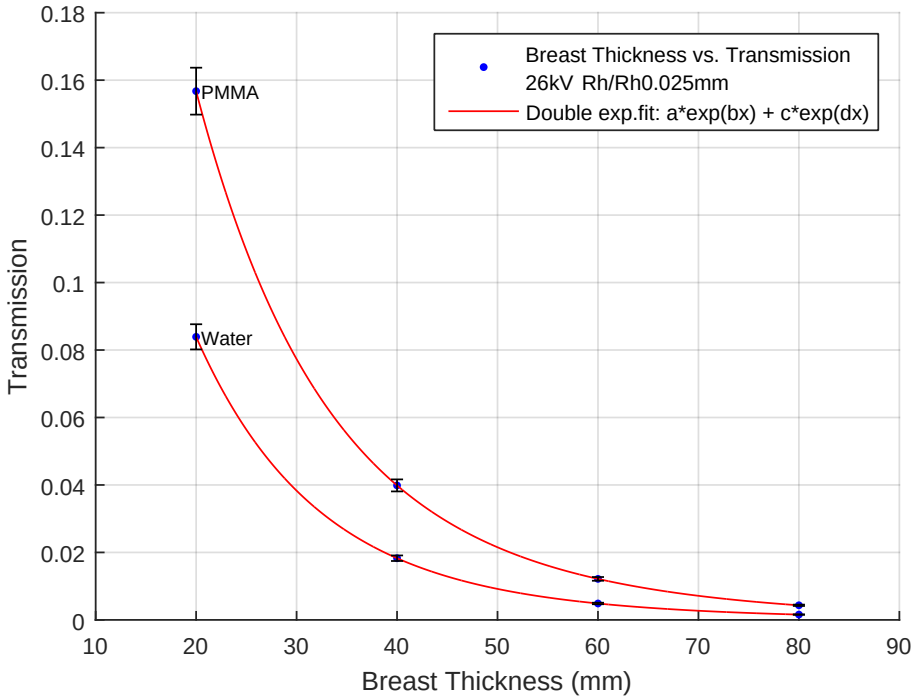

Figure 4.9: Water and PMMA transmission curves at 26kV with a Rh/Rh 0.025mm anode/filter combination.

4.5 Simulation Validation

The following tables of measurements were taken as per Section 3.8. Table 4.10 shows the entrance kerma measured from between the compression paddle and PMMA block. The GE Essential has some inherent limits on what energies can be used with specific anodes, so where there are no values for an energy is where a limit exists for the particular anode. Additionally, where values begin to occur at 4kV intervals is where it was decided to limit the amount of exposures the machine was making in order to prevent any undue stress on the older machine; the machine was manufactured in 2004.

Each kerma measurement, be it entrance or transmission, was produced with a constant mAs so as to aid in tube yield calculations. The tube was also set to use the large focal spot of 0.3mm, as opposed to the smaller focal spot of 0.1mm used for magnification techniques. The kV settings were entered manually into the machine.

Table 4.10: Entrance kerma measurements taken from a GE Essential.

Anode/	**Breast**	**24**	**26**	**28**	**30**	**32**	**34**	**36**
Filter	**Thickness**	**Dose(mGy)**						
Mo/Mo	19mm	1.269	1.755	2.307	2.919	3.592		
0.03mm	38mm	1.358	1.880	2.468	3.122	3.838		
	57mm	1.452	2.009	2.641	3.340	4.107		
	76mm	1.561		2.832		4.400		
Mo/Rh	19mm	1.097	1.559	2.066	2.623	3.23	3.874	4.569
0.025mm	38mm	1.175	1.668	2.210	2.808	3.452	4.143	4.880
	57mm	1.259	1.779	2.357	2.987	3.676	4.406	5.197
	76mm	1.353		2.543		3.963		5.600
Rh/Rh	19mm		1.386	1.849	2.37	2.941	3.562	4.229
0.025mm	38mm		1.479	1.974	2.532	3.141	3.803	4.512
	57mm		1.581	2.106	2.700	3.345	4.048	4.802
	76mm		1.706		2.908		4.365	

The figures presented in Table 4.10 were also used to calculate tube yield, which were compared to simulation yield calculations in Section 4.3 as an

important validation measurement.

Table 4.11 show the transmission kerma measured between the PMMA block and the breast support. These measurements followed on from the entrance measurements where the kV interval moved to 4kV, again this was in aid of protecting the machine from undue stress from the quantity of measurements.

As mentioned in Section 3.8, each measurement has a 5% uncertainty from the accuracy of the dosimeter, however other uncertainties will be added from geometric inaccuracies inherent with any mammography machine.

Table 4.11: Transmission kerma measurements taken from a GE Essential.

Anode/ Filter	**Breast Thickness**	**24**	**28**	**32**	**36**
		Dose(mGy)			
Mo/Mo	19mm	0.1895	0.4035	0.6953	
0.03mm	38mm	0.03946	0.09666	0.1843	
	57mm	0.009937	0.02704	0.05934	
	76mm	0.002766	0.008814	0.0225	
Mo/Rh	19mm	0.1962	0.4913	0.7015	1.044
0.025mm	38mm	0.04864	0.1124	0.1997	0.3148
	57mm	0.01392	0.03435	0.06625	0.1134
	76mm	0.004334	0.0117	0.02497	0.04697
		26	**30**	**34**	
Rh/Rh	19mm	0.2795	0.5594	0.9222	
0.025mm	38mm	0.07914	0.1751	0.3091	
	57mm	0.02529	0.06087	0.115	
	76mm	0.008697	0.02272	0.04623	

Table 4.12 show the final transmission ratio between the transmission kerma and entrance kerma. Propagating errors from both entrance and transmission inaccuracies, one can calculate an uncertainty of ±5.1%. Additionally it was discovered that the PMMA blocks were in fact 19mm thick, which means the transmission ratios will be fitted at 19mm intervals.

Table 4.12: Transmission ratio taken from GE Essential.

Anode/ Filter	**Breast Thickness**	**24**	**28**	**32**	**36**
		Dose(mGy)			
Mo/Mo	19mm	0.1493	0.1749	0.1936	
0.03mm	38mm	0.02906	0.03917	0.04802	
	57mm	0.006843	0.01024	0.01445	
	76mm	0.001772	0.003112	0.005118	
Mo/Rh	19mm	0.1789	0.2378	0.2172	0.2285
0.025mm	38mm	0.04139	0.0509	0.05785	0.06451
	57mm	0.01106	0.01457	0.01802	0.02182
	76mm	0.00320	0.00460	0.006301	0.008388
		26	**30**	**34**	
Rh/Rh	19mm	0.2017	0.2360	0.2589	
0.025mm	38mm	0.05351	0.06915	0.08128	
	57mm	0.01599	0.02254	0.02841	
	76mm	0.005099	0.007813	0.01059	

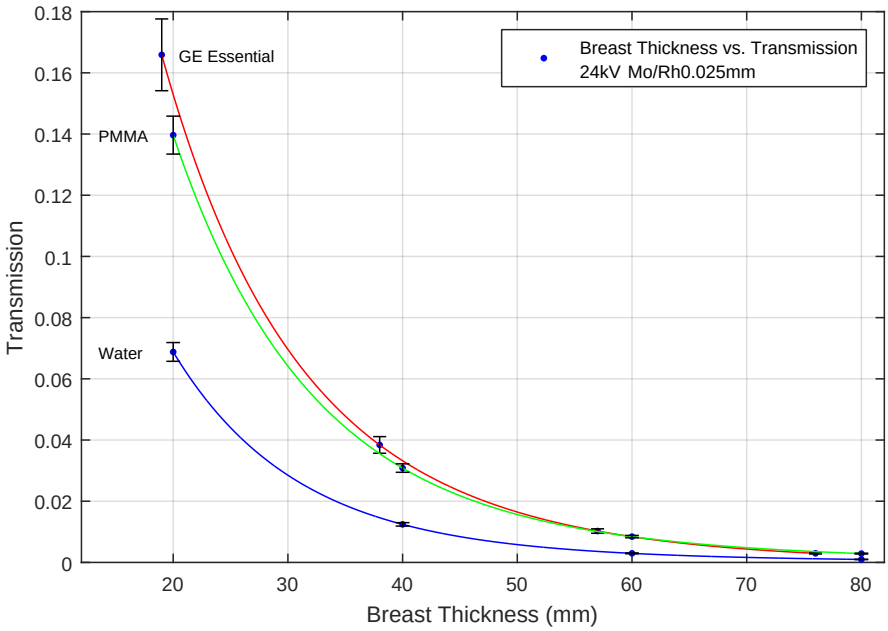

Figure 4.10: Transmission data for Geant4 water and PMMA simulation versus GE Essential: 24kV Mo/Rh 0.025mm anode/filter combination.

Chapter V

Discussion

5.1 X-ray Tube Build

Geant4 documentation provided a number of basic and advance examples for new users to run in order to become familiar with how the tool-kit operates, and how it behaves when parameters are adjusted. This is purely up to the users preference on how they interact with, and manipulate the code in order to learn; this is particularly important for a user with little or no programming experience. This also meant the user was able to start with a working, error free model from which to base their work.

It quickly became apparent that, in using the basic example B1 for the base from which to start the design of this project, was the best initial approach as it was simplistic enough for a layman to manipulate and alter without too many confusing, or time-consuming errors to solve. With only two physical volumes, an electron gun and a dose measurement method already instilled in the example, it took little manipulation to set up an initial x-ray tube. One of the physical volumes was changed to a cylinder and repositioned to an appropriate position, and the electron gun was made smaller in size, repositioned and redirected to replicate electrons incident on an anode with a specific focal spot size. This proved a little more difficult to achieve as the origin of the electrons were randomised over a particular area so as to form the correct focal spot size, in the correct position on the anode, .

Another facet that was considered in the design of the primary generator was the effect of voltage ripple which is a part of every x-ray tube, albeit small, and the effect it may have on the subsequent spectrum production. It was decided that applying a variation in the primary generator's energy to that resembling an apparent voltage ripple, would not affect the spec-

trum and subsequent measurements to a degree that would impact validity measurements.

Although it was straightforward to manipulate example B1's geometry and make other volumes to ultimately produce an x-ray tube, it was often forgotten how Geant4 interpret the values that are entered into their geometry construction methods. A value entered to define a dimension in the XYZ planes is interpreted as the value in both the positive and negative direction, i.e. if 2mm is entered then that dimension will be 4mm. However, when entering a distance outside of volume construction methods, the value is taken as it's true value and not in both positive and negative directions. As a result initial volumes were produced two times the size they should have been, but were corrected once the error was realised.

Additional volumes added to example B1 to build a fully functioning x-ray tube were: a vacuum box for the anode and electron gun to sit in, the Be window, and lead walls appropriately positioned about the anode. The vacuum box and lead walls were important facets to include as outside the x-ray tube was air, where the electron gun would not function properly, and the lead addition to minimise scattering events outside the x-ray tubes housing.

Correctly simulating the x-ray tube specific to a GE Essential was particularly important as it would eliminate many uncertainties in geometric accuracy, giving the simulation the best chance to produce correct data from which to validate against machine measurements.

5.2 Physics Lists and CLHEP Data

After the initial x-ray tube was set up it was particularly important to understand what physical processes were being simulated, and whether they were correct. There are two elements that contribute to Geant4 correctly simulating physical processes, the first is the physics list which hold the cross-sections for all the interactions for each material, and secondly is the CLHEP which, at mammography energies, define the locations of the characteristic peaks for each material.

The physics lists a user can choose from are the Standard, Livermore and Penelope physics lists. The physics list chosen for this project was Pene-

lope. Penelope is regarded as having the most accurate cross-sections at low energies, followed closely by the Livemore and Standard lists. The project could have been carried out with either of the lists with very similar results, and in fact an entire set of data was collected with the Standard physics list unbeknownst to the author.

The error was discovered when a random inspection of the main class file, *main.cc*, was carried out after all data relevant to the project was collected. It was revealed that the Penelope physics list was thought to have been instigated, but wasn't rendering that set of data, including phase-space files, not relevant. The physics list was changed and another set of data was collected. Because this occurred towards the end of the project's time frame, enough experience with Geant4 had been accumulated that the relevant changes were made, and a new data set was collected in a relatively short period; approx. one month. The use of the University of Canterbury physplanck compute cluster proved particularly helpful as many instances of the simulation could be run at one time.

CLHEP is a set of specific classes such as random number generators, physics vectors, geometry and linear algebra that are commonly used in high energy physics software projects. They also define the location of characteristic x-ray peaks in materials defined in Geant4. There are two data sets that come with a common installation of Geant4, one is a default data set and the other stems from data published by Bearden (1967) which are widely accepted values used throughout literature. Although Geant4 simulates the correct physical processes with the correct cross section, the energy at which a characteristic x-ray is emitted differs between the two CLHEP data sets, and this may have affected dosimetry measurements if not discovered through the initial spectrum validation.

5.3 Initial Spectrum Validation and Phase-Space Collection

INITIAL SPECTRUM VALIDATION: The initial spectrum validation was produced using only W as a target material because of the reliable validation source of SpekCalc. It was decided that two energy ranges were taken to contrast the accuracy of a higher energy range to that of a mammography

energy range. When compared to SpekCalc data the higher energy range, 150kVp, produced very good results with the exception of the peaks occuring at 66.95keV and 67.24keV. The simulation data produced distinct characteristic peaks at these energies, but SpekCalc seemed to amalgamate the two into one peak at 67.2keV, thus the specific location and intensity of those peaks couldn't be compared. This was due to the fact that SpekCalc data is produced using results from G. G. Poludniowski and Evans (2007) which states the peak locations and intensities. G. G. Poludniowski and Evans (2007) also gives an insight as to the very poor SpekCalc data at mammography energies, 40kVp, when compared to the Geant4 simulation. This is due to only K-edge peaks being associated with SpekCalc spectra, what is produced is only the bremsstrahlung production calculated from G. G. Poludniowski and Evans (2007).

In contrast to the mammography energy SpekCalc spectrum is the comparison to the spectrum produced from IPEM78 data. Although the comparison isn't perfect and, due to the energy resolution, not all peaks are specifically defined, the comparison is of an acceptable quality. The peaks occur where they're expected and are of expected intensity

INITIAL PHASE-SPACE COLLECTION: The collection of the initial phase-space files and data for initial spectrum validation were collected consecutively. As stated in Section 3.3.1 the phase-space files were collected at $Z = 2.5cm$ and were collimated within the *G4IAEAphspWriter* class file provided by the IAEA. Without the use of extra volumes to collimate the beam, additional forward scatter was minimised and computing time lessened as the collected phase-space files were smaller, and much more specific for the purposes of mammography. However, this method of collimation doesn't replicate the collimation seen on a mammography unit as it has the lead collimator which will produce some scatter. The extent of this effect on subsequent measurements was not determined, but the assumption is that scattering events from lead are minimal at mammography energies due to high mass energy absorption coefficients, so the use of this method shouldn't have had any measurable impact.

The number of photons collected by the phase space files can be estimated as using equation 2.1 to give a ball park figure as to the efficiency of the simulated x-ray anode. For example taking an Mo anode at 24kV the estimated efficiency is 1.2×10^{-3}, multiplying this figure by the quantity of incident electrons, 2×10^9, gives 2.46×10^6 photons over an entire sphere (assuming a point source). But the phase-space file is only collected over a small area at Z = $2.5cm$, or a radius of 2.5cm, thus taking the ratio of areas and multiplying by the number of photons one gets 32000 photons. In fact the number of photons collected was 39000 for an Mo anode at 24kV, but as the ball park figure neglects multiple interactions and potential forward scatter, one can then infer that the simulated anode is performing adequately.

However, using the phase-space files proved a lot more difficult to have perform efficiently than simply "plugging them in and making them go". Ordinarily a user might be able to do just that depending on their experimental requirements, but for the purposes of the phase space files used here, a slightly deeper knowledge of their operation was required.

The primary purpose for using phase-space files in this project was to record spectral data and particular Z locations so one could load those files and have them cycle many times to improve counting statistics and computational time. The issue, however, was that due to phase-space files originating from interactions of 2×10^9 electrons, the electrons that resulted in no recorded photon was viewed as a null event, and was subsequently recorded as such in the phase-space file. Thus when one attempts to use the file, the photon production efficiency is again loaded into the run, i.e. to cycle through the entire phase-space file of 39000 photons, a run of 2×10^9 was required which took as long as the original run. To solve this the recorded null events had to be discarded, which meant simply changing the value of a specific term in the *.IAEAheader* file from 1 to 0.

Although this seems trivial, the solution didn't seem to be common knowledge throughout the Geant4 community, but in solving the issue it enabled the use of phase-space files throughout the simulation without any efficiency restrictions. If it were unable to be solved, this issue would have represented a significant hurdle to overcome using other workarounds that may not have been as elegant as the IAEA methods, nor as time efficient.

5.4 Filter Transmission

The initial phase space files were used to collect filter transmission data so as to calculate mean energies, HVLs and tube yield as part of the validation process, and record further phase-space files at other Z locations. Solving the phase-space issue meant the phase-space files could be cycled numerous times to produce a large quantity of histories for good counting statistics, and to calculate these quantities as accurately as possible.

The results presented for the filter transmission were calculated with a very good fit to a cubic function, which was not expected. Archers equation describes the transmission of x-rays through shielding, and one might naturally assume that it could be used for the likes of transmission of a spectrum through other materials such as filter materials. But the only way that it could be fitted was to modify it slightly, as described in Appendix B, but still proved inaccurate over the simulated filter thickness range, albeit a good fit from 0mm, or a transmission of 1.

Because mammography uses low energies, and the tissue being imaged has very subtle attenuation differences, it was important to minimise uncertainty as much as possible which is why the fitted cubic functions and their uncertainties were used.

The HVLs and mean energies were measured with good accuracy to Boone et al. (1997), and although not documented here, an inspection of values calculated in IPEM78 also saw a good agreement similar to that in Boone et al. (1997). Although the mean calculated uncertainties were good, which stemmed from statistical uncertainty and filter transmission errors, there were some apparent outlying figures differing by as much as 2mmAL HVL and 1keV mean energies. These equated to 6.6% and 4.0% respectively, so although they looked large on initial inspection they don't differ too much from the mean calculated uncertainties and fall well within the maximum reported uncertainty.

The tube yield values offered a good indication as to the overall functionality of the simulation, and in particular how the simulated physical processes of Geant4 amalgamate to ultimately record a dose. The difference between some simulation figures and validation measurements seem very high,

as much as 21%, but because mammography is particularly sensitive to any variation in geometric accuracy, material density and cross-sections, it is reasonable to conclude that at lower energies those differences would manifest more than those at higher energies. As a measure of the overall simulation validity, one can view these figures as acceptable; if the simulation had a catastrophic unforeseeable error these figures would not compare as they do. The accuracy of the HVL, mean energy and tube yield measurements give the simulation a credibility with the advent of subsequent measurements.

5.5 Breast Transmission

The breast transmission parameters that were chosen to be simulated were based primarily on what was able to be validated on the GE Essential, as well as limiting the quantity of data to that which is relevant. Additionally a W/Al anode/filter combination was simulated to give an objective comparison to the Mo/Mo and Mo/Rh anode/filter combinations. The energies were also selected to limit the quantity of relevant data, and with 2kV energy intervals the odd energies that were not simulated could be interpolated to a reasonable accuracy if need be.

The breast transmission results fitted particularly well to the double exponential over the range of breast thicknesses simulated. Again, as with the filter transmission, the transmission fit was done only over the simulated thicknesses as the accuracy at this point of the project was important, and a more detailed view of the data was required. Also, the transmission through breasts less than 20mm in thickness would not provide any more relevant data as those compressed breast thicknesses are very uncommon (Geeraert et al., 2012).

Given the differences between PMMA and waters mass attenuation coefficients over the simulated energy range (Figure 5.1), the recorded transmission values are what would be expected. Although the mass attenuation coefficients look minimal, cumulatively the differences would become more pronounced; the log scale on the Y axis is to visually enhance the smaller coefficients at higher energies, but can still give a false impression on the quantity of the differences.

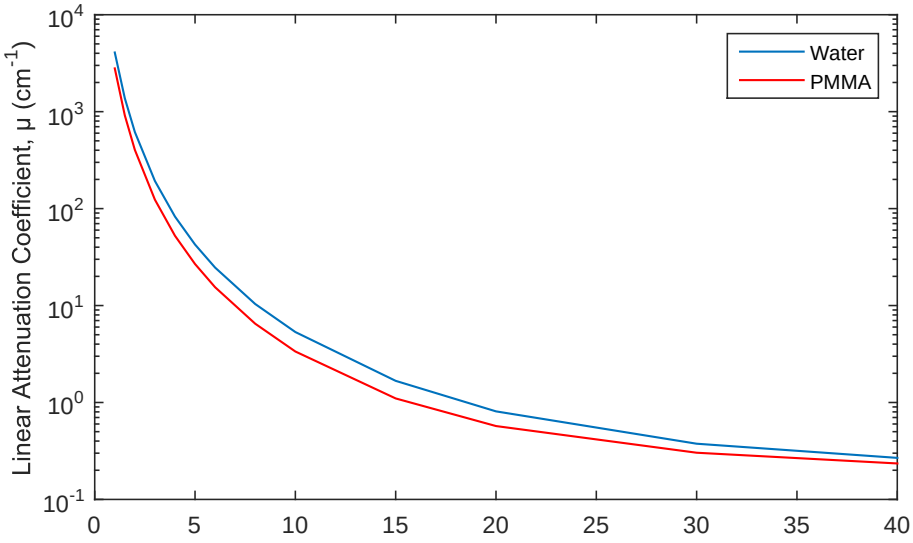

Figure 5.1: Water and PMMA linear attenuation coefficients up to 40keV.

The simulated model of a water equivalent thickness could be established after these measurements were taken, and the results (examples found in Section 4.5 and 5.6) made sense based on the discussion above regarding attenuation of the two materials. Not only was a breast thickness able to be described radiographically as a water equivalent thickness, but can be associated with a glandularity and equivalent breast thickness from Dance et al. (2000). The parameters used to calculate a water equivalent thickness can all be found in DICOM mammography image header data, those being the anode material, filter material and thickness and breast thickness, which can then be reverse engineered to a water equivalent thickness.

DOSE vs KERMA: The breast transmission phase of the project was where it became apparent that the measurement of dose using Geant4 methods wasn't possible as the location of a detector volume to adjacent volumes was too close to obtain consistent results. This was primarily due to electron density disparities between the materials of the detector volume (air), and adjacent volumes (PMMA, skin, lead, carbon fibre), leading to differences in

ionisation probabilities. This was able to be temporarily solved by simply putting a gap equal to, or greater than, in distance to the range of an electron in air. This in turn perturbed the geometry significantly, meaning a number of IVS corrections would have to be applied to obtain accurate results. This may have worked, but had the potential to introduce additional errors into the dose calculations.

A significant quantity of testing was carried out with differing gaps, detector thicknesses and sizes, as well as trialling third party code which claimed to calculate a kerma equivalent dose to try to get a dose measurement to work. Unfortunately this was to no avail, thus a kerma measurement was developed using a more formal approach described in Section 2.3.4. However when testing the dose measurement against the new kerma measurement to see if they matched, it was discovered that there seemed to be a blanket 2% maximum difference between the two regardless of beam parameters. This was ultimately solved by adjusting the function fitted to the NIST data that was used to calculate the attenuation coefficient. Although the issue was solved there was still some apprehension on the accuracy of the kerma measurements despite validation tests (HVL, mean energy and tube yield) stating otherwise. As such it was determined to impose an additional 1% uncertainty on kerma measurements to cover any unforeseen residual differences.

5.6 Model Valdiation

Measurements from a GE Essential was a last minute addition to the end of this project and it proved to be extremely valuable for validation. The first validation step was to calculate a tube yield from the entrance kerma measurements, which has already been discussed, and secondly was to calculate PMMA transmission curves to compare to the simulated transmission curves.

Initially the GE Essential transmission curves were plotted as a function of 20mm PMMA thicknesses and the disparity between simulated and GE Essential transmission functions seemed very large, however as mentioned in Section 4.5 the blocks were in fact 19mm thick each. With the addition of a correct IVS correction, the new fitted functions reduced the apparent

differences markedly to where the function's fell within each others errorbars. An example of this can be found in Figure 4.10 and 5.2.

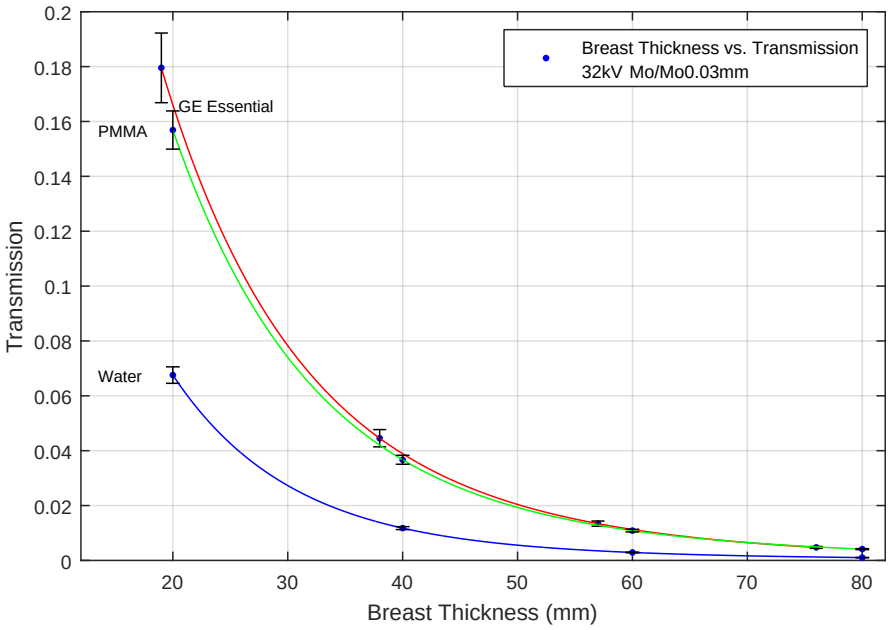

Figure 5.2: Transmission data for Geant4 water and PMMA simulation versus GE Essential: 32kV Mo/Mo 0.03mm anode/filter combination.

However the general difference between GE Essential and simulated transmission functions is that the GE Essential transmission has consistently measured slightly higher values, but generally fall within each others errorbars. The source of the difference in transmission can be linked back to the discussion on geometric accuracy between the simulation and the GE Essential unit, and also manufacturing uncertainties. In terms of geometric set up, what was simulated was based on data received from the manufacturer, but how accurate the components are on a GE Essential are subject to the potential aforementioned deviation sources. Even slight inaccuracies, perhaps in the order the accuracy of their measurement, would cumulatively lead to a measurable difference between simulated and real world measurements. A difference in material densities, or elemental constituents would also play a role. With these factors in mind the overall results of this project have been good, falling within reasonable expected limits, and leading to what can be

viewed as an accurate simulation that has been validated with real world measurements.

ANOTHER EXAMPLE CALCULATION: To calculate another water equivalent thickness from Figure 5.2 using the simulated data: say a breast thickness of 50mm is imaged and that corresponds to the equivalent breast thickness of 50mm. A PMMA thickness can then be calculated to be $43.2mm \pm 2.2mm$, this can now be used to calculate a water equivalent thickness of $29.1mm \pm 2.0mm$ with an associated glandularity of $49.0\% \pm 2.4\%$ if between $40 - 49$years, and $32.9\% \pm 1.6\%$ if between years $50 - 64$.

If the GE Essential data is now used with the simulated water transmission, the PMMA thickness is still $43.2mm \pm 2.2mm$ but the water equivalent thickness is $28.4mm \pm 2.0mm$ with the aforementioned glandularities. If the validation data was to be totally comprehensive, a water transmission would have been taken from the GE Essential and a transmission calculated from that. But using liquid water around an expensive technical machine wasn't within the authors budget to repair if an accident were to occur.

Chapter VI

Conclusion, Limitations and Future Work

The primary aim of this project was to describe the radiographic characteristics of a breast in terms of a water equivalent thickness. To achieve this a Geant4 simulation of the mammography imaging process was developed to measure those characteristics from which a water equivalent thickness was determined for the first time. These simulated measurements were compared to real world measurements taken from a GE Senograph Essential mammography unit, and those measurements agreed with the simulated measurements to within uncertainty calculations.

Using Geant4 to develop the simulation enabled a wide array of experimental flexibility to be accessible, which greatly aided in the design and construction of the project overall. This variability led to the accurate simulation of geometric, and x-ray beam parameters readily found in the header of a mammography DICOM image, giving the simulation the level of precision required to successfully simulate a very sensitive imaging modality. The simulation was therefore able to produce measurements that describe a breast thickness as a quantity (water equivalent thickness) that is easily understood and articulated.

Although the simulation successfully achieved it's goal, it was limited to one specific mammography unit which has a specific set of geometric features. The data was therefore tailored to a GE Essential and it's characteristics, but due to the flexibility of Geant4 the specific parameters can easily be changed to account for other units. Because Geant4 is a C++ based toolkit, a great deal of experience was obtained with this programming language over the course of the project. Even towards the end of the project it seemed as though there were still better methods and techniques to learn and use that would have been beneficial.

One particular facet of the project that would have been done differently,

if done again, would be to take real world measurements early so as to adapt the simulation to any unforeseen hurdles that might have been present; i.e. detector placement. In terms of future work, this would be especially advantageous as other mammography units have geometries that differ slightly between manufacturers.

The possibility of future work would, firstly, extend this project to incorporate a greater set of simulated data, that being to fill in the energy gaps that are presented here. Additionally one could investigate the effect that a change in geometry dimensions would have on the outcome of the transmission figures. Those might include anode angle, breast support thickness, compression paddle thickness, collimation and grid ratio, as well as a raft of other geometry changes that may affect transmission. Ultimately one could obtain transmission curves to calculate a water equivalent thickness for most mammography units on the market today. Further extensions could include other radiography techniques such as plain radiography, or dental radiography.

Appendix A

Filtered and Unfiltered Spectra

A.1 Unfiltered Spectra

The following Molybdenum(Mo), Rhodium(Rh) and Tungsten(W) unfiltered spectra have a range of 24kVp - 36kVp and are graphed in 2kVp intervals to highlight spectral differences. Each spectrum has a bin width of 0.5keV, thus some photo-peaks are not defined, particularly in the Tungsten spectra; inherent filtration was 0.69mm Be.

Below are characteristic peak energies associated with each material's spectrum, and their relative intensity (Bearden, 1967; Dewey et al., 1969; Salem et al., 1974).

Table A.1: K-series characteristic X-ray line energies for Mo and Rh (keV).

Z	**Material**	**K edge**	**K-series**				
42	Mo	20.002	19.960	19.608	19.590	17.479	17.374
45	Rh	23.229	23.173	22.723	22.698	20.216	20.073
	Intensity(%)	–	~ 5	~ 20	~ 10	100	~ 53

Table A.2: L-series characteristic X-ray line energies for W (keV).

Z	**Material**	**L1 edge**	**L1-series**		
74	W	12.092	11.675	9.819	9.526
	Intensity(%)	–	~ 5	27	20

Z	**Material**	**L2 edge**	**L2-series**	
74	W	11.535	11.284	9.671
	Intensity(%)	–	16	100

Z	**Material**	**L3 edge**	**L3-series**			
74	W	10.199	10.273	8.651	8.584	7.604
	Intensity(%)	–	13	~ 90	10	12

Mo and Rh L-series characteristic energies and relative intensities have been left out as they don't provide any further enlightenment to their spectra, given the energy resolution.

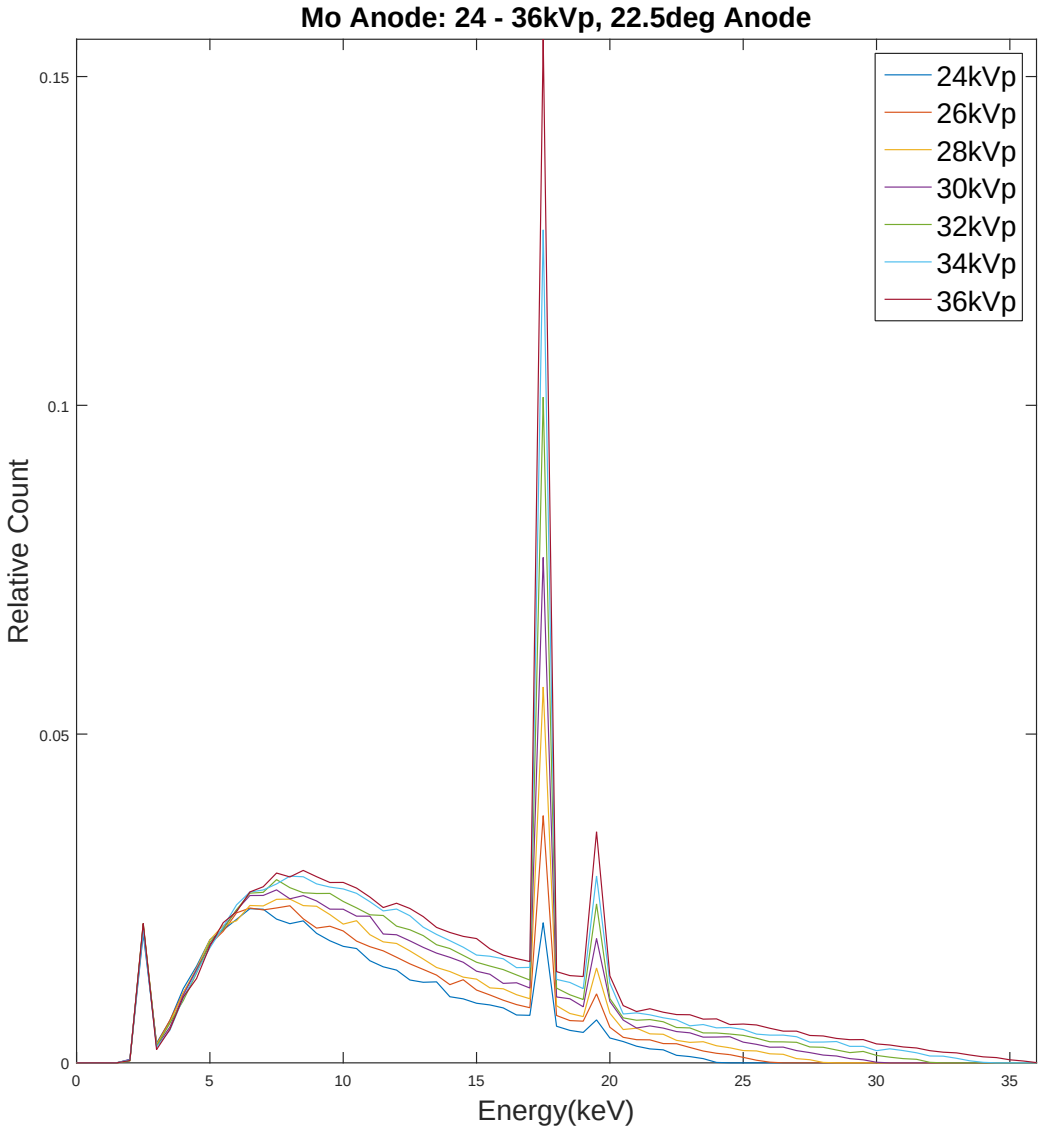

Figure A.1: Molybdenum unfiltered spectra.

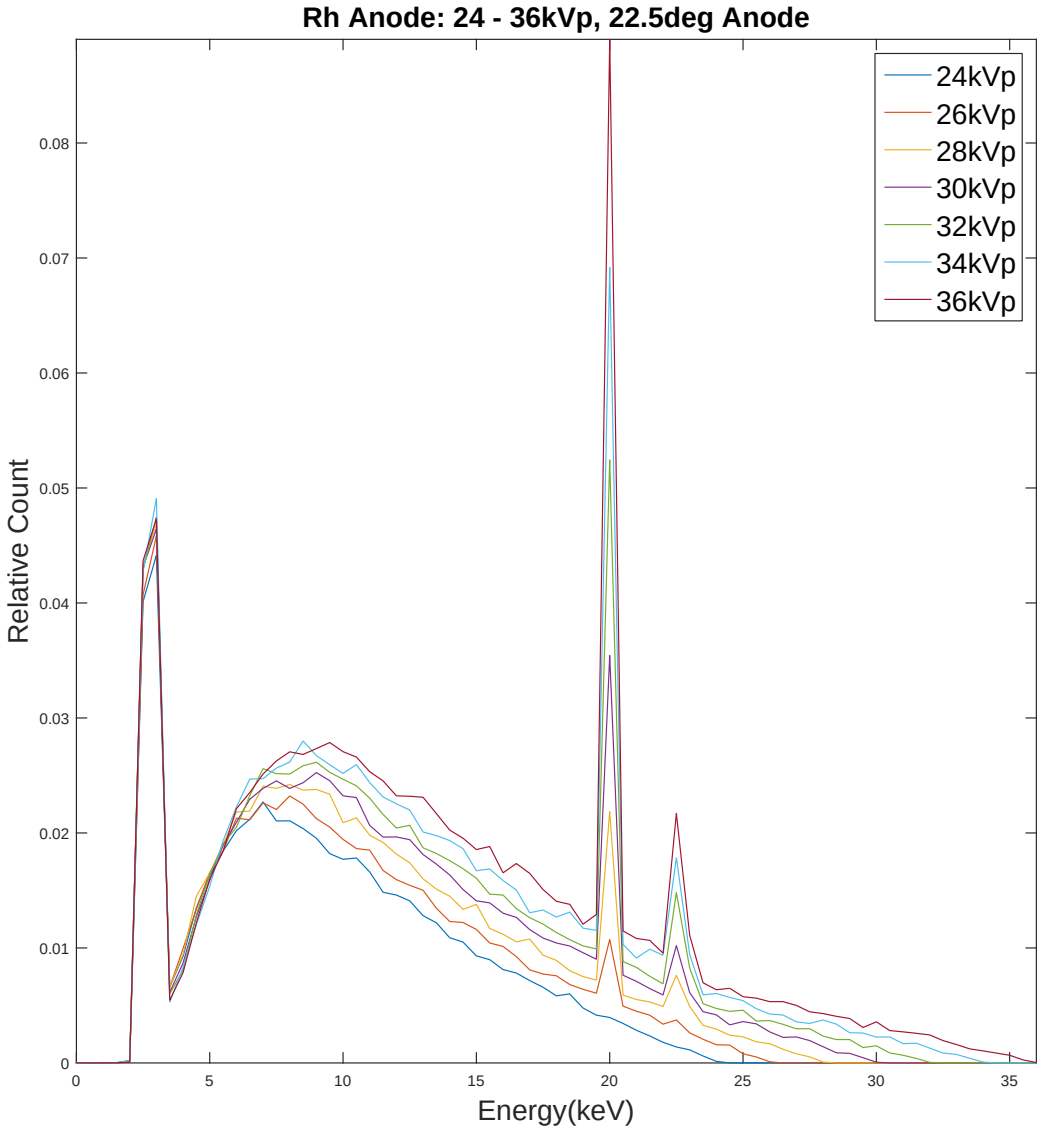

Figure A.2: Rhodium unfiltered spectra.

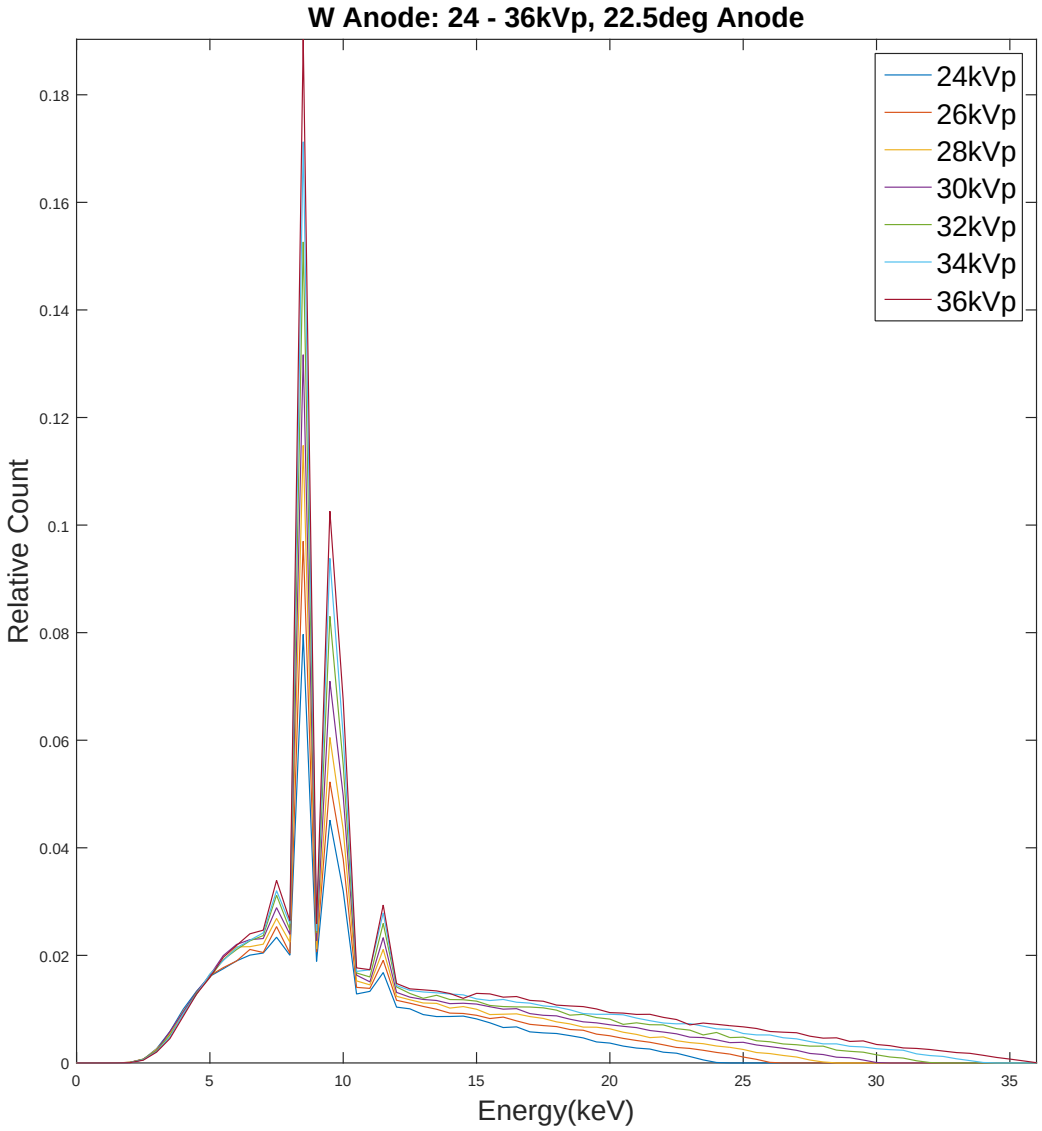

Figure A.3: Tungsten unfiltered spectra.

A.2 Filtered Spectra

Energies chosen to visually represent how the spectrum changes with increasing energy. Counts have not been normalised, so as to depict how they change with energy. Bin width is 0.5keV.

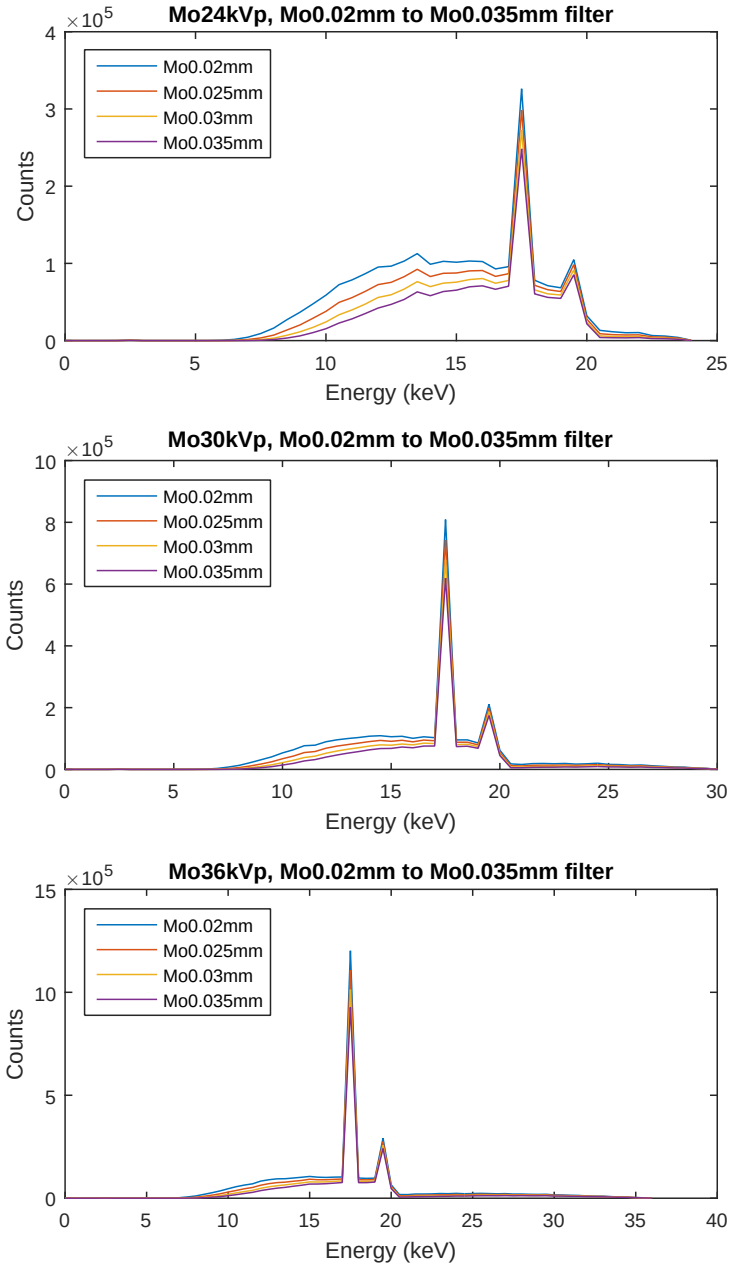

Figure A.4: Molybdenum spectra at 24, 30 and 36kVp with a Molybdenum filter.

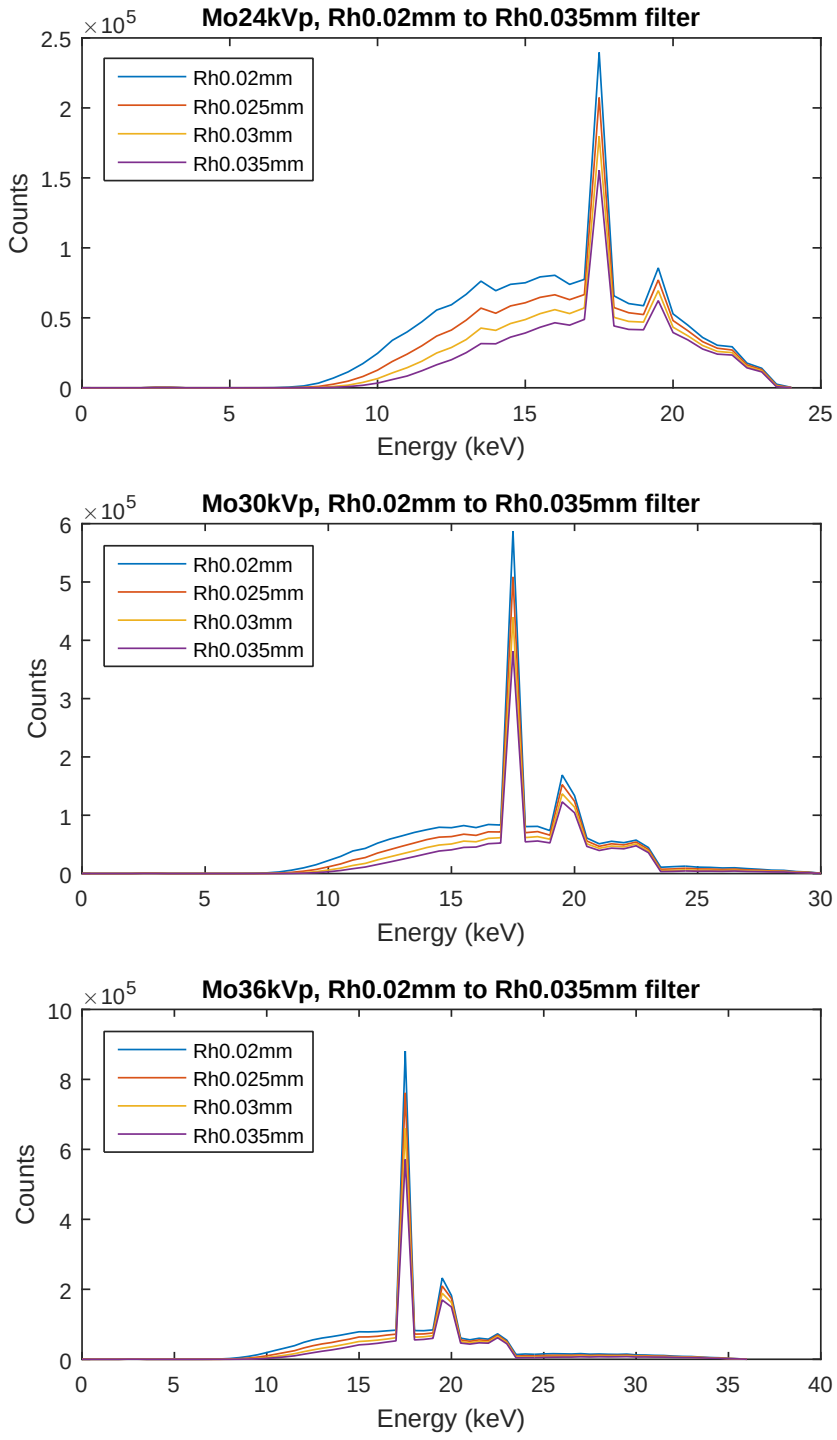

Figure A.5: Molybdenum spectra at 24, 30 and 36kVp with a Rhodium filter.

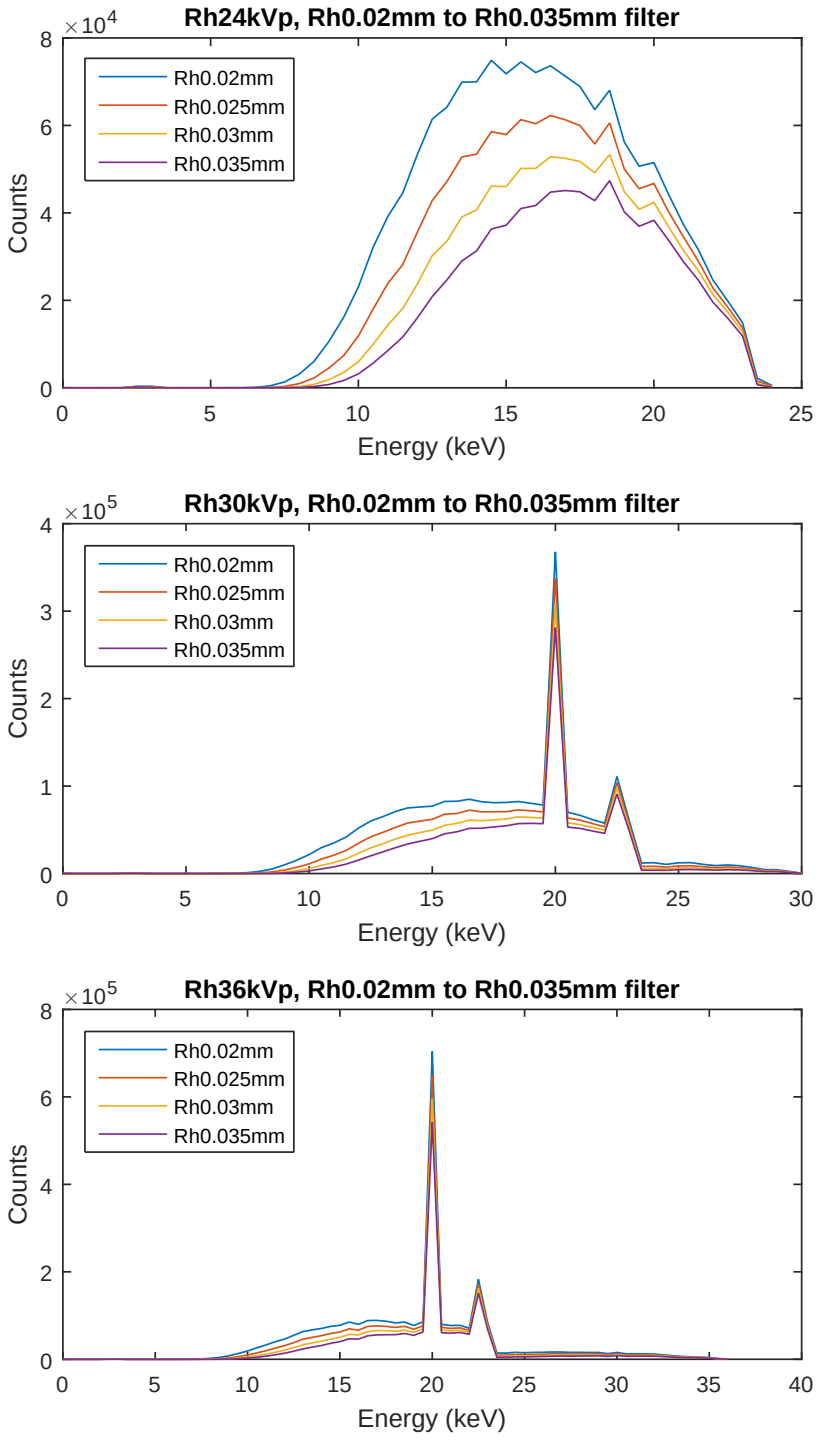

Figure A.6: Rhodium spectra at 24, 30 and 36kVp with a Rhodium filter.

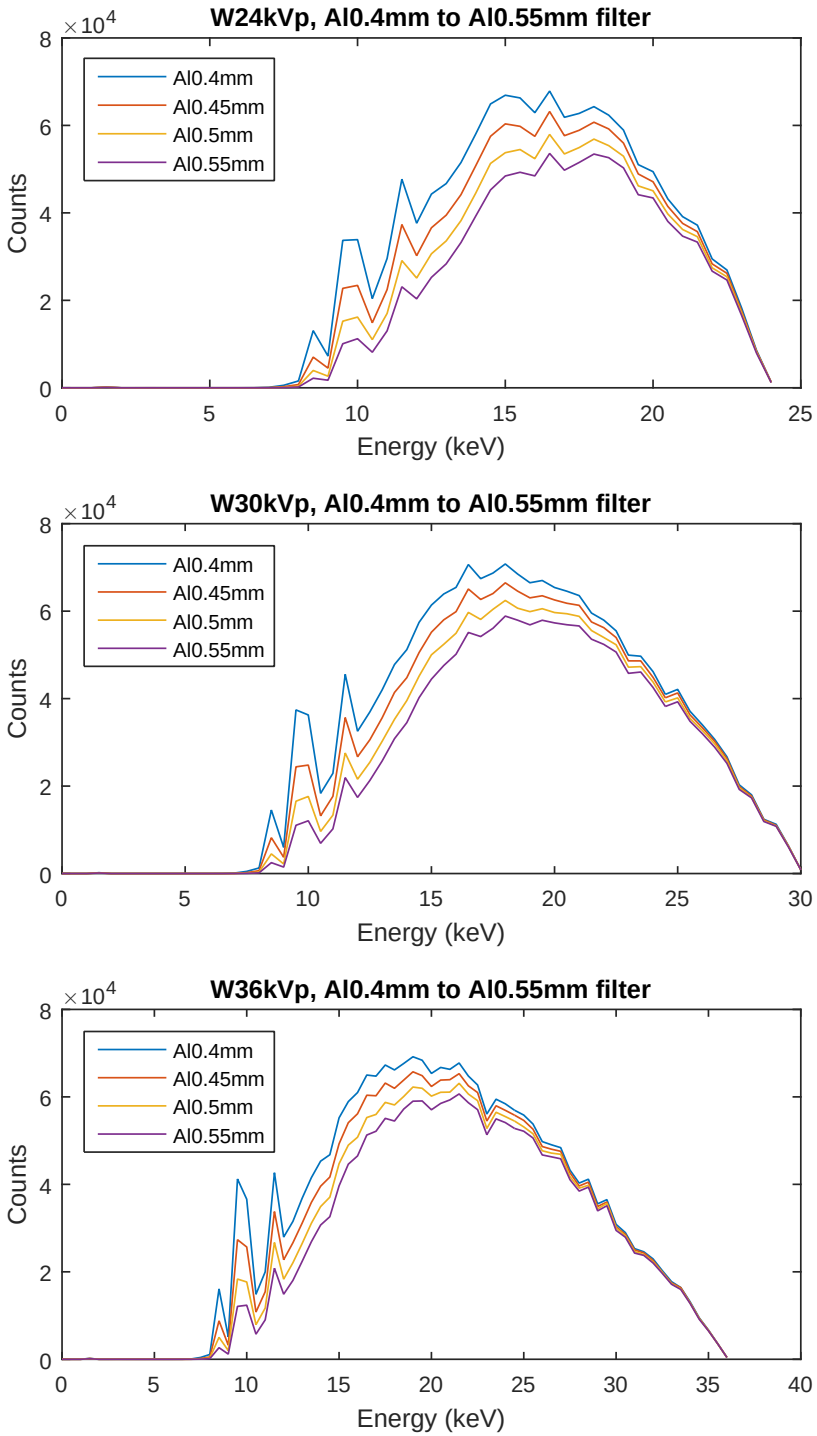

Figure A.7: Tungsten spectra at 24, 30 and 36kVp with an Aluminium filter.

Appendix B

Filter Transmission from Modified Archer Equation

Archer's equation describes the broad beam transmission of x-rays through a medium, or shielding barrier, as the ratio of air kerma from an attenuated beam to that of an unshielded beam as a function of the shielding thickness x:

$$\mathrm{B(x)} = \frac{K(x)}{K_0} \tag{B.1}$$

(Li, Zhang, & Liu, 2012). This can be modelled on Archer's equation:

$$\mathrm{B} = \left[\left(1 + \frac{\beta}{\alpha}\right)e^{\alpha\gamma x} - \frac{\beta}{\alpha}\right]^{-\frac{1}{\gamma}} \tag{B.2}$$

where α, β and γ are fitted parameters that are dependant on the beam's kVp (Archer, Thornby, & Bushong, 1983). However, when attempting to implement this equation on the simulated filter transmission, ascertaining appropriate fitted parameters proved challenging, thus a slightly modified version was adapted with acceptable results; the $-1/\gamma$ became positive:

$$\mathrm{B} = \left[\left(1 + \frac{\beta}{\alpha}\right)e^{\alpha\gamma x} - \frac{\beta}{\alpha}\right]^{\frac{1}{\gamma}} \tag{B.3}$$

The filter thickness could therefore be calculated using:

$$x = \frac{1}{\alpha\beta} ln\left[\frac{B^{\gamma} + \frac{\beta}{\alpha}}{1 + \frac{\beta}{\alpha}}\right] \tag{B.4}$$

This lead to a mean $\mathrm{R}^2 = 1$ and a mean RMSE$= 3.2 \times 10^{-4}$, with a maximum RMSE$= 1.2 \times 10^{-3}$ and a minimum RMSE$= 3.5 \times 10^{-6}$. Although this seems to be relatively accurate from a thickness of 0mm, it was discovered to be fairly inaccurate over the thickness ranges the simulated measurements were taken, $0.02 - 0.035$mm for Mo and Rh, and $0.4 - 0.55$mm for Al.

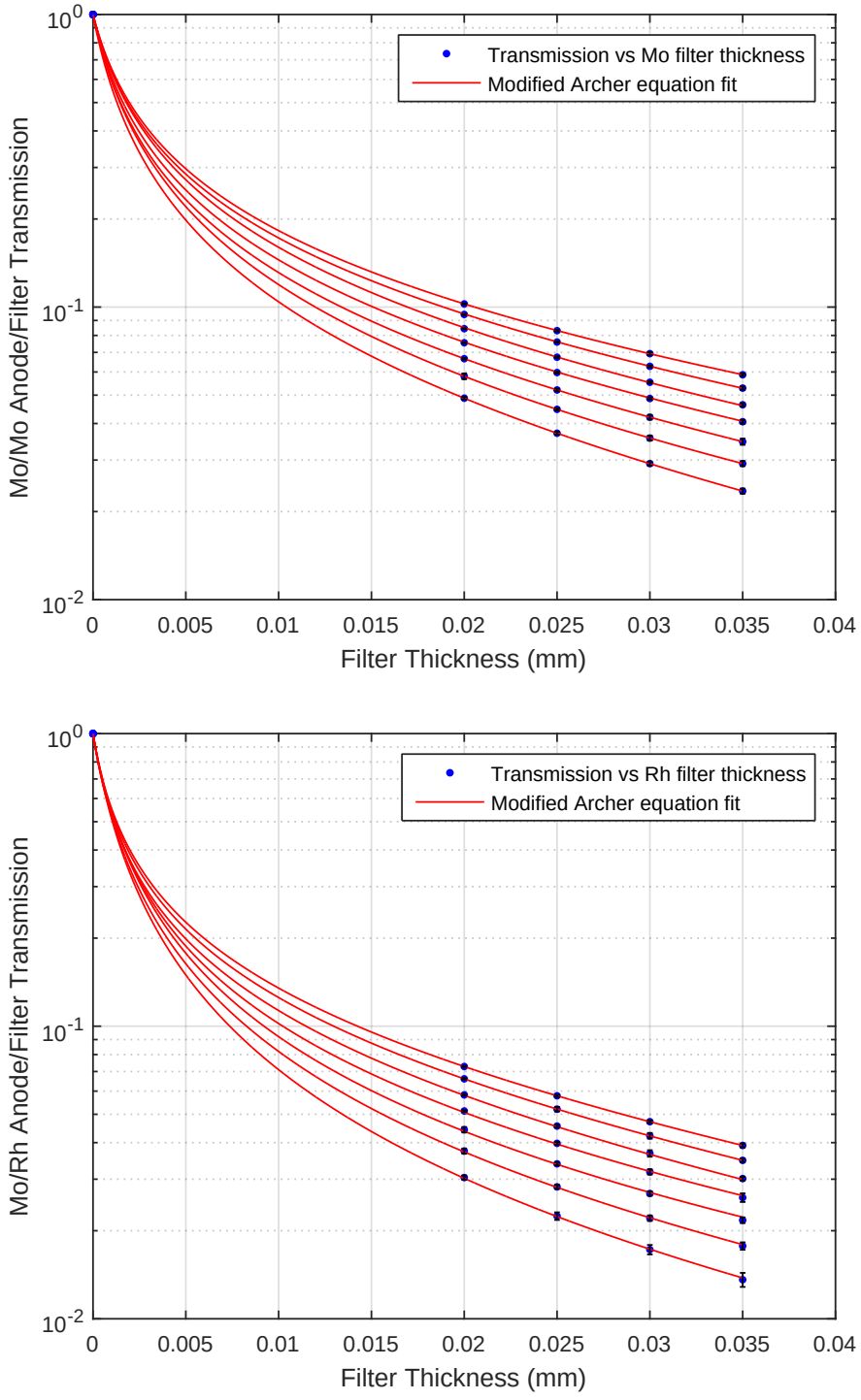

Figure B.1: Modified Archers equation transmission fit, results for Mo/Mo (top) anode/filter and Mo/Rh (bottom) anode/filter.

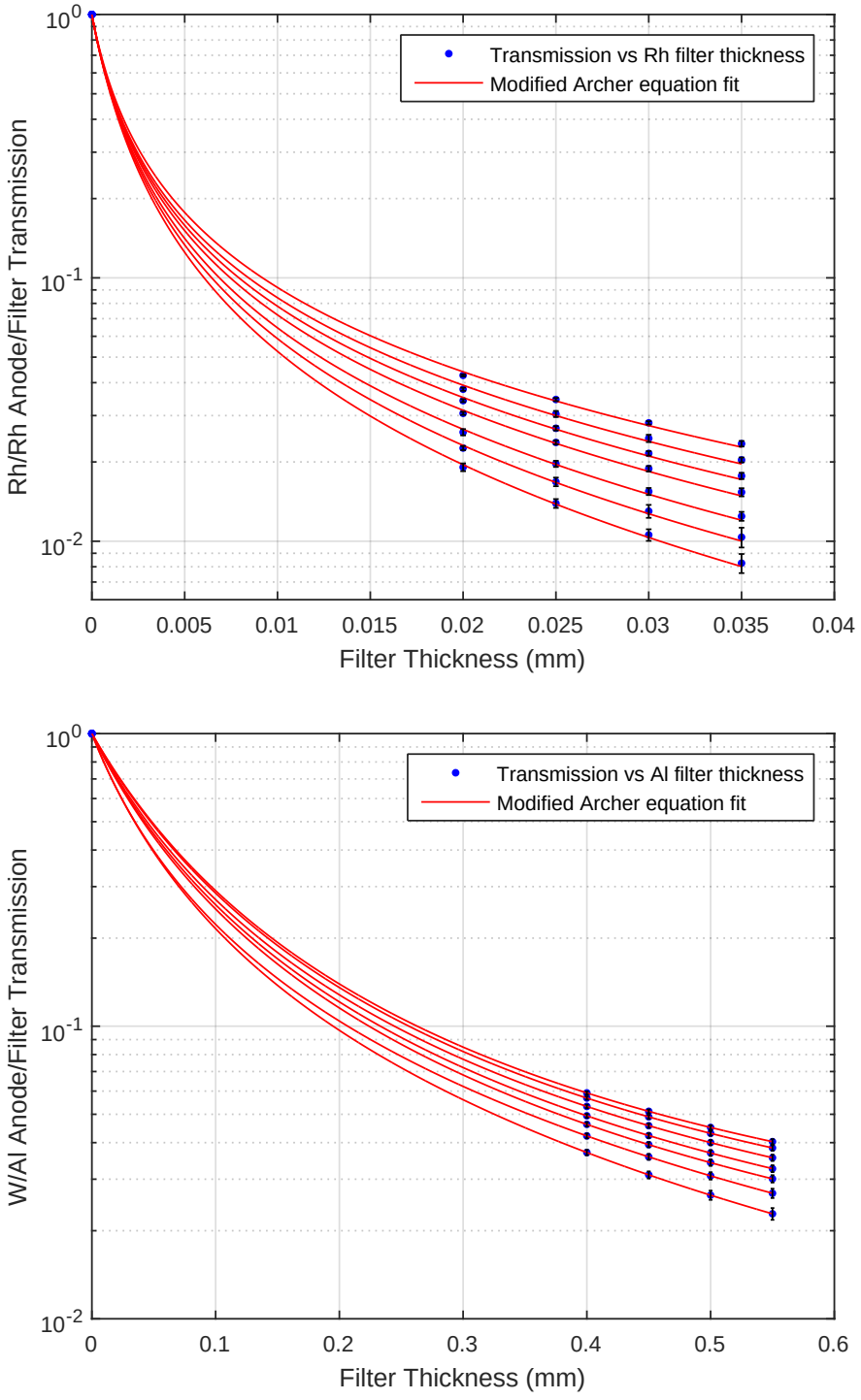

Figure B.2: Modified Archers equation transmission fit, results for Rh/Rh (top) anode/filter and W/Al (bottom) anode/filter.

Table B.1: Coefficients for the modified Archer's equation described above, values are accurate to 4 decimal places.

		Coefficients		
Anode/Filter	**Energy(keV)**	**a**	**b**	**c**
Mo/Mo	*24*	-23.8141	-739.1483	-1.0016
	26	-20.4549	-665.3418	-1.0234
	28	-21.4573	-672.9564	-1.1258
	30	-19.9491	-628.7198	-1.1672
	32	-20.5791	-569.9529	-1.2027
	34	-20.5556	-569.9621	-1.2962
	36	-18.4129	-547.2868	-1.3208
Mo/Rh	*24*	-17.4518	-869.4613	-0.8254
	26	-17.7630	-869.4271	-0.9117
	28	-13.8843	-829.5573	-0.9445
	30	-18.6955	-869.3116	-1.0719
	32	-26.4267	-933.2615	-1.2483
	34	-26.3701	-890.3280	-1.3179
	36	-25.9448	-864.6530	-1.3758
Rh/Rh	*24*	-13.5049	-869.8138	-0.6500
	26	-12.7497	-869.8574	-0.7167
	28	-12.7142	-869.8632	-0.7616
	30	-12.8800	-869.8612	-0.8213
	32	-12.7032	-869.8734	-0.8641
	34	-12.8136	-869.8736	-0.9100
	36	-10.9644	-829.9214	-0.9323
W/Al	*24*	-0.0921	-24.6721	-0.5833
	26	-0.1002	-24.8685	-0.6318
	28	2.2538	-22.3306	-0.4472
	30	2.5549	-21.9822	-0.4396
	32	2.9054	-21.5211	-0.4281
	34	4.1346	-21.4744	-0.3764
	36	4.5052	-21.4781	-0.3671

Appendix C

HVL, Mean Energy and Yield

Table C.1: HVL for Mo, Rh and W anodes. 0.02 - 0.035mm Mo and Rh filters for Mo and Rh anodes, and 0.4 - 0.55mm Al for W anode; 24 - 36kVp.

Mo Anode		**24**	**26**	**28**	**30**	**32**	**34**	**36**
Filter	**Thickness**	**HVL(mmAl)**						
Mo	0.02	0.257	0.283	0.300	0.320	0.336	0.350	0.367
	0.025	0.280	0.307	0.323	0.344	0.360	0.372	0.395
	0.03	0.302	0.328	0.346	0.365	0.380	0.394	0.409
	0.035	0.321	0.347	0.364	0.381	0.397	0.410	0.425
Rh	0.02	0.320	0.352	0.373	0.391	0.406	0.419	0.437
	0.025	0.353	0.386	0.405	0.423	0.439	0.449	0.466
	0.03	0.381	0.416	0.434	0.450	0.465	0.474	0.490
	0.035	0.408	0.439	0.459	0.474	0.486	0.496	0.509
Rh Anode								
Rh	0.02	0.300	0.334	0.364	0.391	0.411	0.436	0.456
	0.025	0.332	0.370	0.401	0.430	0.453	0.477	0.497
	0.03	0.363	0.404	0.436	0.466	0.486	0.512	0.531
	0.035	0.388	0.433	0.467	0.495	0.517	0.545	0.561
Al	0.4	0.306	0.337	0.363	0.386	0.408	0.428	0.447
	0.45	0.326	0.361	0.392	0.416	0.443	0.465	0.488
	0.5	0.349	0.384	0.417	0.444	0.474	0.498	0.526
	0.55	0.367	0.404	0.442	0.471	0.502	0.531	0.559

Table C.2: Mean energy for Mo, Rh and W anodes. 0.02 - 0.035mm Mo and Rh filters for Mo and Rh anodes, and 0.4 - 0.55mm Al for W anode; 24 - 36kVp.

Mo Anode		**24**	**26**	**28**	**30**	**32**	**34**	**36**
Filter	**Thickness**	**Mean energy(keV)**						
Mo	0.02	14.96	15.48	15.92	16.37	16.74	17.13	17.51
	0.025	15.31	15.79	16.20	16.61	16.96	17.33	17.69
	0.03	15.59	16.04	16.41	16.79	17.13	17.48	17.83
	0.035	15.83	16.24	16.59	16.93	17.25	17.59	17.92
Rh	0.02	16.10	16.61	17.01	17.38	17.70	18.02	18.34
	0.025	16.53	17.00	17.36	17.69	17.96	18.26	18.56
	0.03	16.87	17.32	17.63	17.92	18.17	18.45	18.72
	0.035	17.17	17.58	17.86	18.12	18.34	18.59	18.84
Rh Anode								
Rh	0.02	15.92	16.67	17.32	17.84	18.33	18.79	19.18
	0.025	16.38	17.12	17.74	18.21	18.67	19.09	19.45
	0.03	16.77	17.49	18.08	18.51	18.94	19.33	19.66
	0.035	17.09	17.80	18.36	18.75	19.16	19.51	19.83
W Anode								
Al	0.4	16.16	17.04	17.84	18.61	19.41	20.18	20.94
	0.45	16.48	17.37	18.18	18.99	19.78	20.58	21.35
	0.5	16.74	17.66	18.48	19.30	20.12	20.93	21.71
	0.55	16.98	17.91	18.75	19.58	20.41	21.23	22.02

Table C.3: Yield for Mo, Rh and W anodes. 0.02 - 0.035mm Mo and Rh filters for Mo and Rh anodes, and 0.4 - 0.55mm Al for W anode; 24 - 36kVp.

Mo Anode		**24**	**26**	**28**	**30**	**32**	**34**	**36**
Filter	**Thickness**	**Yield(μGy/mAs)**						
Mo	0.02	112.0	144.0	174.6	208.4	244.6	279.1	318.9
	0.025	90.4	117.5	143.5	172.5	203.6	233.8	268.0
	0.03	74.2	97.7	119.7	145.1	172.0	198.0	228.7
	0.035	61.7	82.2	101.2	123.5	146.9	170.0	197.0
Rh	0.02	79.2	105.2	130.3	157.9	186.9	215.2	248.7
	0.025	61.4	83.1	103.8	126.8	150.7	174.6	203.1
	0.03	48.9	66.9	84.4	103.7	123.9	143.9	168.3
	0.035	39.4	55.0	69.6	86.1	103.3	120.3	141.4
Rh Anode								
Rh	0.02	69.8	89.8	111.3	138.8	162.1	188.5	217.7
	0.025	53.5	70.1	88.1	110.8	130.2	152.7	177.2
	0.03	41.9	55.9	71.1	90.3	106.9	126.1	147.3
	0.035	33.5	45.5	58.5	75.0	89.4	105.8	124.4
W Anode								
Al	0.4	67.0	83.8	101.3	118.6	135.3	156.3	173.2
	0.45	58.3	73.5	89.3	105.2	120.1	139.4	154.8
	0.5	51.0	65.1	79.6	94.2	108.1	126.0	140.1
	0.55	45.2	58.2	71.4	84.9	98.0	114.3	127.8

Appendix D

Breast Transmission

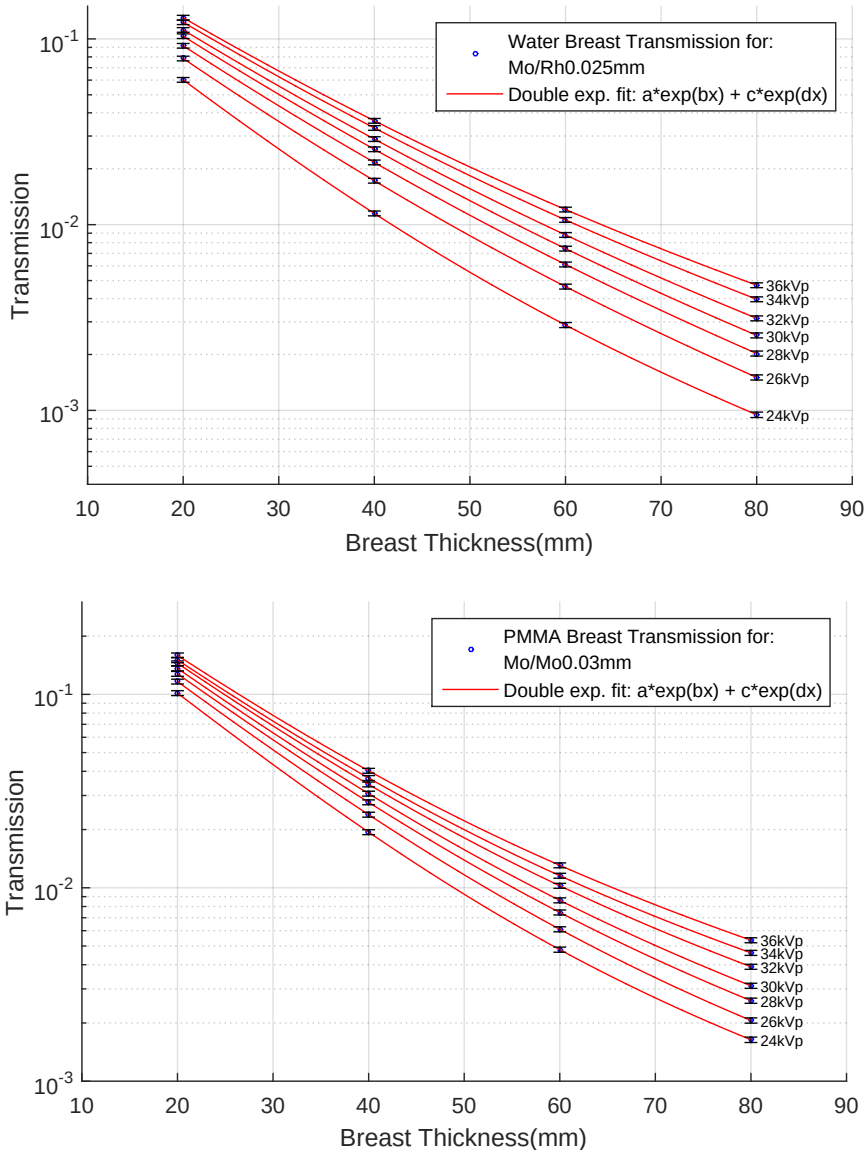

Figure D.1: Water and PMMA breast transmission for Mo/Mo anode/filter.

Table D.1: Mo anode and Mo filter breast transmission fitted function coefficients for a water breast.

Mo Anode	**Energy**	**Coefficients**			
Mo Filter	**(keV)**	**a**	**b**	**c**	**d**
0.02mm	*24*	0.2011	-0.1209	0.0268	-0.0727
	26	0.2280	-0.1205	0.0373	-0.0687
	28	0.2515	-0.1136	0.0281	-0.0580
	30	0.2663	-0.1119	0.0299	-0.0538
	32	0.2770	-0.1085	0.0281	-0.0475
	34	0.2852	-0.1070	0.0291	-0.0444
	36	0.2975	-0.1067	0.0332	-0.0428
0.025mm	*24*	0.2214	-0.1182	0.0238	-0.0717
	26	0.2483	-0.1139	0.0250	-0.0648
	28	0.2721	-0.1137	0.0286	-0.0584
	30	0.2886	-0.1125	0.0307	-0.0545
	32	0.2986	-0.1083	0.0267	-0.0471
	34	0.3094	-0.1086	0.0305	-0.0448
	36	0.3179	-0.1068	0.0322	-0.0424
0.03mm	*24*	0.2349	-0.1250	0.0451	-0.0783
	26	0.2710	-0.1135	0.0231	-0.0640
	28	0.2926	-0.1153	0.0335	-0.0609
	30	0.3020	-0.1076	0.0205	-0.0503
	32	0.3219	-0.1098	0.0281	-0.0478
	34	0.3215	-0.1066	0.0270	-0.0437
	36	0.3364	-0.1077	0.0331	-0.0428
0.035mm	*24*	0.2389	-0.1350	0.0804	-0.0848
	24	0.2881	-0.1149	0.0292	-0.0669
	24	0.3126	-0.1179	0.0402	-0.0634
	24	0.3180	-0.1092	0.0237	-0.0523
	24	0.3352	-0.1089	0.0264	-0.0478
	24	0.3431	-0.1083	0.0286	-0.0446
	24	0.3547	-0.1070	0.0293	-0.0415

Table D.2: Mo anode and Rh filter breast transmission fitted function coefficients for a water breast.

Mo Anode	**Energy**	**Coefficients**			
Rh Filter	**(keV)**	**a**	**b**	**c**	**d**
0.02mm	*24*	0.2116	-0.1293	0.0719	-0.0721
	26	0.2099	-0.1205	0.0934	-0.0672
	28	0.2311	-0.1147	0.1008	-0.0631
	30	0.2509	-0.0997	0.0765	-0.0567
	32	0.2593	-0.1025	0.0935	-0.0558
	34	0.3259	-0.1147	0.1124	-0.0541
	36	0.3023	-0.0904	0.0653	-0.0460
0.025mm	*24*	0.2266	-0.1244	0.0775	-0.0710
	26	0.2236	-0.1199	0.1112	-0.0677
	28	0.4289	-0.1558	0.1440	-0.0660
	30	0.2445	-0.1092	0.1192	-0.0609
	32	0.2800	-0.0971	0.0904	-0.0553
	34	0.3181	-0.0904	0.0667	-0.0487
	36	0.3320	-0.0876	0.0581	-0.0447
0.03mm	*24*	0.2471	-0.1332	0.1077	-0.0730
	26	0.2429	-0.1117	0.1064	-0.0660
	28	0.2586	-0.1084	0.1188	-0.0632
	30	0.2745	-0.1093	0.1354	-0.0619
	32	0.2963	-0.0976	0.1029	-0.0563
	34	0.3348	-0.0916	0.0786	-0.0502
	36	0.3459	-0.0899	0.0754	-0.0475
0.035mm	*24*	0.2548	-0.1145	0.0825	-0.0687
	26	0.2535	-0.1241	0.1545	-0.0691
	28	0.2609	-0.1138	0.1531	-0.0653
	30	0.2994	-0.0995	0.1132	-0.0599
	32	0.3131	-0.0952	0.1033	-0.0563
	34	0.3419	-0.0923	0.0931	-0.0523
	36	0.3695	-0.0889	0.0731	-0.0472

Table D.3: Rh anode and Rh filter breast transmission fitted function coefficients for a water breast.

Rh Anode	**Energy**	**Coefficients**			
Rh Filter	**(keV)**	**a**	**b**	**c**	**d**
0.02mm	*24*	0.2116	-0.1293	0.0719	-0.0721
	26	0.2099	-0.1205	0.0934	-0.0672
	28	0.2311	-0.1147	0.1008	-0.0631
	30	0.2509	-0.0997	0.0765	-0.0567
	32	0.2593	-0.1025	0.0935	-0.0558
	34	0.3259	-0.1147	0.1124	-0.0541
	36	0.3023	-0.0904	0.0653	-0.0460
0.025mm	*24*	0.2266	-0.1244	0.0775	-0.0710
	26	0.2236	-0.1199	0.1112	-0.0677
	28	0.2453	-0.1063	0.0973	-0.0619
	30	0.2855	-0.1177	0.1292	-0.0617
	32	0.2800	-0.0971	0.0904	-0.0553
	34	0.3181	-0.0904	0.0667	-0.0487
	36	0.3320	-0.0876	0.0581	-0.0447
0.03mm	*24*	0.2471	-0.1332	0.1077	-0.0730
	26	0.2429	-0.1117	0.1064	-0.0660
	28	0.2586	-0.1084	0.1188	-0.0632
	30	0.2745	-0.1093	0.1354	-0.0619
	32	0.2963	-0.0976	0.1029	-0.0563
	34	0.3348	-0.0916	0.0786	-0.0502
	36	0.3459	-0.0899	0.0754	-0.0475
0.035mm	*24*	0.2548	-0.1145	0.0825	-0.0687
	26	0.2535	-0.1241	0.1545	-0.0691
	28	0.2586	-0.1041	0.1285	-0.0636
	30	0.2994	-0.0995	0.1132	-0.0599
	32	0.3131	-0.0952	0.1033	-0.0563
	34	0.3419	-0.0923	0.0931	-0.0523
	36	0.3695	-0.0889	0.0731	-0.0472

Appendix E

Equivalent Breast Thickness and Glandularity

GLANDULARITY: Although Dance et al. (2000) calculated their own coefficients for the data, fitted functions were produced in order to confirm the coefficients. The coefficients differed slightly from published results:

Table E.1: Cubic polynomial fitted coefficients for glandularity as a function of age and breast thickness.

	Coefficients			
Age(years)	**a**	**b**	**c**	**d**
40-49	6.397×10^{-5}	7.251×10^{-4}	-1.894	137.7
50-64	-1.128×10^{-4}	0.0395	-4.555	176.2

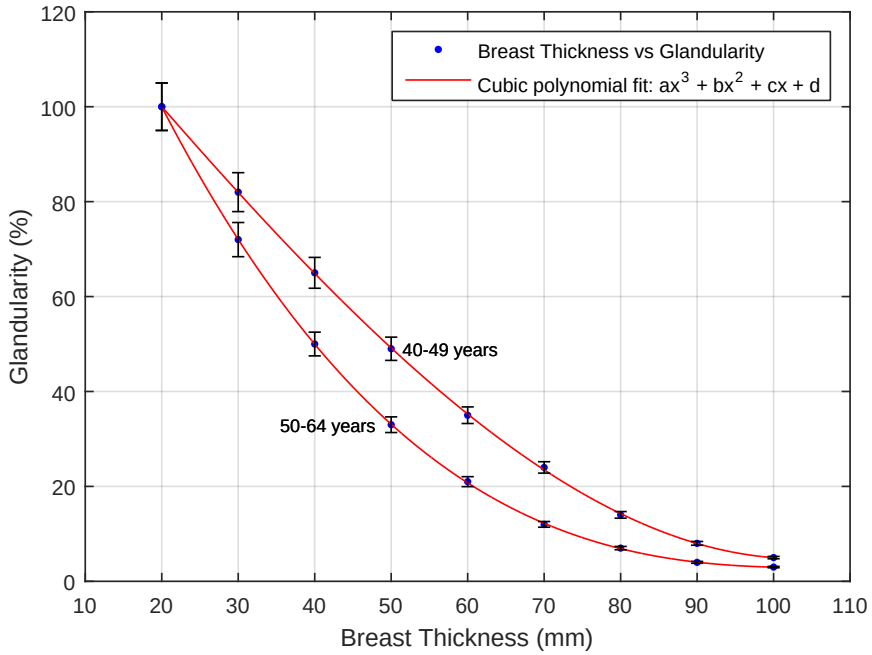

Figure E.1: Age dependant glandularity plots, data from Dance et al. (2000).

Both cubic polynomials had a $R^2 = 1$, the $40 - 49$ years function had an RMSE= 0.29 and an RMSE= 0.17 for the $50 - 64$ years function.

EQUIVALENT BREAST THICKNESS: A cubic polynomial was also fitted to an equivalent breast thickness as a function of PMMA thickness, the coefficients were:

Table E.2: Cubic polynomial fitted coefficients for equivalent breast thickness as a function of PMMA thickness.

Coefficients			
a	**b**	**c**	**d**
-1.547×10^{-4}	0.0254	0.1237	9.565

The fitted cubic had a $R^2 = 1$ with an RMSE= 0.27.

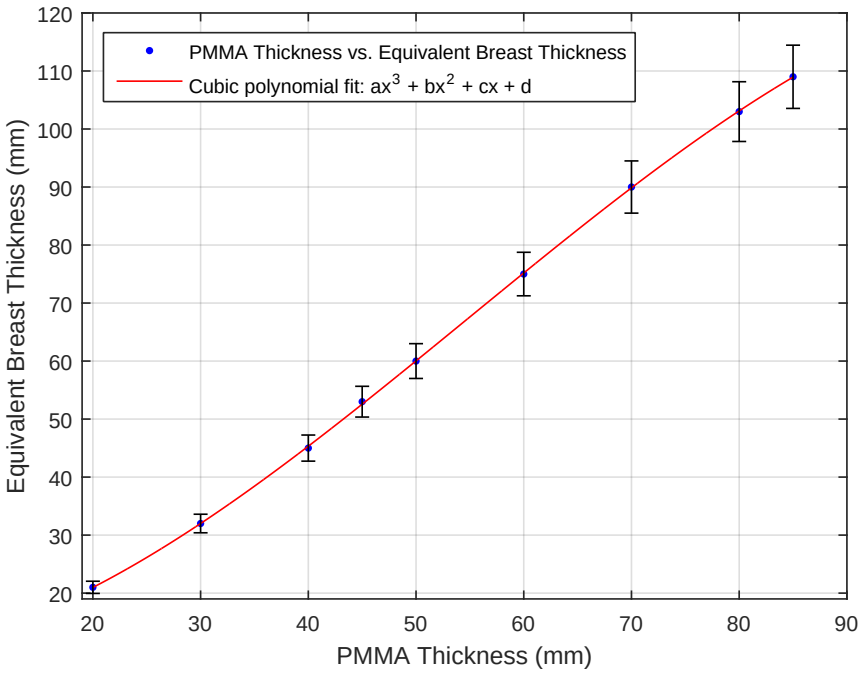

Figure E.2: Equivalent breast thickness as a function of PMMA thickness, data from Dance et al. (2000).

Appendix F

Geant4 Code Snippets

The following code snippets describe the method in which certain aspects of the simulation was performed and recorded.

```
//--------Defining the shape and dimensions of the anode----------------------
G4Tubs* sAnode = new G4Tubs("Anode", 0, 5*cm, 0.75*cm, 0.*deg, 360.*deg);

//---------Defining the logical volume for the anode-------------------------
G4LogicalVolume* lAnode = new G4LogicalVolume(sAnode,fMaterialAnode,"Anode");

//---------Defining the physical volume for the anode------------------------
pAnode = new G4PVPlacement(anodeRot,posA,lAnode,"Anode",logicVacBox,false,0);
```

Figure F.1: Code for simulating the x-ray tube anode.

Here *fMaterialAnode* is the user predefined anode material, *anodeRot* represents the 22.5 degree rotation for the anode angle, and posA is it's position in the geometry relative to it's mother volume *logicVacBox*.

```
//------------Defining electron origin position randomisation---------------------
G4double size = std::cos(angle)*0.3247;
G4double x0 = size * (G4UniformRand())-(size/2);
G4double y0 = -25;
G4double z0 = -y0*std::tan(angle) + (size * (G4UniformRand())-(size/2));

//-----------------Defining electron beam kinematics-----------------------------
G4ParticleDefinition* particle = particleTable->FindParticle(particleName="e-");
fParticleGun  = new G4ParticleGun(1);
fParticleGun->SetParticleDefinition(particle);
fParticleGun->SetParticleMomentumDirection(G4ThreeVector(0.,1.,-std::tan(angle)));
fParticleGun->SetParticleEnergy(GunElectronEnergy*keV);
fParticleGun->SetParticlePosition(G4ThreeVector(x0, y0, z0));
```

Figure F.2: Code for simulating the electron beam.

The varable *angle* was globally assigned as 22.5 degrees.

```
//--Coefficients from rational fit to NIST mass attenuation data--
G4double p1 = -0.0001494528;
G4double p2 = 0.03955245;
G4double p3 = -1.078084;
G4double p4 = -20.02434;
G4double p5 = 4488.449;
G4double q1 = -1.557;
G4double q2 = 8.358;
G4double q3 = -13.73;

//--1 x 1cm Detector surface area--
G4double IncidentDetSurfaceArea = 1;

//--Detector surface area of breast--
G4double surfaceAreaOther = 100.531;

//--Momentum vector and Z direction momentum--
G4ThreeVector momentum = fTrack->GetMomentum();
G4double pz = momentum.z();

//--Getting the volume name the track is passing through--
G4LogicalVolume* volume = aStep->GetPreStepPoint()->GetTouchableHandle()
                         ->GetVolume()->GetLogicalVolume();
G4String volName = volume->GetName();

//--Getting volume names of pre and post stepping points--
G4String PreStepVolumeName = aStep->GetPreStepPoint()->GetPhysicalVolume()
                             ->GetName();
G4String PostStepVolumeName = aStep->GetPostStepPoint()->GetPhysicalVolume()
                              ->GetName();

//--Statement for track requirements: must be "gamma"
//                                    must have +ve momentum in Z direction
//                                    must have gone through the detector volume
if (PreStepVolumeName != PostStepVolumeName
        && fTrack->GetParticleDefinition()->GetParticleName() == "gamma"
        && pz > 0)
{
//-------------------------Incident Kerma Detector-----------------------------
        if (volName == "IncidentDet")
{
//      Getting energy of track in keV
        G4double EMGD = fTrack->GetKineticEnergy() / keV;

//      Calculating mass energy-absorption coefficient from track energy
        G4double massAbsCoeffIncident = ((p1 * (std::pow(EMGD, 4))) + (p2 *
            (std::pow(EMGD, 3))) + (p3 * (std::pow(EMGD, 2))) + (p4 * EMGD) + p5)/
            ((std::pow(EMGD, 3)) + (q1 * (std::pow(EMGD, 2))) + (q2 * EMGD) + q3);

//      Calculating kerma of track
        G4double edepStepMGD = (1/IncidentDetSurfaceArea) * massAbsCoeffIncident
                               * 1000 * EMGD * 1.602176565 * (std::pow(10, -16));

//      Sending kerma calculation to EventAction.cc
        fEventAction->AddEdep(edepStepMGD);
}
}
```

Figure F.3: Kerma code from *SteppingAction.cc* used to calculate kerma in the relevant detector volumes.

```
// Defining phase space file and location
G4String intialFolder = "PHSP_files/";
G4String str = intialFolder + fileName;// fileName = input file name
const char * fileLoc = str.c_str();

//-------------Obtaining Energy Spectrum from PHSP File---------------//
// Access properties
IAEA_I32 source_read = 0;
IAEA_I32 access_read = 1, access_write = 2, access_append = 3;
IAEA_I32 result;

// Particle properties
IAEA_I32 type, extra_ints[1];
IAEA_Float E, wt, x, y, z, u, v, w, extra_floats[1];

// Source file input
char* fiaearead = const_cast<char*>(fileLoc);
IAEA_I32 len = 81;
iaea_new_source(&source_read, fiaearead, &access_read, &result, len);

IAEA_I64 histories; // Getting total number of histories
IAEA_I64 OriginalParticles; // Getting total number of original particles

result = -1; // To request for the total number of particles
iaea_get_max_particles(&source_read, &result, &histories);
iaea_get_total_original_particles(&source_read, &OriginalParticles);

IAEA_I32 n_stat;
IAEA_I64 read_indep = 0, nread = 0, nrecorded = 0;
IAEA_I64 irecord;

for (irecord = 0; irecord < histories; irecord++)
{
        // read IAEA particle from file
        iaea_get_particle(&source_read, &n_stat,
                &type, // particle type
                &E,    // kinetic energy in MeV
                &wt,   // statistical weight
                &x,    // x position in cartesian coordinates
                &y,    // y position in cartesian coordinates
                &z,    // z position in cartesian coordinates
                &u,    // x direction in cartesian coordinates
                &v,    // y direction in cartesian coordinates
                &w,    // z direction in cartesian coordinates
                extra_floats, extra_ints);
        nread++;
        if (n_stat == -1) break;

//Output energy in keV
G4double energy = E / keV;

//Defining file name as phase-space filename and writing to it
G4String dataFileName = fileName + "_SPECTRUM_DATA.txt";
ofstream myfile(dataFileName, ios::out | ios::app);
myfile << energy << "\n";
myfile.close();
}
```

Figure F.4: Method to read phase-space file data; part of *PrimaryGeneratorAction.cc* used to obtain filtered spectra and calculate mean energies.

```
//-------------------------Material Definitions-----------------------------
G4Material* Air = nist->FindOrBuildMaterial("G4_AIR");
G4Material* perspex = nist->FindOrBuildMaterial("G4_PLEXIGLASS");
G4Material* CsI = nist->FindOrBuildMaterial("G4_CESIUM_IODIDE");
G4Material* elTl = nist->FindOrBuildMaterial("G4_Tl");
G4Material* water = nist->FindOrBuildMaterial("G4_WATER");

G4Material* CsI_Tl = new G4Material("CsI_Tl", densityCsI_Tl= 4.51*g/cm3,
                                    ncomponents=2);
CsI_Tl->AddMaterial(CsI,99.6*perCent);
CsI_Tl->AddMaterial(elTl,0.4*perCent);

G4double densityCF = 1.45*g/cm3;
G4Material* CarbonFiber = new G4Material(name="CarbonFiber", densityCF,
                                         nel=1);
CarbonFiber->AddElement(elC,1);

//-----------Relevant breast transmission volumes and detectors-------------
Det2AboveBreastAndPaddle = BoxShape(breastSupportDist - breast_thickness -
                                    (0.144*2)*cm - 0.255*cm, 0.*cm, 0*cm,
                                     0.001*mm, 0*cm, 8*cm, Air,
                                     "Det2AboveBreastAndPaddle");

Compression_paddle = BoxShape(breastSupportDist - breast_thickness -
                              (0.144*2)*cm - 0.53*cm, 0*cm, 12*cm, 0.075*cm,
                               15.35*cm, 12*cm,
                               perspex, "CompPaddle");

Breast = BoxShape(breast_zpos, 0.*cm, 0*cm, (breast_thickness/2), 0*cm, 8*cm,
                  water, "Breast");

MGDdet = BoxShape(breastSupportDist - breast_thickness - (0.144*2)*cm -
                  0.445*cm, 0*cm, 5*cm, 0.001*mm, 2*cm, 2*cm, Air, "MGDdet");

Breast_support = BoxShape(breastSupportDist, 0*cm, 12*cm, 0.6*mm, 15.35*cm,
                          12*cm, CarbonFiber, "BreastSup");

Det3BeforeGrid = BoxShape(65.75*cm, 0.*cm, 0*cm, 0.001*mm, 0*cm, 8*cm, Air,
                          "Det3BeforeGrid");

Det4AtDetector = BoxShape(65.95*cm, 0.*cm, 0*cm, 0.001*mm, 0*cm, 8*cm, Air,
                          "Det4AtDetector");

CsI_detector = BoxShape(66.025*cm, 0*cm, 12*cm, 0.5*mm, 15.35*cm, 12*cm,
                        CsI_Tl, "CsI_det");

//----------------------Detector volume indexing----------------------------
fDetScoringVolume[0] = Det2AboveBreastAndPaddle->GetLogicalVolume();
fDetScoringVolume[1] = Det3BeforeGrid->GetLogicalVolume();
fDetScoringVolume[2] = Det4AtDetector->GetLogicalVolume();
fDetScoringVolume[3] = Breast->GetLogicalVolume();
fDetScoringVolume[4] = CsI_detector->GetLogicalVolume();
fDetScoringVolume[5] = MGDdet->GetLogicalVolume();

return physWorld;
}
```

Figure F.5: Method used to define the physical volumes and detectors used during breast transmission, and how the detectors were indexed.

```
//----------------------Detector volume indexing---------------------------
fDetScoringVolume[0] = Det2AboveBreastAndPaddle->GetLogicalVolume();
fDetScoringVolume[1] = Det3BeforeGrid->GetLogicalVolume();
fDetScoringVolume[2] = Det4AtDetector->GetLogicalVolume();
fDetScoringVolume[3] = Breast->GetLogicalVolume();
fDetScoringVolume[4] = CsI_detector->GetLogicalVolume();
fDetScoringVolume[5] = MGDdet->GetLogicalVolume();

return physWorld;
}

//------Construct applied to breast transmission voluumes and detectors-----
G4VPhysicalVolume* B1DetectorConstruction::BoxShape(G4double FilterZPosition,
                          G4double FilterXPosition, G4double FilterYPosition,
                          G4double FilterThickness, G4double DetX,
                          G4double DetY, G4Material* FilterMaterial,
                          G4String VolName)
{
G4ThreeVector posFilter = G4ThreeVector(FilterXPosition, FilterYPosition,
                                        FilterZPosition);

G4RotationMatrix* fieldRot = new G4RotationMatrix();
fieldRot->rotateX(90.*deg);

G4Box* solidShapeFilterPad;
G4Tubs* solidShapeFilter;

//--------------Box shape appllied to relevent volumes----------------------
if (VolName == "CompPaddle" || VolName == "BreastSup"
                || VolName == "CsI_det" || VolName == "MGDdet")
{
solidShapeFilterPad = new G4Box("Filter2Box", DetX, DetY, FilterThickness);

G4LogicalVolume* logicVolFilter = new G4LogicalVolume(solidShapeFilterPad,
                                                      FilterMaterial,
                                                      VolName);

return new G4PVPlacement(0, posFilter, logicVolFilter, VolName, MotherVolumn,
                         false, 0, checkOverlaps);
}

//------Half cylinder shape applied to breast and some detector volumes-----
else
{
solidShapeFilter = new G4Tubs("Filter2Box", DetX, DetY, FilterThickness,
                              0.*deg, 180.*deg);

G4LogicalVolume* logicVolFilter = new G4LogicalVolume(solidShapeFilter,
                                  FilterMaterial, VolName);

return new G4PVPlacement(0, posFilter, logicVolFilter, VolName, MotherVolumn,
                         false, 0, checkOverlaps);
}
}
```

Figure F.6: Following on from Figure F.5, this shows the method to construct the physical volumes and detectors during breast transmission.

Appendix G

Validation Measurement Images

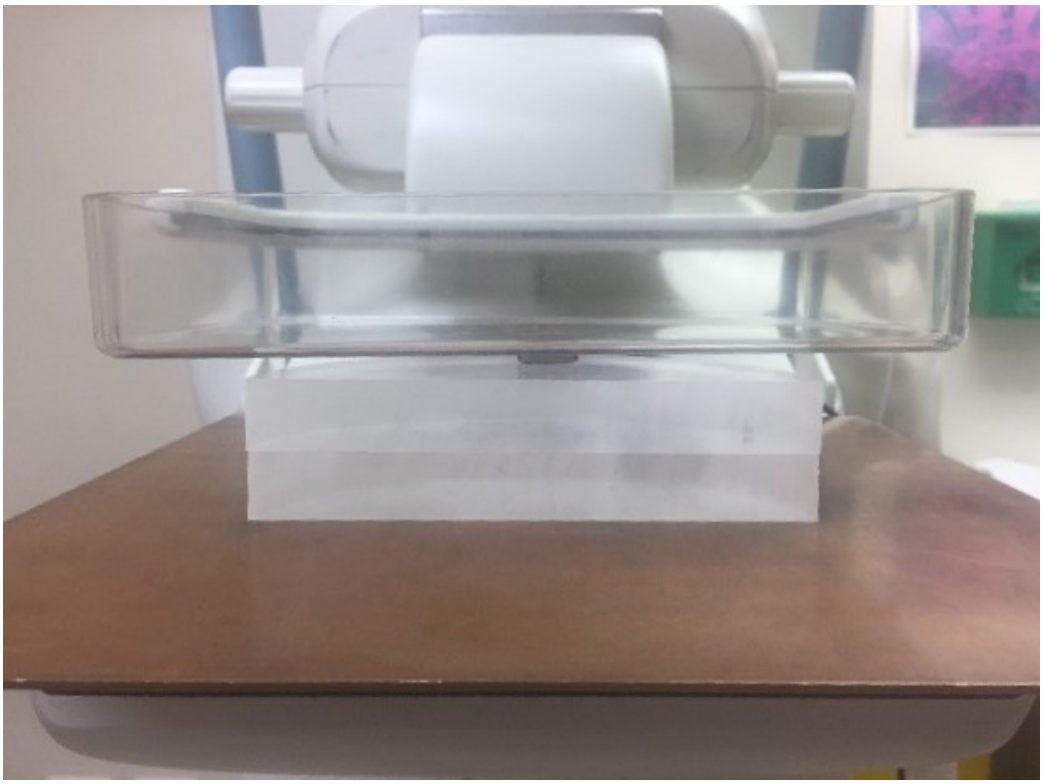

Figure G.1: Image of the entrance kerma measurement with the dosimeter between the compression paddle and two blocks of 19mm PMMA slabs.

Figure G.2: Image of the entire mammography unit during validation measurements.

References

Agostinelli, S., Allison, J., Amako, K. a., Apostolakis, J., Araujo, H., Arce, P., ... others (2003). GEANT4—a simulation toolkit. *Nuclear instruments and methods in physics research section A: Accelerators, Spectrometers, Detectors and Associated Equipment*, *506*(3), 250–303.

Archer, B. R., Thornby, J., & Bushong, S. C. (1983). Diagnostic X-ray shielding design based on an empirical model of photon attenuation. *Health physics*, *44*(5), 507–517.

Badger, L. (1994). Lazzarini's lucky approximation of π. *Mathematics Magazine*, *67*(2), 83–91.

Bearden, J. A. (1967). X-ray wavelengths. *Reviews of Modern Physics*, *39*(1), 78.

Berger, M., Hubbell, J., Seltzer, S., Chang, J., Coursey, J., Sukumar, R., ... Olsen, K. (2011). *XCOM: Photon cross section database (version 1.5), National Institute of Standards and Technology, Gaithersburg, MD, 2010.*

Boone, J. M., Fewell, T. R., & Jennings, R. J. (1997). Molybdenum, rhodium, and tungsten anode spectral models using interpolating polynomials with application to mammography. *Medical physics*, *24*(12), 1863–1874.

Boyd, N., O'sullivan, B., Campbell, J., Fishell, E., Simor, I., Cooke, G., & Germanson, T. (1982). Mammographic signs as risk factors for breast cancer. *British journal of cancer*, *45*(2), 185.

Boyd, N. F., Martin, L. J., Bronskill, M., Yaffe, M. J., Duric, N., & Minkin, S. (2010). Breast tissue composition and susceptibility to breast cancer. *Journal of the National Cancer Institute*.

Bushberg, J. T., & Boone, J. M. (2011). *The essential physics of medical imaging.* Lippincott Williams & Wilkins.

Cortés-Giraldo, M. A., Quesada, J. M., Gallardo, M. I., & Capote, R. (2009). *Geant4 interface to work with iaea phase-space files.*

Cortés-Giraldo, M. A., Quesada, J. M., Gallardo, M. I., & Capote, R. (2012). An implementation to read and write IAEA phase-space files in geant4-based simulations. *International journal of radiation biology*, *88*(1-2), 200–208.

Cranley, K., Fogarty, G., & Desponds, L. (1997). IPEM Report 78. *Catalogue of diagnostic x-ray spectra and other data (CD-Rom Edition 1997)(Electronic Version prepared by D Sutton)(York: The Institute of Physics and Engineering in Medicine (IPEM)).*

Dance, D. (1990). Monte-Carlo calculation of conversion factors for the estimation of mean glandular breast dose. *Physics in medicine and biology*, *35*(9), 1211.

Dance, D., Christofides, S., & Maidment, A. D. (2014). Diagnostic radiology physics: A handbook for teachers and students.

Dance, D., Skinner, C., Young, K., Beckett, J., & Kotre, C. (2000). Additional factors for the estimation of mean glandular breast dose using the UK mammography dosimetry protocol. *Physics in medicine and biology*, *45*(11), 3225.

Dance, D., Young, K., & Van Engen, R. (2009). Further factors for the estimation of mean glandular dose using the United Kingdom, European and IAEA breast dosimetry protocols. *Physics in medicine and biology*, *54*(14), 4361.

Dance, D., Young, K., & Van Engen, R. (2010). Estimation of mean glandular dose for breast tomosynthesis: factors for use with the uk, european and iaea breast dosimetry protocols. *Physics in medicine and biology*, *56*(2), 453.

De Benedetto, D., Abdulcadir, D., Giannotti, E., Nori, J., Vanzi, E., & Capaccioli, L. (2016). Radiological anatomy of the breast. *Italian Journal of Anatomy and Embryology*, *121*(1), 20–36.

Dewey, R., Mapes, R., & Reynolds, T. (1969). *Progress in nuclear energy, series IX.* Pergamon Press, New York.

Electronics, R. (2013). *Specifications, black piranha.* Retrieved from `http://rtigroup.com/content/downloads/brochures/Specifications_Piranha.pdf`

Ellis, H., & Mahadevan, V. (2013). Anatomy and physiology of the breast. *Surgery (Oxford)*, *31*(1), 11–14.

Geeraert, N., Klausza, R., Mullera, S., et al. (2012). Breast characteristics and dosimetric data in X-ray mammography - A large sample worldwide survey. In *Bonn: Iaea conference.*

General Electric. (2013). *Senograph Essential.* GE™Healthcare. (Technical data)

Gram, I. T., Funkhouser, E., & Tabár, L. (1997). The tabar classification of mammographic parenchymal patterns. *European journal of radiology*, *24*(2), 131–136.

Heggie, J., McLean, I., Herley, J., Thomson, F., Grewal, R., Diffey, J., & Collins, L. (2012). ACPSEM position paper: recommendations for a digital mammography quality assurance program V3. 0. *Australas Phys Eng Sci Med*, *24*, 1–27.

Hogg, P., Kelly, J., & Mercer, C. (2015). *Digital mammography: a holistic approach.* Springer.

Hubbell, J. H., & Seltzer, S. M. (1995). *Tables of x-ray mass attenuation coefficients and mass energy-absorption coefficients 1 keV to 20 MeV for elements Z= 1 to 92 and 48 additional substances of dosimetric interest* (Tech. Rep.). National Inst. of Standards and Technology-PL, Gaithersburg, MD (United States). Ionizing Radiation Div.

Johns, H. E., & Cunningham, J. R. (1983). *The physics of radiology* (4th ed.). Springfield, IL: Charles C Thomas.

Johns, P. C., & Yaffe, M. J. (1987). X-ray characterisation of normal and neoplastic breast tissues. *Physics in medicine and biology*, *32*(6), 675.

Khan, F. M., & Gibbons, J. P. (2014). *Khan's the physics of radiation therapy* (5th ed.). Philadelphia, PA: Lippincott Williams & Wilkins.

Li, X., Zhang, D., & Liu, B. (2012). Transmission of broad W/Rh and W/Al (target/filter)

x-ray beams operated at 25–49 kVp through common shielding materials. *Medical physics*, *39*(7), 4132–4138.

Metropolis, N., & Ulam, S. (1949). The monte carlo method. *Journal of the American statistical association*, *44*(247), 335–341.

Ministry of Health. (2016a). *New cancer registrations 2014.* `http://www.health.govt.nz/publication/new-cancer-registrations-2014`.

Ministry of Health. (2016b). *Selected cancers 2013, 2014, 2015.* `http://www.health.govt.nz/publication/selected-cancers-2013-2014-2015`.

Poludniowski, G., Landry, G., DeBlois, F., Evans, P., & Verhaegen, F. (2009). SpekCalc: a program to calculate photon spectra from tungsten anode x-ray tubes. *Physics in medicine and biology*, *54*(19), N433.

Poludniowski, G. G. (2007). Calculation of x-ray spectra emerging from an x-ray tube. Part II. X-ray production and filtration in x-ray targets. *Medical physics*, *34*(6), 2175–2186.

Poludniowski, G. G., & Evans, P. M. (2007). Calculation of x-ray spectra emerging from an x-ray tube. Part I. Electron penetration characteristics in x-ray targets. *Medical physics*, *34*(6), 2164–2174.

Salem, S., Panossian, S., & Krause, R. A. (1974). Experimental K and L relative x-ray emission rates. *Atomic Data and Nuclear Data Tables*, *14*(2), 91–109.

Senographe Essential Service Information and Procedures Class A SIP-A (1st ed.) [Computer software manual]. (2014). (Technical Publications)

Sickles, E., D'Orsi, C., Bassett, L., Appleton, C., Berg, W., Burnside, E., et al. (2013). ACR BI-RADS® mammography. *ACR BI-RADS Atlas, Breast Imaging Reporting and Data System*, 123–132.

Sobol, W. T., & Wu, X. (1997). Parametrization of mammography normalized average glandular dose tables. *Medical physics*, *24*(4), 547–554.

Soeberg, M. J. (2014). *Trends in cancer survival by ethnic and socioeconomic group, New Zealand, 1991-2004* (Unpublished doctoral dissertation). University of Otago.

Tortora, G. J., & Derrickson, B. H. (2012). *Principles of anatomy and physiology.* John Wiley & Sons.

Turner, J. E. (2008). *Atoms, radiation, and radiation protection* (3rd ed.). Weinheim, Germany: John Wiley & Sons.

Wu, X., Barnes, G. T., & Tucker, D. (1991). Spectral dependence of glandular tissue dose in screen-film mammography. *Radiology*, *179*(1), 143–148.

Wu, X., Gingold, E. L., Barnes, G. T., & Tucker, D. M. (1994). Normalized average glandular dose in molybdenum target-rhodium filter and rhodium target-rhodium filter mammography. *Radiology*, *193*(1), 83–89.

Zhao, W., Ristic, G., & Rowlands, J. (2004). X-ray imaging performance of structured cesium iodide scintillators. *Medical physics*, *31*(9), 2594–2605.